Zwitterionic Polymers and Their Derivatives as Drug and Gene Delivery Carriers and Implantable Materials

Lei Zhang

A dissertation

submitted in partial fulfillment of the

requirements for the degree of

Doctor of Philosophy

University of Washington

2012

Reading Committee:

Shaoyi Jiang, Chair

Buddy D. Ratner

Suzie H. Pun

Program Authorized to Offer Degree:

Chemical Engineering

University of Washington

Abstract

Zwitterionic Polymers and Their Derivatives as Drug and Gene Delivery Carriers and Implantable Materials

Lei Zhang

Chair of the Supervisory Committee:

Professor Shaoyi Jiang

This dissertation mainly focuses on the development of zwitterionic-based materials and their biomedical applications, particularly, multifunctional zwitterionic-based nanoparticles (NPs) for targeted imaging and drug delivery, microparticles for DNA vaccine delivery, and *in vivo* evaluation of zwitterionic-based nanoparticles and hydrogel implants.

In the multifunctional nanoparticle work, stealthy and functionalizable magnetic nanoparticles were first developed by coating them with polycarboxybetaine (PCBMA) using a biomimetic adhesive linkage. After conjugation with a targeting ligand, the

PCBMA coated NPs could efficiently enter cells and be imaged with magnetic resonance imaging (MRI). Second, degradable PCBMA nanogels were developed using a reduction-sensitive crosslinker. The nanogels could encapsulate both imaging reagents and macromolecule drugs. They were degradable and able to release their payload spontaneously after entering the intracellular reducing environment. The degraded products could be excreted from the body via renal clearance, making the nanogels a safe and ideal platform for targeted imaging and drug delivery.

In the DNA vaccine delivery work, microparticles were developed using a CBMA ethyl ester (CBMA-EE) monomer and its tertiary amine analogue. Gene transfection results showed that microparticles with a 1:1 molar ratio of the two monomers had the best transfection efficiency, which was twelve times higher than commercially developed PLGA-CTAB microparticles. Together with their low toxicity and passive targeting effect to macrophage cells, the microparticles developed in this work could potentially be used as a suitable platform for DNA vaccine delivery.

In the *in vivo* evaluation work, *in vivo* circulation time of PCBMA nanogels and the foreign body reaction to PCBMA hydrogel implants were studied. Results of PCBMA nanogels showed that they exhibit an extended circulation time in a rat model. Furthermore, it was found that softer nanogels were able to more effectively pass through splenic filtration and had a longer circulation time. *In vivo* implantation studies show that that PCBMA holds great promise as an ideal coating for implantable medical devices.

TABLE OF CONTENTS

LIST OF FIGURES

Figure number Page

LIST OF TABLES

Table number Page

ACKNOWLEDGEMENTS

For all the work presented here, the author would like to thank his advisor, Prof. Shaoyi Jiang, for support, monetary and inspiration. The author would also thank Prof. Buddy D. Ratner, Prof. Allan S. Hoffman, Prof. Suzie H. Pun, Prof. Qiuming Yu and Prof. Dayong Gao for their collaborations and valuable suggestions. The author would also thank all members in Prof. Jiang's research group for their kind help and discussion. The author would especially thank his family.

The PCB nanoparticles and hydrogel implantation work were supported by the Office of Naval Research (N000140910137), the National Science Foundation (DMR-0705907 and DMR-1005699). The SERS detection work was supported in part by the University of Washington (UW) faculty start-up funds and NOAA Oceans and Human Health Initiative funds (to Prof. Qiuming Yu), and by the Defense Threat Reduction Agency (HDTRA1-10-1-0074). Nanofabrication and SERS measurements were performed at the Nanotech User Facility, the UW site of the National Nanotechnology Infrastructure Network (NNIN) supported by the NSF. The DNA vaccine delivery work was supported by the National Science Foundation (DMR-1005699).

Chapter 1 Introduction

The fast development of biomaterials holds great potential to improve the treatment of human diseases in terms of the design of novel drug delivery systems, medical devices, etc [1-3]. However, one major challenge, nonspecific bio-fouling, still remains unsolved and has been greatly impeding the performance of biomaterials in many biomedical applications [4]. Bio-fouling is defined as the undesirable attachment of biomolecules, cells, etc. onto the surface of biomaterials, causing failure of the delivery systems or the devices [5]. For example, nano-carriers are designed to deliver therapeutic drugs and/or imaging agents to the target site. They are commonly injected into the body intravenously; however, as soon as they come in contact with blood, fouling of blood proteins onto their surface can result in recognition by the innate immune system. Consequently the nano-carriers are cleared from blood circulation [6, 7].

To solve the above problem, biomaterials with anti-fouling properties are highly desirable. Currently, polyethylene glycol (PEG) is the most widely used anti-fouling material and plays important roles in many application areas. However, certain drawbacks limit the application of PEG; for example, PEG is susceptible to oxidation damage and could lose its function in biological media, which is undesirable for long term applications [8]. Zwitterionic materials have been emerging as a new class of anti-fouling material and attracting significant attention in this field. While non-ionic

hydrophilic anti-fouling materials such as PEG achieve hydration via hydrogen bonding, zwitterionic materials, such as phosphobetaine, sulfobetaine, and carboxybetaine, provide even stronger hydration via ionic salvation [4].

Among zwitterionic materials, carboxybetaine (CB) is of particular interest due to its unique properties. Our group has demonstrated PCB surfaces can achieve undetectable nonspecific protein adsorption (<0.3 ng/cm^2) from single-protein solutions or complex media by SPR [9]. One unique property is that the carboxyl groups in PCB could be conjugated to amine-containing functional molecules via simple 1-ethyl-3-(3-dimethylaminopropyl)-carbodiimide and N-hydroxysuccinimide (EDC/ NHS) chemistry for a specific application, while the un-reacted PCB maintains a non-fouling background. Another unique property is that the carboxyl group in PCB can be hidden by a hydrolysable ester group, rendering the polymer positively charged [10]. Before hydrolysis, this cationic polymer can be used to condense negatively charged DNA or to kill bacteria, while after hydrolysis, it is converted to zwitterionic polymer and spontaneously releases DNA or bacteria [11, 12]. These features make PCB esters very promising as biocompatible antimicrobial coatings and highly effective gene delivery carriers [4].

This thesis mainly focuses on three important aspects of zwitterionic PCB materials for biomedical applications:

1.1 Multifunctional nanoparticles

Multifunctional nanoparticles that combine several functions in one platform have

been attracting increasing attention recently for uses in targeted drug delivery and imaging, biosensing [13, 14], etc.

My first project was to coat magnetic nanoparticles (MNPs) with PCBMA polymer using a biomimetic adhesive linkage. It was found that the PCBMA coating could efficiently stabilize MNPs in saline and 100% serum solutions. Meanwhile, PCBMA-MNPs could also evade non-specific uptake by macrophage cells, indicating that they were potentially stealthy to the innate immune system. Moreover, the PCBMA coating was conjugated with a targeting peptide, which greatly facilitated uptake of the particles by human umbilical vein endothelial cells (HUVEC), as visualized by MRI. This work has been published in **Biomaterials** in 2010 and will be discussed in Chapter 2.

My second project focused on PCBMA nanogels and their use to encapsulate both magnetic NPs and a model drug. Considering the needs for drug release, as well as the removal of the nanogels from the body after they finish their task, a reduction-sensitive crosslinker was used in the nanogel formulation, which can be cleaved in a reducing environment. This work has been published in **Biomaterials** in 2011 and will be discussed in Chapter 3.

My third project demonstrated the use of plasmonic-magnetic NPs for fast condensation and detection of bacteria using surface enhanced Raman spectrometry (SERS). This work has been published in **Biosensors and Bioelectronics** in 2012 and will be discussed in Chapter 4.

1.2 Hydrolytic cationic ester microparticles for DNA vaccine delivery

Previous work in our group has shown excellent gene transfection efficiency using PCBMA-EE and its tertiary analogue [11]. PCBMA-EE, containing quaternary amines, is positively charged and could be used to condense negatively charged DNA, while a tertiary analogue of CBMA-EE, containing tertiary amines, could be used for endosomal escape purposes. In my sixth project, we aimed to use PCBMA-EE based microparticles for DNA vaccine delivery. Microparticles have been prepared using CBMA-EE and its tertiary analogue with different molar ratios. PLGA-CTAB microparticles were prepared using the method developed by Chiron Corporation [15]. Gene transfection results show that microparticles with a 1:1 quaternary to tertiary ratio achieved the best gene transfection efficiency to macrophage cells, which was twelve times higher than the PLGA-CTAB control. Furthermore, no obvious toxicity could be observed from the microparticles. The goal is to develop a nontoxic and more efficient delivery platform for DNA vaccine delivery. This work has been submitted for publication and will be discussed in more detail in Chapter 5.

1.3 *In vivo* evaluation of poly carboxybetaine nanoparticles and hydrogels

Due to the excellent anti-fouling properties of zwitterionic materials *in vitro*, they are expected to have good *in vivo* performance. The fifth project is focuses on the *in vivo* circulation time and biodistribution of PCBMA NPs. A CBMA crosslinker (CBMAX) was developed and used to formulate PCBMA nanogels. Gold NPs were encapsulated in the nanogels as a marker in the blood. Results show the long circulation time of the

nanogels. Moreover, the crosslinking density and solid content were tuned to change the stiffness of the nanogels. Biodistribution studies showed that the softer nanogels could better pass through splenic filtration, and consequently had less accumulation in the spleen and longer circulation half-life. It has been well recognized that poor *in vivo* circulation time of NPs is due to non-specific adsorption of blood proteins and their subsequent removal by reticuloendothelial system (RES). The excellent anti-fouling property of PCB accounts for their stealth *in vivo*. This work has been submitted to **ACS Nano** and will be discussed in more detail in Chapter 6.

The sixth project focused on the *in vivo* evaluation of subcutaneously implanted PCBMA hydrogels. Medical devices are subjected to the foreign body reaction after implantation into the body, and almost all implantable devices will end up being coated with a dense avascular collagen capsule, which could isolate the devices from the body and cause them to lose their function [16]. Results show that compared to HEMA hydrogels, PCBMA hydrogels received a substantially mitigated foreign body reaction. After three months of implantation, PHEMA hydrogels were coated with a dense collagen capsule, which is consistent with literature reports. In contrast, PCBMA hydrogels were surrounded with diffused collagen. Moreover, the blood vessel density adjacent to PCBMA samples was much higher than PHEMA samples. The above results show that PCBMA hydrogels are very promising as coatings for implantable devices with improved biocompatibility and device efficiency. This work has been submitted for publication and will be discussed in more detail in Chapter 7.

Chapter 2 Multifunctional Zwitterionic Magnetic Nanoparticles with a Biomimetic Adhesive Linkage

Multifunctional magnetic nanoparticles (MNPs) modified by a zwitterionic polymer (PCBMA–$DOPA_2$) containing one poly(carboxybetaine methacrylate) (PCBMA) chain and two 3,4-dihydroxyphenyl-l-alanine (DOPA) residue groups were developed. Results showed that MNPs modified by PCBMA were not only stable in complex media, but also provided abundant functional groups for ligand immobilization. The PCBMA–$DOPA_2$ MNPs had a hydrodynamic particle size of about 130 nm, a strong saturation magnetization of 110.2 emu/g Fe and a high transverse relaxivity of 428 mm^{-1} s^{-1}. Long-term stability in phosphate-buffered saline (PBS) and 10% NaCl solution was achieved for over six months. Compared to MNPs coated with dextran, PCBMA–$DOPA_2$ MNPs presented better stability in 100% human blood serum at 37 °C. Macrophage cell uptake studies revealed that the uptake ratio of PCBMA–$DOPA_2$ MNPs was much lower than that of dextran MNPs. Furthermore, quantitative analysis results showed that after PCBMA–$DOPA_2$ MNPs were conjugated with a targeting RGD peptide, uptake by human umbilical vein endothelial cell was notably increased, which was further visualized by magnetic resonance imaging.

2.1 Introduction

Magnetic nanoparticles (MNPs) have many attractive properties, often combining low toxicity with excellent magnetic properties [17-20]. Recently, “theranostics”, which incorporate both therapy and diagnosis, are attracting significant attention and may revolutionize current medical treatments [3, 21]. To achieve this goal, MNPs can work as multifunctional carriers to selectively accumulate at the target site, cure disease by certain mechanisms (either hyperthermia or drug release) and be detected using non-invasive diagnosis modality such as MRI [21]. Multifunctional MNPs can typically be formed from magnetic cores and surface coating [3]. Magnetic cores are iron oxide nanoparticles which are detectable by MRI and can be manipulated by a magnetic field, while an ideal surface coating can carry a therapeutic reagent, prevent MNPs from being cleared from the blood circulation, and provide functional groups for conjugation of targeting ligands. Thus, the surface coating plays a key role in achieving multifunctional MNPs.

Many classes of polymers have been investigated to decorate MNPs. However, few candidates can really fulfill the *in vivo* requirements. For *in vivo* applications, magnetic nanoparticles are subject to opsonization immediately upon introduction to the bloodstream, serum proteins will adsorb onto MNPs surfaces. As a result, MNPs will quickly be recognized by the reticuloendothelial system (RES) and cleared from the blood, resulting in very limited longevity and poor targeting efficiency [17, 19]. To address this issue, neutral and hydrophilic polymers are preferred since they can reduce opsonization and improve *in vivo* circulation half-life. Dextran and poly(ethylene glycol)

(PEG) are the most widely studied polymers for this purpose. Moreover, they can also carry functional groups such as amines or carboxyl groups after suitable modifications for conjugation of targeting moieties. However, both dextran and PEG present certain drawbacks that influence their *in vivo* performance. To conjugate targeting moieties, the amines of dextran MNPs are often cross-linked by epichlorohydrin and ammonia. The resulting amine-terminated cross-linked iron oxide nanoparticles (CLIO) are then conjugated to functional molecules. This method creates one major problem, as the cross-linking agent, epiclorohydrin, is classified as a carcinogenic, mutagenic, and reprotoxic substance [13]. PEG is subjected to oxidization in the presence of oxygen and transition metal ions [22]. Furthermore, when PEG is coated onto NPs, one PEG chain offers only one functional group. Recently, a new class of zwitterionic materials have been developed and showed excellent low fouling properties against complex media such as undiluted blood serum or plasma [23]. It has been shown that zwitterionic poly(carboxybetaine methacrylate) (PCBMA) is not only highly resistant to nonspecific protein adsorption, but also provides abundant carboxyl groups for ligand immobilization [10, 24].

To coat the zwitterionic polymer onto a surface, the “graft-from-surface” method via atom transfer radical polymerization (ATRP) has achieved surface coatings with excellent ultra low fouling properties [22]. However, ATRP reactions require surface-grafted initiators, catalysts, and oxygen-free conditions which limit its practical application. To address this problem, another strategy, the “graft-to-surface” method has been employed

in this work. In this method, polymers carrying adhesive moieties with strong surface affinity are synthesized and then grafted onto the surface through their adhesive moieties. Recently, 3,4-dihydroxyphenyl-L-alanine (DOPA) inspired from the adhesive proteins found in mussels has been shown to have high affinity towards many types of surfaces [25, 26].

Here, we present a convenient method to coat MNPs with the dual-functional PCBMA polymer via two DOPA groups. Results show that PCBMA-MNPs presented high saturation magnetization and long-term stability in bio-relevant media such as 100% human blood serum. Moreover, PCBMA-MNPs can be easily conjugated to a RGD peptide for their enhanced ability to enter targeted cells.

2.2. Experimental

2.2.1 Materials

$FeCl_2 \cdot 4H_2O$ (>99%), $FeCl_3 \cdot 6H_2O$ (>99%), $NH_3 \cdot H_2O$ (NH_3 content: 28~30%), dextran (M.W. 10,000) from Leuconostoc mesenteroides, 3, 4-dihydroxyphenyl-L-alanine, 2-bromoisobutyric acid, dicyclohexyl carbodiimide (DCC) N-hydrosuccinylimide, copper (I) bromide (99.999%), 2,2'-bipyridine (BPY 99%), and tetrahydrofuran (THF HPLC grade) were purchased from Sigma-Aldrich. 1-Ethyl-3-[3-dimethylaminopropyl]carbodiimide hydrochloride (EDC) was purchased from Pierce Biotechnology, Inc. Tetrabutylammonium fluoride (TBAF, 1 M solution in THF containing ca 5% water), 1,3-diamino-2-hydropropane, diisopropylethylamine (DIEA), tert-butyl chlorodimethylsilane (TBDMS, 98%) and *N*-hydroxysulfosuccinimide

(NHS) were purchased from Acros organics. Cyclo[Arg-Gly-Asp-$_D$-Tyr-Lys] (cRGD) was purchased from Peptides International. Tetrahydrofuran (THF) and hexane were purchased from J. T. Baker. Pooled human blood serum was purchased from BioChemed Services. The carboxybetaine methacrylate (CBMA) monomer was synthesized using the method reported previously [12].

2.2.2 Synthesis of $DOPA_2(TBDMS)_4$-Br initiator

Figure 2-1 illustrates the synthesis of $DOPA_2(TBDMS)_4$-Br initiator. $DOPA_2(TBDMS)_4$-NHS and 2-aminoethyl 2-bromoisobutyrate were synthesized as reported previously [27-29]. To prepare the initiator, $DOPA_2(TBDMS)_4$-NHS (1032mg, 1.00mM) was dissolved in 5mL dry N,N-Dimethylformamide (DMF), and the trifluoroacetic acid salt of 2-aminoethyl 2-bromoisobutyrate (339mg, 1.00mM) was added under N_2 protection. The mixture was stirred on an ice bath before DIEA (385 μL, 2.2mM) was added via a syringe. After 1 h, the mixture was warmed to room temperature and stirred overnight , and then 40 mL 5% aqueous HCl was added. The mixture was extracted with 30 mL ethyl acetate, and the organic phase was washed with 30 mL DI water, dried, and concentrated *in vacuuo*. The crude product was purified on a silica gel column with chloroform and 1 % methanol as an eluent. The product, 2-bromoisobutyric acid $DOPA_2(TBDMS)_4$-amino ethyl ester was obtained as a white foam, (1.03 g, 91%). 1H-NMR($CDCl_3$), δ: 6.60-6.82(m, 6H), 6.38-6.44(m, 2H), 4.64-4.67(m, 2H), 4.12-4.19(m, 2H), 4.09-4.11(m, 1H), 3.14-3.60 (m, 3H), 2.66-3.04(m, 3H), 1.95(d, 6H), 1.31(s, 9H), 1.0 (m, 36H) 0.2 (m, 24 H).

2.2.3 Synthesis of $DOPA_2$-PCBMA

$DOPA_2(TBDMS)_4$-Br initiator (52mg, 0.05 mM), BPY (44mg, 0.29 mM), CuBr (13.6 mg, 0.094 mM), and $CuBr_2$ (1.03 mg, 0.005mM) were placed in a 50 mL flask and degassed three times. 1 mL degassed DMF was then added to dissolve the reactants. Then, 1.0 g CBMA, dissolved in degassed H_2O/DMF (2mL/7mL), was added into the flask while stirring to start the reaction. Polymerization was conducted at room temperature for 10 h. The resultant was purified by dialysis for three days against pure water. The purified polymer was lyophilized to white powder.

Both DOPA groups of the $DOPA_2$-PCBMA polymer were protected by TBDMS groups. Before the polymer was coated onto MNPs, the TBDMS groups were removed with TBAF in THF and reacted for 12 h. The deprotected polymer was purified by THF three times and dried under vacuum at room temperature. The molecular weight and molecular weight distribution of the polymer were measured with gel permeation chromatography (GPC). The number average molecular weight (Mn) was 80.8 kDa (using PEG standards) and the polydispersity index (PDI) was 1.22.

2.2.4 Preparation of Uncoated, Dextran Coated and $DOPA_2$-PCBMA Coated MNPs

Water-soluble uncoated MNPs (Fe_3O_4) were prepared by a classical co-precipitation method [30]. Briefly, $FeCl_2 \cdot 4H_2O$ and $FeCl_3 \cdot 6H_2O$ were precipitated by adding $NH_3 \cdot H_2O$ under the protection of pure nitrogen gas. The resultant was washed 5 times by DI water and collected with a permanent magnet. During this procedure, any small particles with poor mobility to the magnet were removed. The homogenous colloid was filtered by

a 0.2 μm membrane and stored for further use. Similar to the preparation of uncoated NPs, dextran-coated MNPs were prepared by adding $NH_3 \bullet H_2O$ to precipitate $FeCl_2 \bullet 4H_2O$ and $FeCl_3 \bullet 6H_2O$ at the presence of dextran. To prepare $DOPA_2$-PCBMA coated MNPs, 20mg unprotected $DOPA_2$-PCBMA polymer was dissolved in 5mL DI water and stirred for 1 h before 5mg uncoated MNPs were added. The mixture was stirred for another 2 h and then washed three times with DI water.

2.2.5 Characterization of MNPs

The morphology of PCBMA-$DOPA_2$-MNPs was characterized by transmission electron microscope (TEM, Tecnai G2 F20, FEI). Magnetic properties were measured by a superconducting quantum interference device (SQUID) (MPMS-5S, Quantum Design). The hydrodynamic size of the particles was analyzed with a dynamic light scattering (DLS) particle sizer (Nano ZS, Zetasizer Nano, Malvern). The concentration of all MNP samples was determined by inductively coupled plasma atomic emission spectroscopy (ICP-AES, Elan DRC-e, PerkinElmer).

2.2.6 Stability Studies

To evaluate the stability of various MNPs, uncoated, dextran-coated and $DOPA_2$-PCBMA coated MNPs were mixed in PBS, 10% NaCl, or 100% human blood serum. The particle size was continuously monitored by DLS. Tests in serum were conducted at 37^oC to mimics physiological conditions.

2.2.7 Cytotoxicity Assay

The cell viability of HeLa, macrophage, and HUVEC cells was tested by a typical

MTT method using a Vybrant® MTT Cell Proliferation Assay Kit (Molecular Probes). Cells were seeded in 96-well cell culture plates in 200 μL medium with serum under 5% CO^2 at 37^{o}C to allow 80-90% confluence. On the day of the test, cells were washed with PBS and incubated with 200 μL fresh medium containing nanoparticles at various concentrations. After 24 h, cells were washed with PBS and incubated with 100 μL medium and 50 μl of 12 mM MTT stock solution for another 4 h. Then, the medium was removed and 150 μL DMSO was added and incubated for 10 min. The absorbance at 570 nm was read with a 96-well plate reader (SpectraMax M5, Molecular Devices).

2.2.8 Macrophage Cell Uptake

Similar to what has been reported previously [26], RAW 264.7 cells were cultured in DMEM medium with 10% FBS and 1% antibiotics in a 6-well plate. Prior to the test, cells were washed with PBS three times, and then various types of nanoparticles in culture media (concentration 10 mg Fe /mL) were added. After 4 h incubation at 37 ^{o}C, 5% CO_2, cells were washed three times with PBS and lysed with 1 mL of 50mM NaOH solution [31]. Intracellular iron content was determined by the ICP-MS method.

2.2.9 Functionalization of PCBMA-DOPA2-MNPs

5mg PCBMA-$DOPA_2$-MNPs were dispersed in 2mL DI water. 3mg EDC and 0.5mg NHS were then added successively. The mixture was stirred for 0.5 h and then washed two times by DI water. After that, the nanoparticles were re-dispersed in 2mL DI water, and 0.05mg of RGD peptide Cyclo[Arg-Gly-Asp-$_D$-Tyr-Lys] was added. The mixture was stirred for another 3 h at room temperature. The final product was washed three times

with DI water.

2.2.10 Magnetic Resonance Imaging

All MRI studies were conducted on a 3 T whole body scanner (Philips Achieva R2.6.1, Best, Netherlands). An eight-channel receive-only head coil was used for signal acquisition because of its high signal-to-noise ratio (SNR). The spin-spin (T_2) transverse relaxation time was acquired by a multi-echo turbo spin echo (TSE) sequence as described previously [32]. PCBMA-DOPA$_2$-MNPs at various concentrations were scanned using the following parameters: TR 3000 ms, TE 7-224 ms in steps of 7 ms, field of view (FOV) 140 x 120mm^2, matrix size 188 x 160, slice thickness 10 mm, number of signal average 1, acquisition bandwidth 250Hz/pixel, and total scan time is 5'21".

T_2 maps were generated from the multi-echo TSE images using a custom-programmed algorithm coded in MATLAB (Mathworks, Natick, MA). The T_2 relaxation time of each sample was measured using a custom-made image processing software CASCADE [33]. Images were loaded into the software and then a region of interest (ROI) of no smaller than 2cm^2 was carefully delineated within the boundary of the samples of interest. The average T_2 relaxation time of the sample was then measured automatically by CASCADE.

2.2.11 HUVEC Cell Targeting

HUVEC cells were cultured in Medium 200 supplemented with low serum growth supplement in a 6-well plate. First, cells were washed by PBS for three times. Then, PCBMA-DOPA$_2$-MNPs with or without RGD peptide in fresh culture media

(concentration 10 or 20 mg Fe /mL) were added. After 4 h incubation, cells were washed three times with PBS and lysed with 1 mL of 50mM NaOH solution. Intracellular iron content was determined by the ICP-MS method. MRI images of different cell samples were also taken by the 3T MRI instrument using the similar T_2-weighted sequence as described above.

2.3 Results and Discussion

2.3.1 Preparation and Physical Properties of PCBMA-DOPA$_2$-MNPs

Co-precipitation and thermal decomposition are the two major categories of methods to prepare MNPs [17]. In previous studies, DOPA-conjugated molecules were normally coated onto MNPs prepared by thermal decomposition. In this work, PCBMA-DOPA$_2$ was attached onto MNPs prepared by co-precipitation. The composition of the magnetic core and the formation of PCBMA-DOPA$_2$-MNPs are illustrated in Figure 2-2. The TEM image (Figure 2-3) confirms the structure of PCBMA-DOPA$_2$-MNPs. Each magnetic core is formed by a number of Fe_3O_4 nanocrystals with a single crystal size of ~15nm. The hydrodynamic size of the magnetic cores is ~70nm, as measured by DLS. With a DOPA$_2$-PCBMA coating, the hydrodynamic size of the nanoparticles increased to ~130nm. Multi-crystal cores are preferred for magnetic targeting [33], since it has been reported that without inter-particle aggregation, the small Fe_3O_4 nanocrystals have very poor mobility under a normal magnetic gradient [34]. Negligible hysteresis in the magnetization curve in Figure 2-4a reveals that at room temperature PCBMA-DOPA$_2$-MNPs possess surperparamagnetic property, indicating that the

nanoparticles present no coercivity (Hc) or remnant magnetization (Mr) in the absence of an external magnetic field. The SQUID magnetometer test also proves that our product has a saturation magnetization (Ms) of 110.2 emu/g Fe, which is 1.6 times higher than that of the commercial product, Feridex® [35]. Ms is mainly determined by the Fe_3O_4 nanocrystal size, and the strong Ms of our product is due to the fact that the size of nanocrystals (~15nm) is much larger than that of Feridex® (~4.8nm), but still in the range of superparamagnetic size (<25nm) [36]. The multi-crystal cores with larger crystal sizes render PCBMA-$DOPA_2$-MNPs highly responsive to a magnetic field [37], as shown in Figure 2-4b. Most nanoparticles were attracted to the permanent magnet side about 1 min. The superparamagnetic property and magnetization of the nanoparticles are demonstrated in Figure 2-2.

To ascertain the ability of PCBMA-$DOPA_2$-MNPs to enhance magnetic resonance imaging, the R_2 transverse relaxivity was measured by a clinical 3T MRI instrument. The quantitative results in Figure 2-5a show that the R_2 relaxivity is 428 mM^{-1} s^{-1}, which is about two times higher than that of Feridex® at a 3T magnetic field [35]. The high relaxivity is also due to the strong Ms of PCBMA-$DOPA_2$-MNPs [38]. Figure 2-5b visually presents the T_2-weighted MR images of MNPs samples with different iron concentration. The darkness of the images is dependent on iron concentration and decreases as iron concentrations increases. These results reveal the ability of PCBMA-$DOPA_2$-MNPs to be used as a T_2-weighted MR contrast agent.

2.3.2 Stability Studies

Uncoated MNPs can achieve long-term stability in DI water due to their surface charge. However, when mixed in solutions of higher ionic strengths such as PBS or 10% NaCl solution, they aggregate immediately and their hydrodynamic size increases to several thousand nanometers because their surface electronic double layer was significantly compressed by the ionic environment [3]. With the $DOPA_2$-PCBMA coating, MNPs are stable in PBS or high ionic strength solutions such as 10% NaCl for at least 6 months without any size change monitored by DLS, as shown in Figure 2-6. This result also verifies the stable formation of the PCBMA-coated MNPs.

To evaluate the stability of PCBMA-$DOPA_2$-MNPs in blood, the particles were suspended in 100% human blood serum at 37 ^{o}C. Dextran-coated MNPs and uncoated MNPs were used as controls. Results are shown in Figure 2-7. The size of uncoated MNPs increased to ~250 nm as soon as they entered the simulated blood environment. However, their size did not continue increasing to several thousand nanometers as they did in PBS and 10% NaCl solutions. This phenomenon is likely due to the formation of relatively stable particles coated with serum proteins with a size of ~250nm. Dextran-coated MNPs showed notable size increase soon after they entered the 100% human blood serum. The size increase could be due to proteins adsorption from blood serum because the anti-fouling ability of dextran is limited. In contrast, no obvious size change could be observed for the PCBMA-$DOPA_2$-MNPs sample over the entire time-course of the test, indicating the excellent stability and ultra-lowfouling ability of the nanoparticles.

2.3.3. *In vitro* Studies

Resistance to macrophage cell uptake is also important to evaluate nanoparticles *in vitro*, because it can indicate the *in vivo* response of the innate immune system to the nanoparticles [26]. Before cell uptake studies, the cytotoxicity of PCBMA-DOPA$_2$-MNPs was evaluated by an MTT assay and results are as shown in Figure 2-8. No significant cell viability decrease can be observed at the tested concentration range. Mouse macrophage cell line, RAW 264.7 cell, was used in this work. As shown in Figure 2-9, uptake of PCBMA-DOPA$_2$-MNPs by macrophage cell is much lower than that of dextran-coated MNPs and uncoated MNPs. This test further shows the advantage of the PCBMA coating. It is possible that PCBMA-DOPA$_2$-MNPs can achieve a longer circulation half-life time than dextran coated MNPs.

Another important issue in the development of multifunctional MNPs is that the nanoparticles should be functionalizable [20]. We have shown previously that the abundant carboxyl groups in PCBMA can be efficiently and easily conjugated to biomolecules by conventional EDC/NHS chemistry. Furthermore, activated but unreacted NHS groups will be hydrolyzed back to carboxyl groups as a part of non-fouling zwitterionic groups [10], ensuring that the excellent nonfouling properties of the coating is maintained in post-functionalized surfaces. In this study, a RGD peptide, Cyclo[Arg-Gly-Asp-$_D$-Tyr-Lys], was adopted as the targeting ligand and conjugated to PCBMA-DOPA$_2$-MNPs. HUVEC cells were used to test the targeting efficiency of the MNPs by means of measuring intracellular iron concentrations. As shown in Figure 2-8,

at both Fe concentrations (10 μg Fe/mL and 20 μg Fe/mL) tested, non-functionalized PCBMA-DOPA$_2$-MNPs have a very low uptake level, similar to macrophage cell studies. In contrast, RGD-PCBMA-DOPA$_2$-MNPs show much higher uptake levels. T_2-weighted MR images visually confirmed the uptake of MNPs, as shown by the insert figure in Figure 2-10, the cell sample treated with functionalized MNPs at 20 μg Fe/mL shows much higher contrast compared with the nonfunctionlized one. These results demonstrate the successful conjugation of RGD with the nanoparticles and the notable active targeting efficacy of PCBMA-DOPA$_2$-MNPs after loaded with a targeting ligand.

2.4 Conclusions

In this work, we present a convenient method to efficiently coat MNPs with the zwitterionic PCBMA with adhesive 3,4-dihydroxyphenyl-L-alanine linkages. The superior stability of PCBMA-coated MNPs in ionic solutions and undiluted human blood serum, along with their ultra-low macrophage cell uptake suggest that PCBMA-DOPA$_2$-MNPs could achieve long blood circulation half-life *in vivo*. In addition, these nanoparticles possess high mobility in the presence of an external magnetic field due to their multi-crystal cores. Importantly, the PCBMA coating can be easily functionalized by target ligands via simple NHS/EDC chemistry. These features enable them to take advantages of both passive targeting (by a magnetic field) and active targeting (by targeting ligands). Thus, multifunctional PCBMA-DOPA$_2$-MNPs hold great promise as a MRI detectable, high efficient targeting delivery carrier.

Figures

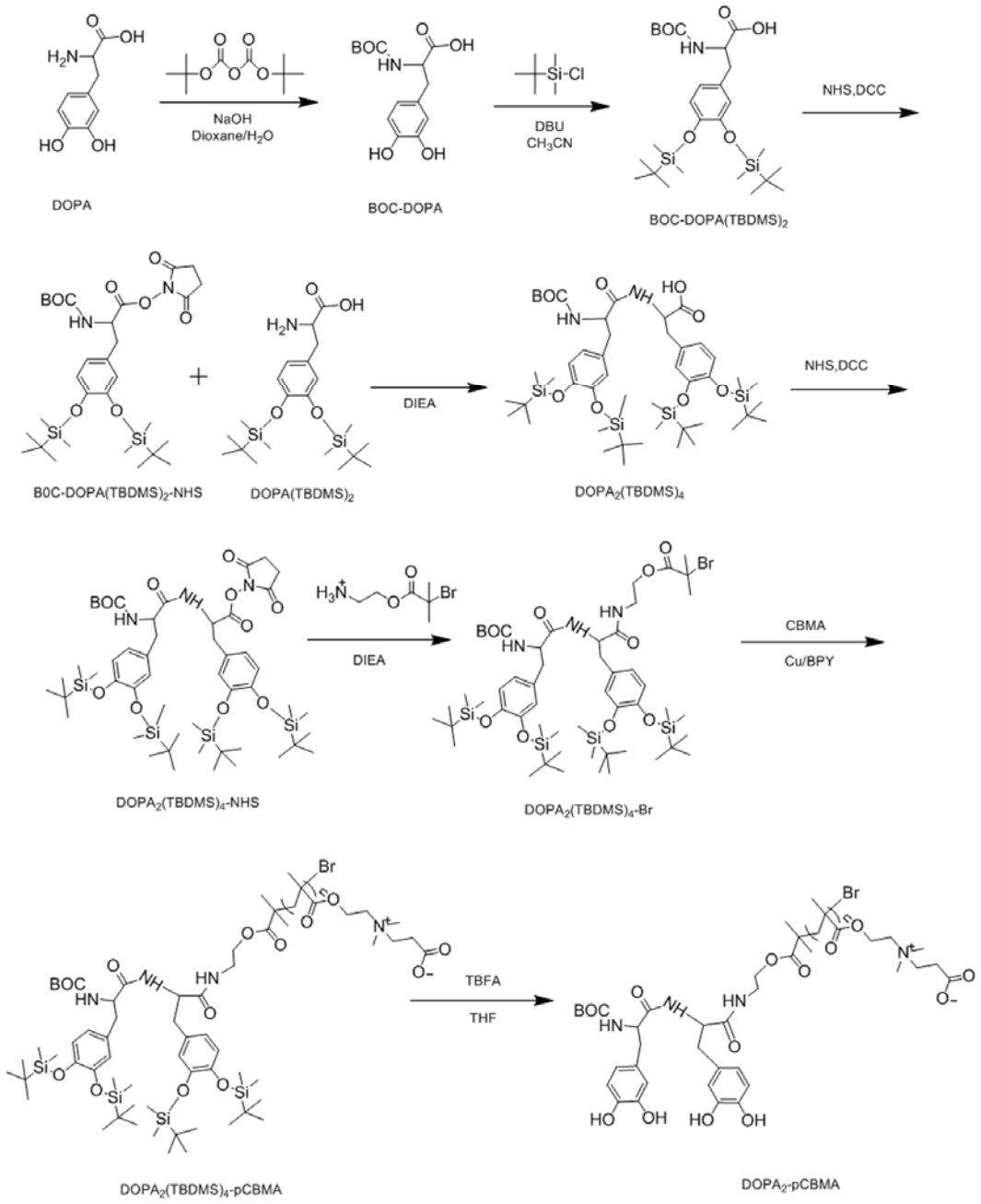

Figure 2-1. Synthesis of $DOPA_2(TBDMS)_4$-Br initiator and polymerization of $DOPA_2$-PCBMA.

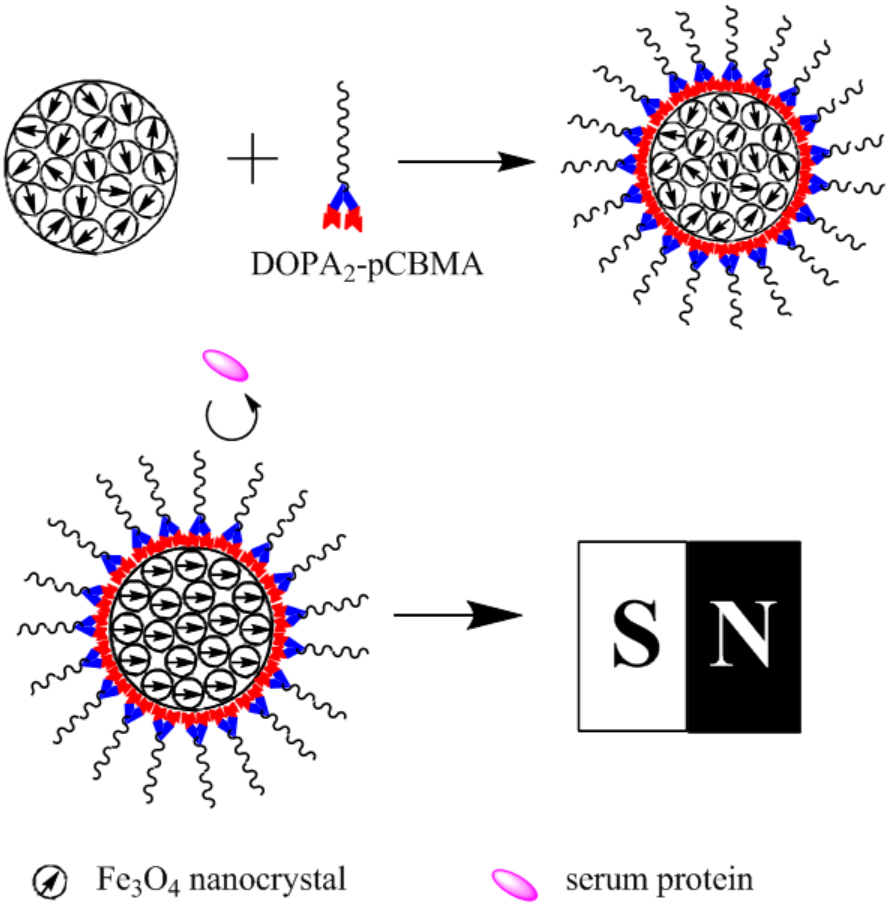

Figure 2-2. Preparation of PCBMA-DOPA$_2$-MNPs and their magnetization in the presence of a permanent magnet.

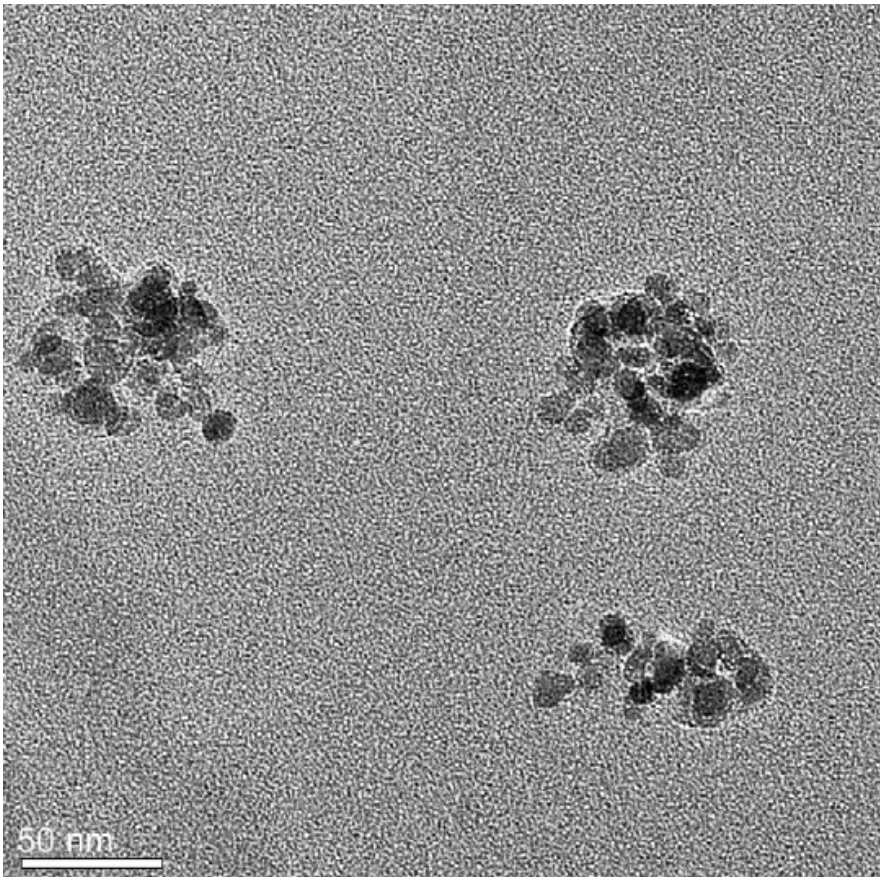

Figure 2-3. TEM image of PCBMA-DOPA$_2$-MNPs, scale bar = 50 nm.

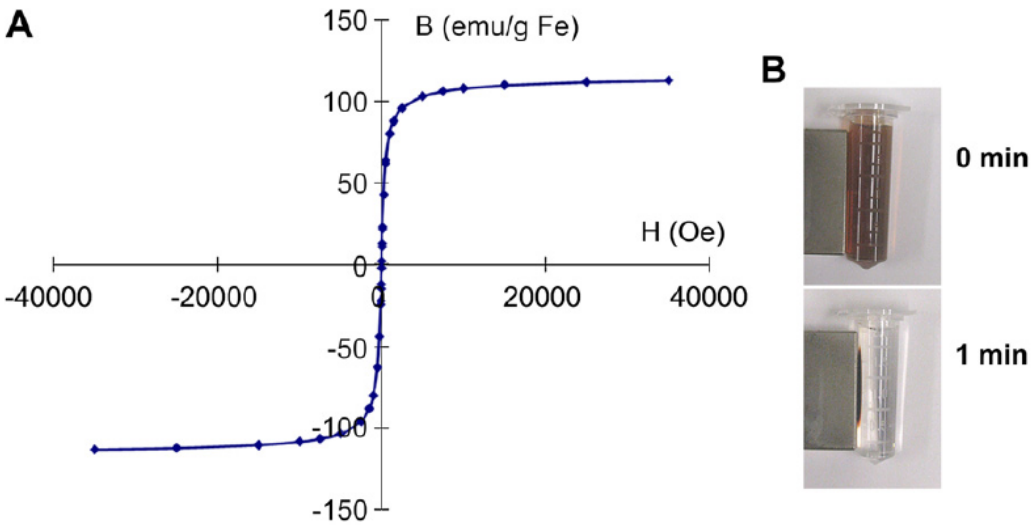

Figure 2-4. Magnetic properties of PCBMA-DOPA$_2$-MNPs: (A) Hysteresis loop of the MNPs measured by a SQUID magnetometer; (B) Most MNPs were collected by the magnetic about 1 min under a permanent magnet.

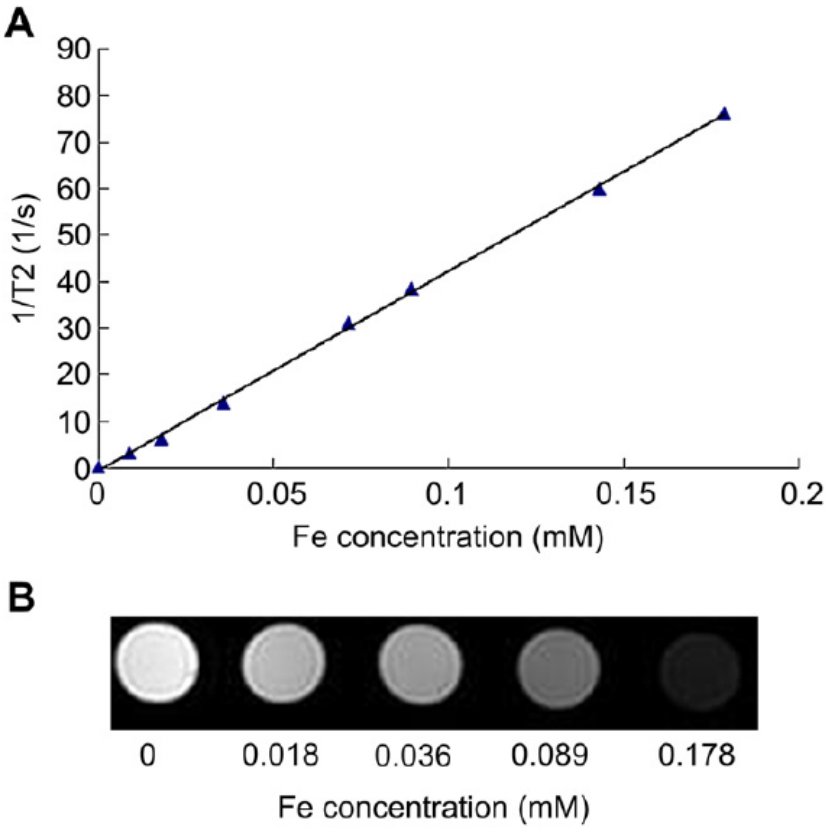

Figure 2-5. (A) R_2 relaxivity of PCBMA-DOPA$_2$-MNPs as a function of Fe concentration. (B) T_2-weighted MR images of PCBMA-DOPA$_2$-MNPs at different Fe concentrations.

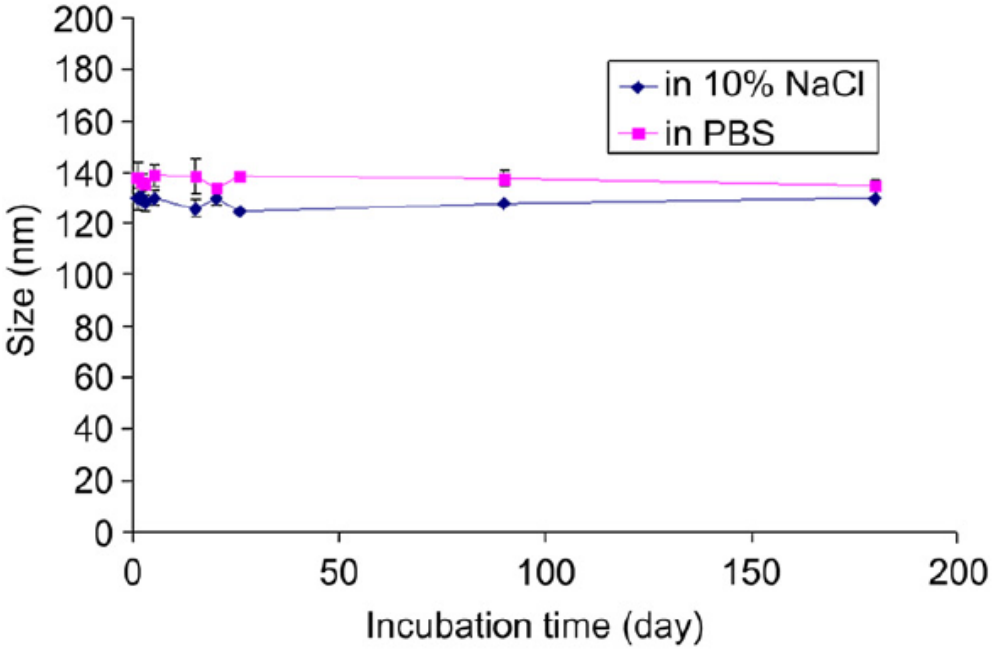

Figure 2-6. Stability test of PCBMA-DOPA$_2$-MNPs in 10% NaCl and PBS solution by DLS (n=3).

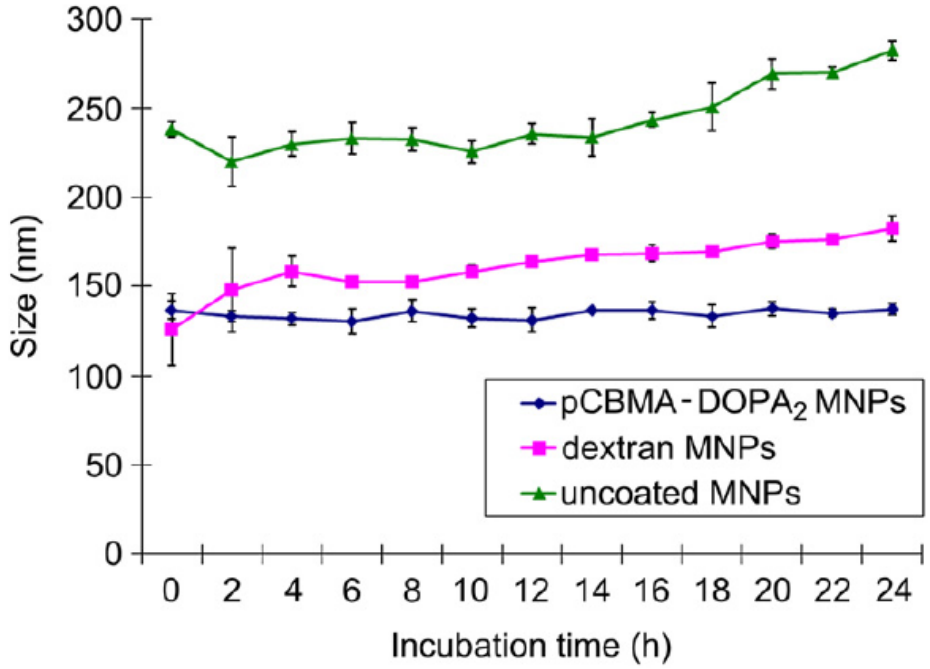

Figure 2-7. Stability of uncoated MNPs, dextran-coated MNPs and PCBMA-$DOPA_2$-MNPs in 100% human blood serum, continuously measured by DLS at 37 ^{o}C (n=3).

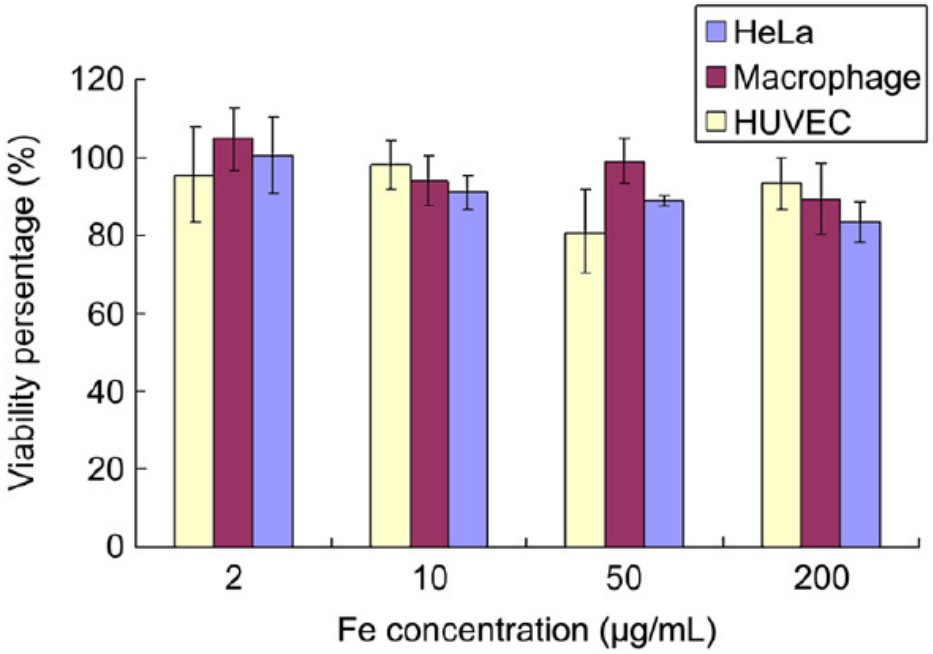

Figure 2-8. Cytotoxicity of PCBMA-DOPA$_2$-MNPs to HeLa, macrophage and HUVEC cells by MTT assay (n=3).

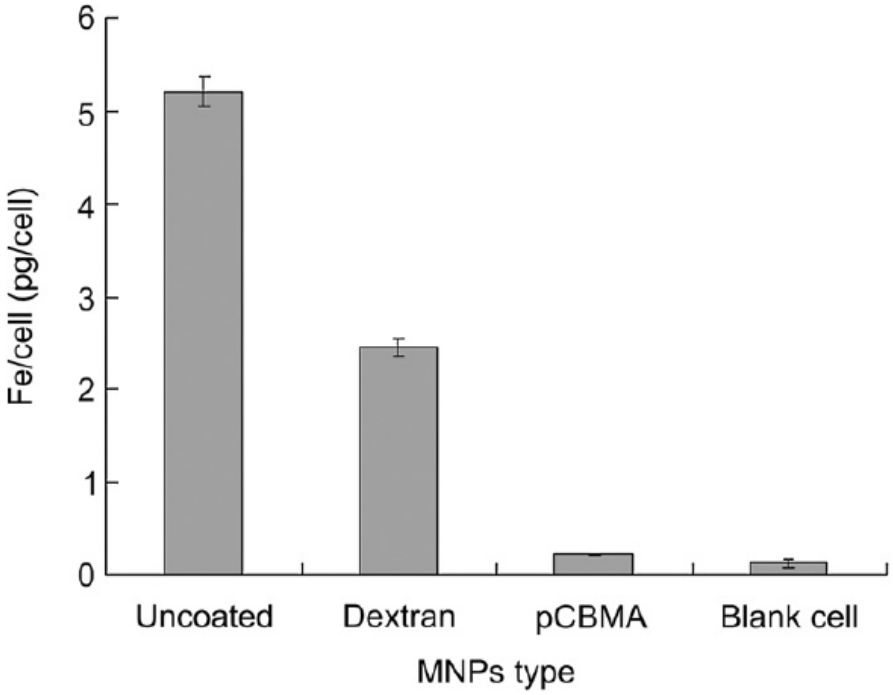

Figure 2-9. Macrophage cell uptake of uncoated MNPs, dextran-coated MNPs, and PCBMA-$DOPA_2$-MNPs at the Fe concentration of 10 μg Fe/mL (n=3).

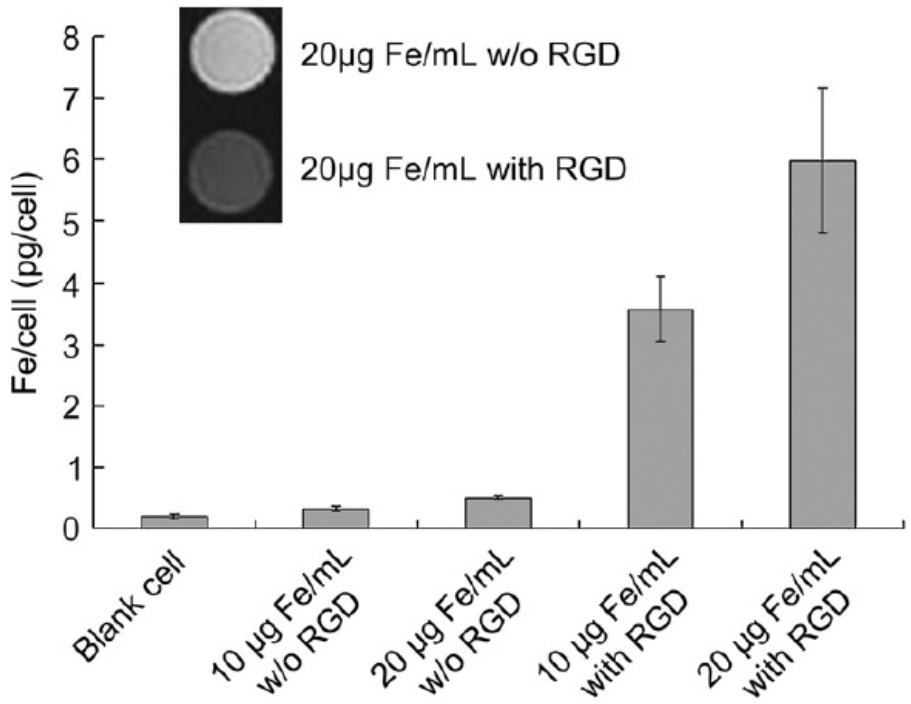

Figure 2-10. HUVEC cell uptake of PCBMA-DOPA$_2$-MNPs with or without RGD peptide at two different Fe concentrations (10 μg Fe/mL and 20μg Fe/mL, n=3). The insert figure shows T_2-weighted MR images of cell samples treated with PCBMA-DOPA$_2$-MNPs with or without RGD peptide at 20 μg Fe/mL

Chapter 3 Multifunctional and Degradable Zwitterionic Nanogels

Multifunctional and degradable nanogels encapsulating both model drug (fluorescently labeled dextran) and imaging reagent (monodisperse Fe_3O_4 nanoparticles) were developed by polymerizing zwitterionic monomers with a disulfide crosslinker. Results show that the nanogels have a hydrodynamic size of about 110 nm in saline solution and their size remained unchanged for over 6 months. After being conjugated with a targeting ligand, the nanogels showed a significant cellular uptake by human umbilical vein endothelial cells. The nanogels show low macrophage uptake, implying potential low interaction with the innate immune system. Upon entering the reducing intracellular environment, the disulfide bonds were efficiently cleaved, resulting in the spontaneous release of the encapsulated model drug and Fe_3O_4 nanoparticles. Magnetic resonance imaging (MRI) studies show that the encapsulation of multiple monodisperse Fe_3O_4 nanoparticles by the nanogels significantly enhanced their MRI performance (R2 relaxivity), while the disassembling of the Fe_3O_4 nanoparticles due to the nanogels degradation brings their R2 relaxivity back to that of their original monodisperse form. Furthermore, the degradation properties enable the removal of the disassembled nanogels from the body by renal clearance.

3.1 Introduction

Multifunctional nanoparticles (NPs) have been extensively studied in the field of

targeting drug delivery due to their great potential to work as carriers for both imaging and therapy [3, 20, 21, 30]. However, a successful and sophisticated multifunctional nanoparticle-based drug delivery system should have the following properties: first, it should have high therapeutic drug loading and could release its payload at the target site; second, it should have long *in vivo* circulation half-life and can target a specific site after administration to reduce side effects to other healthy tissues; third, it should load imaging reagent for non-invasive imaging to monitor the targeting and therapeutic efficiency; and last, they should be degradable and removable from the body (e.g., via renal clearance) to avoid possible toxicity and side-effects [39-41].

Recent advances in material development have been greatly improving the design and fabrication of multifunctional nanoparticles that can fulfill the above stated criteria. We have shown that zwitterionic polymers are an ideal class of material to develop nonfouling surfaces and stealth nanoparticles [4]. Among various zwitterionic materials, polycarboxybetaine methacrylate (CBMA) is of particular interest due to its ultra-low fouling and functionalizable properties. It has been successfully used to modify a variety of nanoparticles, such as silica [42], gold [43] , Fe_3O_4[6], poly(lactic-co-glycolic acid) (PLGA) [44], and hydrogel NPs (nanogels) [45]. These NPs could achieve long-term stability in different protein solutions and/or undiluted blood serum. Besides working as a stabilizer and an anti-fouling coating, PCBMA can also provide abundant –COOH groups, which can be easily linked to targeting ligands or other functional molecules via conventional conjugation chemistry. These properties render PCBMA an ideal material to

construct multifunctional NPs. For example, PCBMA coated Fe_3O_4 NPs can be ultra stable in biological media and can evade the innate immune system. After being conjugated to a RGD peptide, the uptake of these Fe_3O_4 NPs by HUVEC cells was significantly enhanced, and could be visualized by magnetic resonance imaging (MRI) [6].

In this work, multifunctional PCBMA nanogels encapsulating monodisperse Fe_3O_4 magnetic NPs (MNPs) as a MRI contrast reagent and fluorescently labeled dextran as a model drug were synthesized using a reduction-sensitive crosslinker.

3.2 Experimental

3.2.1 Materials

2-(Dimethyl amino)ethyl methacrylate (DMAEMA), oleic acid (90%), $FeCl_3 \cdot 6H_2O$ (99%), dithiothreitol (DTT, 99%), cetyltrimethylammonium bromide (CTAB, 95%), phosphate buffered saline (PBS), Span 80, Tween 80, and fluorescein isothiocyanate-dextran (FITC-dextran) (MW 20 000) were purchased from Sigma-Aldrich. L-Cystine (98%), sodium oleate were purchased from TCI America. β-propiolactone (97%) was purchased from Alfa Aesar. 1-Ethyl-3-[3-dimethylaminopropyl]-1 carbodiimide hydrochloride (EDC) was purchased from Pierce Biotechnology, Inc. N-Hydroxysulfosuccinimide (sulfo-NHS) was purchased from Acros Organics. Cyclo[Arg-Gly-Asp-D-Tyr-Lys] (cRGD) was purchased from Peptides International. 2,20-Azobis(4-methoxy-2.4-dimethyl valeronitrile) (V-70) was purchased from Wako Pure Chemical Industries. The disulfide (reduction-sensitive)

crosslinker, L-cystine bisacrylamide, was synthesized according to literatures reported method[46]. The CBMA monomer was synthesized by the reaction of DMAEMA and β-propiolactone using a method published previously [44].

3.2.2 Synthesis of monodisperse MNPs

Monodisperse MNPs (9 nm) were synthesized by the thermal decomposition method[47]. Iron-oleate complex was firstly synthesized by reacting 5.4 g iron chloride and 18.25 g sodium oleate in a mixture solvent composed of 40 mL ethanol, 30 mL distilled water and 70 mL hexane at 70 °C for 4 h. The product was washed 3 times with DI water, the hexane was then evaporated off. After that, 18 g iron-oleate complex and 2.85 g oleic acid were dissolved in 100 g 1-octadecene, the solution was stirred vigorously and gradually heated to 320 °C, and then held for 20 min. After the mixture cooled to room temperature, pure ethanol was used to precipitate the NPs, the final MNPs were dispersed in hexane.

To prepare water soluble monodisperse MNPs, 1 mL NPs in hexane solution (10 mg/mL) was mixed with 10 mL water and 0.5 g CTAB[48]. The mixture was sonicated and stirred vigorously for 30 min, the hexane solvent was then evaporated from the mixture. The resulting water soluble NPs were washed 3 times with DI water using a 100 kD molecular-weight-cutoff Amicon Ultra centrifugal filter device (Millipore) and filtered by a 0.2 μm syringe filter .

3.2.3 Synthesis of nanogels

PCBMA nanogels loaded with MNPs and FITC-dextran were prepared by inverse

microemulsion polymerization as presented in Figure 3-1. Briefly, 0.7 g Tween 80, 0.8 g Span 80 and 4 mg V-70 were dissolved in 20 mL of hexane and kept in an ice bath. 10 mg monodisperse MNPs, 10 mg FITC-dextran, 115 mg CBMA and 5 mg disulfide crosslinker were dissolved in 0.5 mL of DI water. The two stock solutions were mixed in a 100 mL flask with vigorous stirring, then strong sonication was applied to form the microemulsion. The flask was purged with nitrogen at 4 ^{o}C for 30 min to remove dissolved oxygen. During polymerization, the reaction was kept at 40 ^{o}C with stirring and was protected under nitrogen for 4 h. After the reaction, the product was washed with tetrahydrofuran (THF) 3 times to remove the surfactants, then the product was dispersed in DI water and other impurities were removed using a 100 kD molecular-weight-cutoff Amicon Ultra centrifugal filter. The final nanogel product was collected using a permanent magnet.

3.2.4 Characterization of nanogels

The morphology of nanogels was characterized by scanning electron microscope (SEM, Sirion, FEI). The hydrodynamic size of all the particles was analyzed with a dynamic light scattering (DLS) particle sizer (Nano ZS, Zetasizer Nano, Malvern). The Fe concentration of the nanogel samples was determined by inductively coupled plasma atomic emission spectroscopy (ICP-AES, Elan DRC-e, PerkinElmer).

3.2.5 Cytotoxicity assay

The cell viability of macrophage cells and HUVEC cells was tested by a typical MTT method using a Vybrant® MTT Cell Proliferation Assay Kit (Molecular Probes).

Cells were seeded in 96-well cell culture plates in 200 μL medium with serum under 5% CO_2 at 37 ^{o}C to allow 80-90% confluence. On the day of the test, cells were washed with PBS and incubated with 200 μL fresh medium containing nanogels at various concentrations. After 24 h, cells were washed with PBS and incubated with 100 μL medium and 50 μL of 12mM MTT stock solution for another 4 h. Then, the medium was removed and 150 μL DMSO was added and incubated for 10 min. The absorbance at 570 nm was read with a 96-well plate reader (SpectraMax M5, Molecular Devices).

3.2.6 Functionalization of nanogels and HUVEC cells targeting

5 mg nanogels were dispersed in 5 mL DI water. 6 mg EDC and 1 mg NHS were then added successively. The mixture was stirred for 0.5 h and then washed two times with DI water. After that, the nanogels were re-dispersed in 2 mL DI water, and 0.1 mg of RGD peptide Cyclo[Arg-Gly-Asp-D-Tyr-Lys] was added. The mixture was stirred for another 3 h at room temperature. The final product was washed three times with DI water.

HUVEC cells were cultured in Medium 200 supplemented with low serum growth supplement in a 6-well plate. First, cells were washed with PBS three times. Then, nanogels with or without RGD peptide in fresh culture media were added (final Fe concentration 5 ppm or 10 ppm). After 4 h incubation, cells were washed three times with PBS and lysed with 1 mL of 50 mM NaOH solution. Intracellular iron content was determined by the ICP-MS method.

3.2.7 Macrophage Uptake Test

RAW264.7 cells were cultured in DMEM medium with 10% FBS and 1%

antibiotics in a 6-well plate. Prior to the test, cells were washed with PBS three times, and MNP loaded nanogels with or without RGD peptide (at Fe concentration of 5 ppm or 10 ppm) in culture media were added. After 4 h incubation under 5% CO_2 at 37 ^{o}C, cells were washed three times with PBS and lysed with 1 mL of 50 mM NaOH solution. Intracellular iron content was determined by the ICP-AES method.

3.2.8 Degradation test by DLS

0.1 mg of MNP and FITC-dextran loaded nanogels was dispersed in 5 mL PBS solution containing 10mM DTT, the hydrodynamic size was monitored by DLS at 37 ^{o}C. Nanogels dispersed in PBS without DTT served as the control.

3.2.9 Degradation test by MRI

All MRI studies were conducted on a 3 T whole body scanner (Philips Achieva R2.6.1, Best, Netherlands). An eight-channel receive-only head coil was used for signal acquisition because of its high signal-to-noise ratio (SNR). The spin-spin (T2) transverse relaxation time was acquired by a multi-echo turbo spin echo (TSE) sequence as described previously [6].

Monodisperse MNPs, nanogels and degraded nanogels at various Fe concentrations were scanned using the following parameters: TR 3000 ms, TE 7-224 ms in steps of 7 ms, field of view (FOV) 140 x120 mm^2, matrix size 188 x160, slice thickness 10 mm, number of signal average 1, acquisition band width 250 Hz/pixel, and total scan time is 5’21”.

T2 maps were generated from the multi-echo TSE images using a custom-programmed algorithm coded in MATLAB (Mathworks, Natick, MA). The T2

relaxation time of each sample was measured using a custom-made image processing software CASCADE. Images were loaded into the software and then a region of interest (ROI) of no smaller than 2 cm^2 was carefully delineated within the boundary of the samples of interest. The average T2 relaxation time of the sample was then measured automatically by CASCADE.

3.2.10 Release test

Two PBS stock solutions (10 mL, with or without 10mM DTT) both containing 5 mg MNPs and FITC-dextran loaded nanogels were incubated at 37 ^oC. At different time points, 0.5 mL solution from each sample solution was collected and the released FITC-dextran was obtained using a 100 kD molecular-weight-cutoff Amicon Ultra centrifugal filter. The fluorescence intensity was determined by a fluorescence spectrophotometer (F-4500 fluorescence spectrophotometer, Hitachi). The release of FITC-dextran was further tested in fetal bovine serum (FBS), using the same method as described above.

3.3 Results and discussion

The SEM image in Figure 3-2 visually shows the morphology of the PCBMA nanogels. In PBS solution, the nanogels possess a hydrodynamic size of ~110 nm determined by DLS. Hydrodynamic size is of great importance in the design of nano-carriers for targeting drug delivery: NPs larger than 150nm could be removed rapidly by liver and spleen after injection, resulting in poor *in vivo* circulation time and targeting efficiency; while NPs smaller than 20nm have been reported to be excreted

through renal clearance, which will also decrease the longevity of the NPs after injection *in vivo* [49, 50]. Thus, the hydrodynamic size of nanogels prepared in this work falls into the suitable range. We further tested the stability of nanogels in PBS in a long term study, and found the nanogels maintained the same mean diameter over six months as shown in Figure 3-3. Moreover, after lyophilized to dry powder, the nanogels can also be re-dispersed in PBS and their size (~ 110 nm) remains the same. The tests above show that the nanogels possess favorable stability for storage in both solution and solid forms.

Cytotoxicity assay was first conducted before doing the cell uptake tests. Figure 3-4 shows the cytotoxicity of the nanogels on macrophage cells and HUVEC cells. In all the concentrations tested, the nanogels didn't present obvious cytotoxicity to the cells. HUVEC cell uptake test (Figure 3-5) shows that, at two different Fe concentration levels (5 ppm and 10 ppm), the targeting efficiency was notably enhanced after the nanogels conjugated with the RGD peptide. Macrophage cell uptake test is an important and commonly used method to evaluate the response of the innate immune system to nanoparticles; non-specific macrophage cell uptake is a major reason that NPs get cleared after injection *in vivo*. Figure 3-6 shows that, at two different Fe concentration levels (5 ppm and 10 ppm), the nanogels (with or without targeting ligand, the RGD peptide) present very low cell uptake amounts, indicating the nanogels could notably evade the macrophage uptake and possibly have long circulation half-life after *in vivo* administration to the body [26, 31].

Degradation of the nanogels was first tested by DLS, as shown in Figure 3-7, by

incubating in PBS containing 10mM DTT at 37 ^{o}C. After 24 hours, the nanogels (~ 110 nm) were degraded to small products with hydrodynamic size ~ 12 nm, which is comparable to the water soluble monodisperse MNPs. This result indicates the degraded products are possibly composed of the original water soluble monodisperse MNPs and PCBMA polymer chains as shown in Figure 3-1.

Degradation of the nanogels was further evaluated by MRI test. Figure 3-8 shows the T2 tests and MR images of different samples. The original monodisperse MNPs have a transverse relaxivity (R2 relaxivity, reciprocal of the proton spin-spin relaxation time) of 39.531 mM^{-1} s^{-1}, while the MNP loaded nanogels have a R2 relaxivity of 113.12 mM^{-1} s^{-1}. This interesting phenomenon is due to the synergistic effect of assembling several monodisperse MNPs together, which could enhance the R2 relaxivity of MNPs without any change to the monodisperse MNPs themselves [51, 52]. Different methods have been used to assemble monodisperse MNPs together to form a cluster, however, less attention has been paid to disassembling clusters after they finish their task. The R2 relaxivity of degraded samples decreased to 41.56 mM^{-1} s^{-1}, indicating the complete disassembly of the encapsulated monodisperse MNPs. MR images in Figure 3-8 visually present the different contrast of the three samples, showing the different MR contrast ability of the samples, which is consistent with the T2 tests.

The release of encapsulated FITC-dextran in both PBS and FBS is shown in Figure 3-9. Results show the significant difference between the samples with or without reducing reagent (DTT). The nanogels incubated with DTT show an efficient release of

FITC-dextran. For both samples in PBS and FBS, about 80% of the payload was released over a period of 48 hours. In contrast, the nanogels incubated without DTT only appeared to have released by physical diffusion, which is much less efficient, only about 3% was released during the same 48 hours. No obvious difference was observed between the release profiles in PBS and FBS, because the release mechanism is due to the degradation of the nanogels induced by reducing agent.

These results show that the nanogels hold great promise to serve as multifunctional drug delivery carriers. It can be assumed that ultra-low fouling PCBMA polymer chains could efficiently stabilize the particles and resist the clearance of the particles after systemic administration. Meanwhile, PCBMA polymer chains can be easily functionalized with targeting ligands to enhance the accumulation of nanogels at the target site without any compromise of their stealth properties. Furthermore, the encapsulation of multiple monodisperse MNPs could dramatically enhance their MRI performance. Before the nanogels arrive at the target site and are internalized into the target cells, the loaded therapeutic reagents have a very slow release profile. However, after the nanogels enter the intracellular (reducing) environment, the disulfide crosslinkers will be cleaved, resulting in the fast release of the therapeutic payload and the imaging reagent (e.g., MNPs). Unlike some other non-degradable nano-carriers which will accumulate in the body after injection [53, 54], the nanogels in this work can be degraded into small MNPs and PCBMA polymers, which could be removed from the body by renal clearance. It has been reported that renal clearance rate is closely related to

the hydrodynamic size of the NPs, for faster removal by renal clearance, smaller sized MNPs could be used [49].

3.4 Conclusions

In this work, we demonstrated a multifunctional and degradable nanogel based on a zwitterionic polymer (PCBMA). The delicate design of the release mechanism and proper use of ultra low fouling and functionalizable PCBMA polymer greatly facilitated the performance of the nanogels. The nanogel presented in this work fulfills several important criteria of a multifunctional drug carrier, including both drug and imaging reagent loading, drug release at the target site, and removal from body after drug release. The nanogel developed in this work could potentially load other types of imaging nanoparticles with different sizes, such as water soluble quantum dots or gold NPs, or other types of hydrophilic drugs, such as proteins, DNA, or siRNA. These properties render this nanogel a safe and versatile carrier for simultaneous targeting, imaging, and drug delivery.

Figures

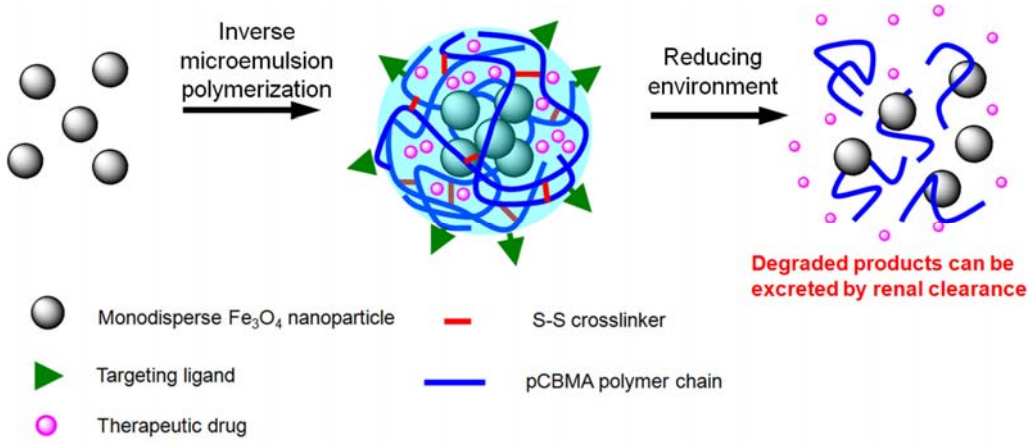

Figure 3-1. Formation and degradation of degradable PCBMA nanogels.

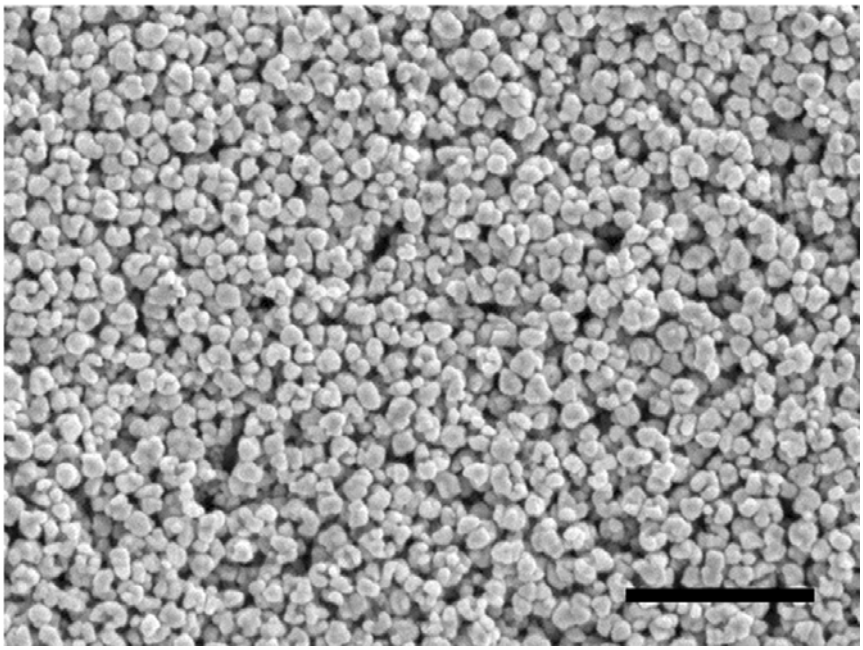

Figure 3-2. SEM image of degradable PCBMA nanogels (scale bar = 1μm).

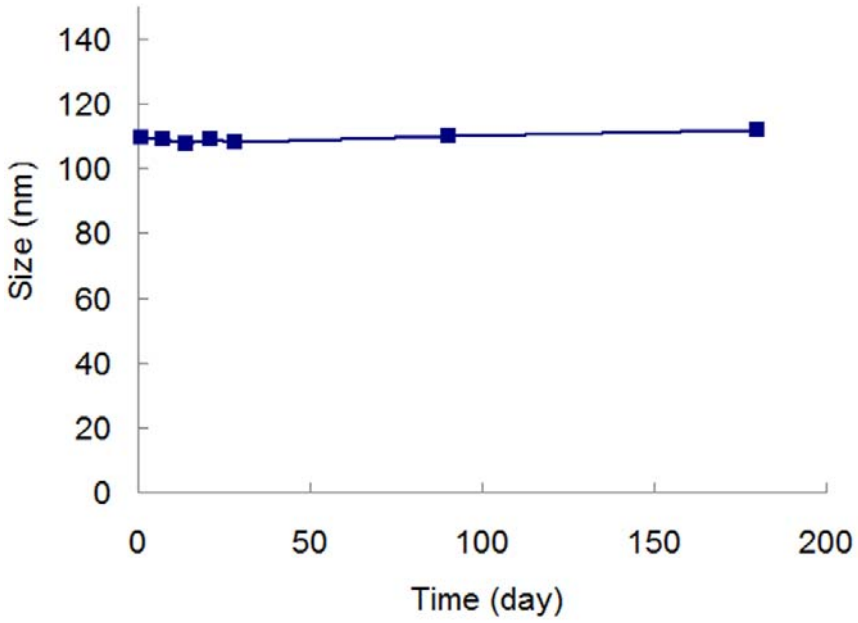

Figure 3-3. Stability of the nanogels in PBS solution monitored by DLS.

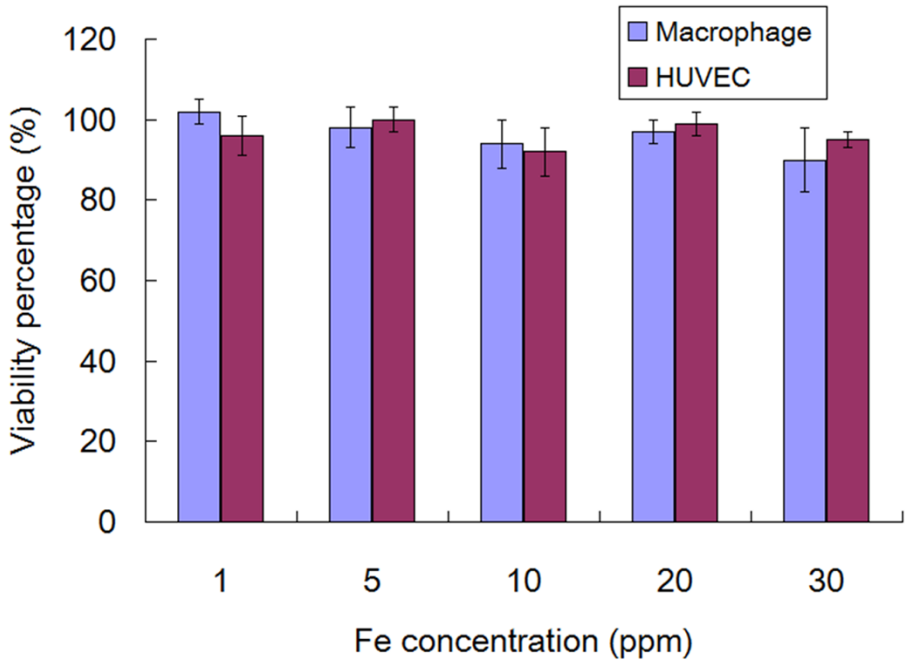

Figure 3-4. Cytotoxicity test on macrophage cells and HUVEC cells at different Fe concentrations (1, 5, 10, 20, 30 ppm, n=3).

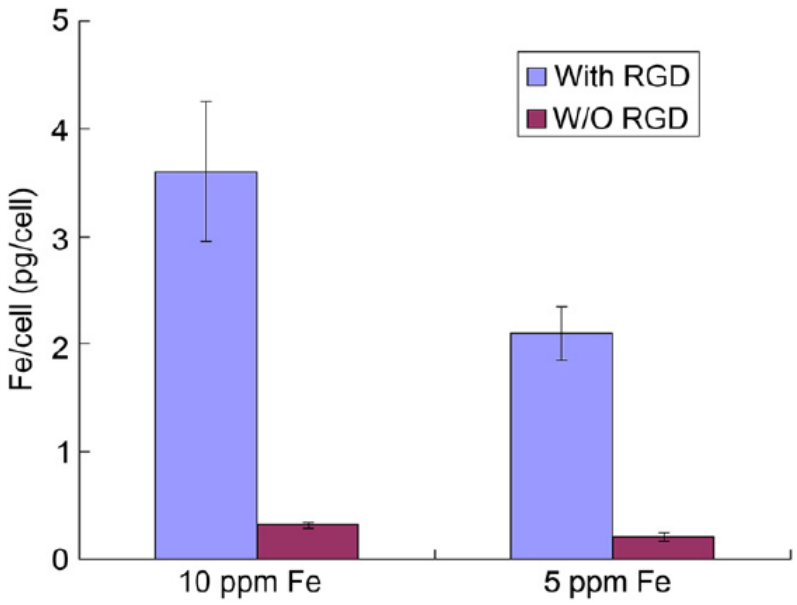

Figure 3-5. HUVEC cell uptake test of the nanogels with or without RGD peptide at two different Fe concentrations (5 ppm and 10 ppm, n = 3).

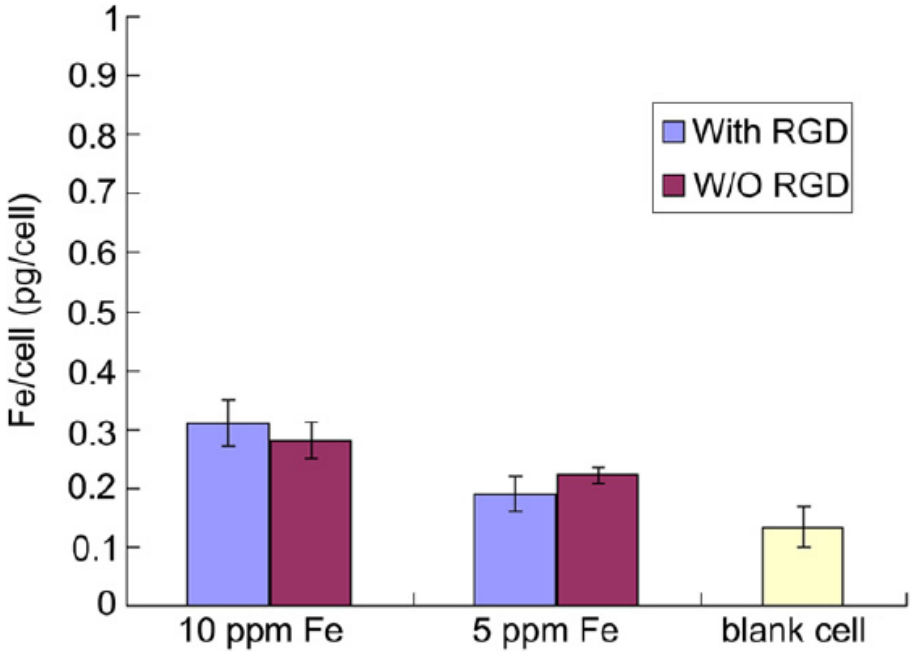

Figure 3-6. Macrophage cell uptake test of the nanogels with or without RGD peptide at two different Fe concentrations (5 ppm and 10 ppm, n = 3).

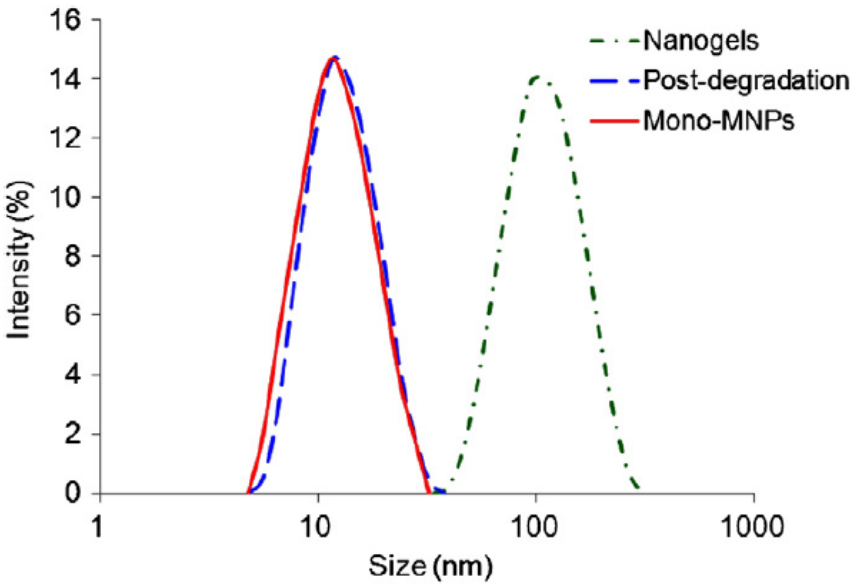

Figure 3-7. Degradation test by DLS.

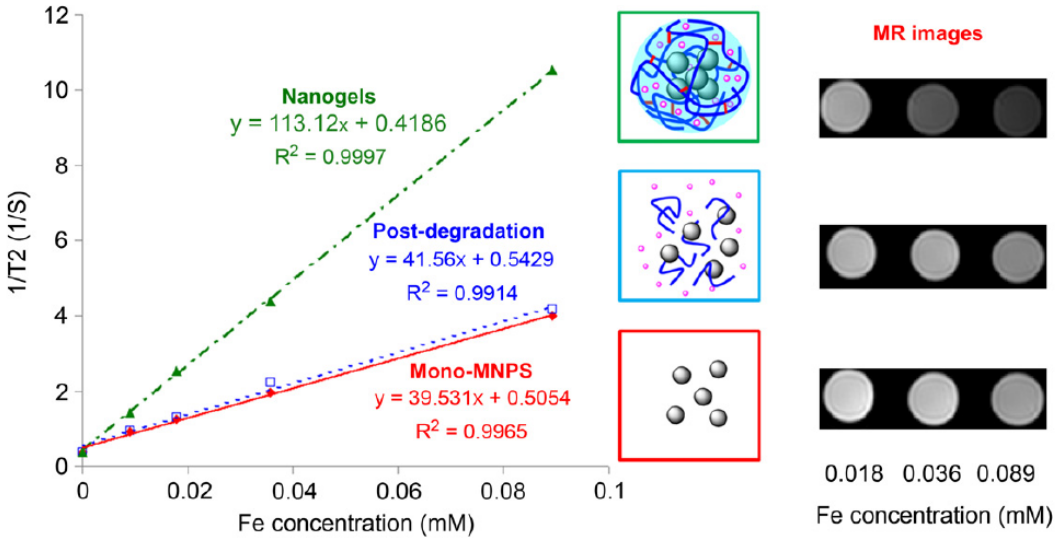

Figure 3-8. Degradation test by MRI.

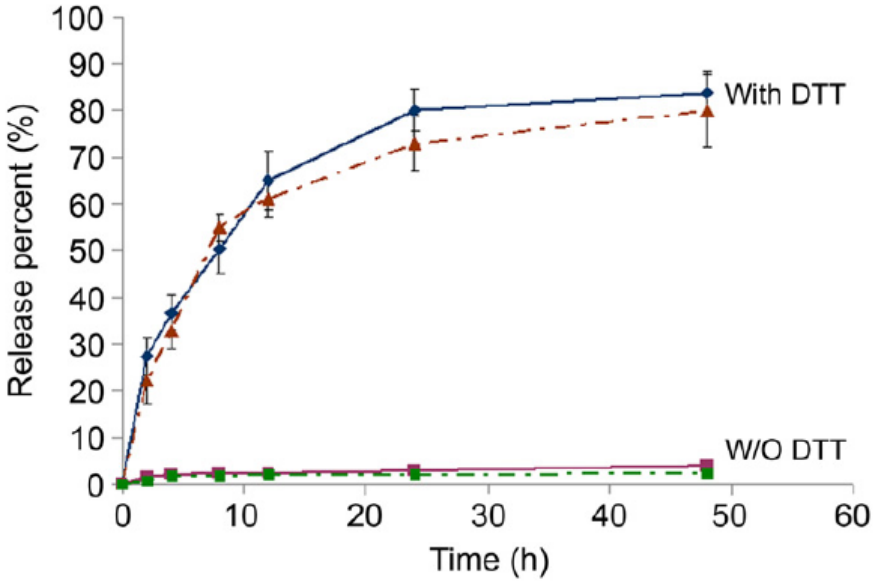

Figure 3-9. Release of FITC-dextran from nanogels in PBS (solid lines) and FBS (dash lines) with or without 10mM DTT at 37 ^{o}C (n = 3)

Chapter 4 Multifunctional Magnetic-plasmonic Nanoparticles for Fast Concentration and Sensitive Detection of Bacteria Using SERS

Multifunctional magnetic-plasmonic Fe_3O_4-Au core-shell nanoparticles (Au-MNPs) were prepared for simultaneous fast concentration of bacterial cells by applying an external point magnetic field, and sensitive detection and identification of bacteria using surface-enhanced Raman spectroscopy (SERS). We demonstrated that a spread of a 10 μL drop of a mixture of 10^5 cfu/mL bacteria and 3 μg/mL Au-MNPs on a silicon surface can be effectively condensed into a highly compact dot within 5 minutes by applying an external point magnetic field, resulting in 60 times more concentrated bacteria in the dot area than on the spread area without concentration. Surrounded by dense uniformly packed Au-MNPs, bacteria can be sensitively and reproducibly detected directly using SERS. The principle component analysis (PCA) showed that three different Gram-negative bacterial strains can be clearly differentiated. We also demonstrated that the condensed multifunctional Au-MNPs dot can be used as a highly sensitive SERS-active substrate and a limit of detection better than 0.1 ppb was obtained in detection of small molecules such as 4-mercaptopyrine. This novel platform significantly simplifies the concentration and detection process, which holds great promise for applications in food safety, environmental monitoring, medical diagnoses, and chemical and biological threat detections.

4.1 Introduction

Recently, growing interest has been paid to the development of multifunctional plasmonic magnetic nanoparticles by incorporation of gold nanostructures to superparamagnetic Fe_3O_4 nanoparticles (MNPs) that can combine both plasmonic and magnetic properties in one single nanoparticle [55]. Impinged by light, gold nanostructures such as nanodots, nanorods and nanoshells can generate extreme high local electric fields arising from local surface plasmon resonance (LSPR). This is due to collective oscillation of conduction band electrons in response to the electric field of the electromagnetic radiation of the light. Both LSPR wavelength and electric field intensity can be tuned by varying the dimensions of the nanostructures, the spacing between them and the surrounding dielectric media [56]. Therefore, metallic nanostructures have been used for bioimaging [57-59], LSPR biosensing [60], surface-enhanced Raman spectroscopy (SERS) [61], thermotherapy [59, 62, 63], and many other nanophotonic applications [64, 65].

Plasmonic MNPs have also been developed recently by many research groups with different methods. Several unique particle structures such as Fe_3O_4 core/gold shell [9, 66, 67], dumbbell-like NPs formed by attaching a Au NP to a Fe_3O_4 NP [68], and gold nanorods decorated with Fe_3O_4 NPs [69, 70] have been developed. Tunable plasmonic properties were achieved by controlling the thickness of the gold nanoshell or the size of gold nanoparticles [66, 68, 71]. One of the fascinating aspects of plasmonic MNPs is that the plasmonic property can be further tuned by varying the inter-particle distance via

external magnetic field [71]. Because the sensitivity of SERS strongly depends on the distance of gold or silver nanoparticles, and single molecule detection can be achieved in the very narrow gap between nanoparticles [72, 73], it is expected that closely packed plasmonic MNPs could serve as highly sensitive SERS-active substrates for sensing and detection applications. While plasmonic MNPs have been explored for protein concentration/detection using SERS [74], pathogen separation and imaging [69], photothermic therapy [67, 70], drug delivery [55, 75], and immunoassay [76, 77], little work has been reported to apply plasmonic MNPs for simultaneous concentration and detection of microorganisms using SERS.

Using plasmonic NPs (e.g., Au or Ag NPs) for the detection and differentiation of intact microorganisms such as bacteria or spores by SERS has been extensively studied recently [78-80]. However, the non-uniform attachment of plasmonic NPs on bacteria makes it difficult to conduct quantitative analysis and reproducible detection. Early studies made SERS samples by simply mixing a bacteria solution with colloid plasmonic NPs. The mixture was either dried on a glass slide and then measured by Raman spectrometer [81], or directly detected in a cuvette [82]. Although these methods are straightforward and easy to conduct, it was found that NPs non-uniformly attached to bacteria, and NPs and bacteria are non-uniformly distributed on the substrate surface, resulting in low reproducibility and accuracy. Several new approaches were developed for solving this problem. One method was based on “convective assembly” of NPs and bacterial cells by slowly moving a glass slide with an angle to another glass slide having

a drop of bacteria and NPs mixture. The relatively uniform distribution of bacteria and NPs on the substrate was obtained and signal reproducibility was notably improved [83]. To further improve the distribution of NPs on the surface, clusters of NPs were assembled in prefabricated nanohole arrays via electron beam lithography (EBL) for SERS detection of bacteria [84]. Both of these methods could improve detection reliability and reproducibility to some extent. However, these methods always require a relative high concentration of bacteria solution to achieve the detectable SERS signals.

In practical applications of pathogen detection and identification, potential samples from fields or patients are always in low concentration. Culturing and growing these bacteria require prolonged time and strictly controlled environments, therefore, methods that can concentrate bacteria samples to improve detection accuracy are highly desired [43]. Several bacteria concentration methods have been developed by using, for example, magnetic beads [85], electrodynamic [86], and microfluidic systems [43]. However, to fulfill the criteria by World Health Organization for concentration of bacterial samples (i.e., simple-to-use, rapid, low-cost, sensitive, accurate, specific, and robust [87, 88]), new methods have to be developed.

In this work, we developed multifunctional magnetic-plasmonic Fe_3O_4-Au core-shell NPs and demonstrated that they can be used for simultaneous fast concentration of bacterial cells by applying an external point magnetic field, and sensitive detection and identification of bacteria using SERS. This novel platform significantly simplifies the concentration and detection process, which holds great promise for

applications in food safety, environmental monitoring, medical diagnoses, and chemical and biological threat detections.

4.2 Experimental

4.2.1 Preparation of Fe_3O_4-Au NPs:

Superparamagnetic Fe_3O_4 NPs (MNPs) were prepared according to the reported method [30]. Briefly, a solution containing both ferric chloride and ferrous chloride was added dropwise to a 1.5 M NaOH solution under vigorous mechanical stirring and nitrogen gas protection at room temperature. The reaction temperature was gradually increased to 75°C and held for 1 h under stirring and nitrogen gas protection. The products were collected with a permanent magnet, re-dispersed in de-ionized (DI) water (18.2 MΩ cm), and then collected by the permanent magnet again to wash away the non-magnet impurities. This process was repeated five times.

The MNPs were then coated with citrate by mixing 1 mg MNPs with 1mL, 0.5 mg/mL citric acid solution at 50°C for one hour. The products (C-MNPs) were washed three times with DI water [89]. After that, the C-MNPs were coated with PEI by mixing 1 mg C-MNPs with 1 mg/mL PEI water solution for 30 min at room temperature, followed by washing three times with DI water to obtain the product (PEI-MNPs).

To make gold coated magnetic NPs, 0.1 mg PEI-MNPs were dispersed in 5 mL DI water, to which 50 μL of 1% $HAuCl_4$ solution and 10 μL of 1% NaOH solution were added. The growth of Au on the PEI-MNPs was started by adding 25 μL 0.2 M NH_2OH solution and the reaction was conducted under sonication at room temperature for 30 min

[90]. The products (Au-MNPs) were collected by a permanent magnet, and re-dispersed in 5 mL DI water. In order to grow a fully covered gold nanoshell, the reaction was repeated 4 more times. Before the Raman tests, the Au-MNPs were dried and cleaned in an oxygen plasma cleaner for 10 min. The cleaned Au-MNPs were re-dispersed in DI water to form a 30 μg/mL colloid solution.

4.2.2 SERS tests of 4-mercaptopyridine (4-MP)

All the samples in this study were prepared on silicon chips, which were thoroughly rinsed with DI water and acetone, dried under a stream of nitrogen gas, and cleaned in a UV/ozone cleaner for 20 min before use. A 10 μl drop of 3 μg/mL Au-MNPs solution was made on a silicon chip. In order to condense the Au-MNPs to a dot on the chip, one corner of a permanent magnet was put underneath the chip. After about 5 min, a dot of Au-MNPs was formed, and the liquid was completely evaporated after about another 5 min. Four chips prepared by this method were immersed in four different aqueous solutions with the 4-MP concentration of 100 nM (~10 ppb), 10 nM (~1 ppb), 1 nM (0.1ppb) and 0 nM, respectively, and incubated for 3 hours.[61, 91] The chips were rinsed with DI water and dried under a stream of nitrogen gas. SERS spectra of 4-MP were collected using a Renishaw InVia Raman spectrometer attached to a Leica DMLM upright microscope with a 50×/N.A. 0.8 objective. The excitation laser was 785 nm and the laser power at the sample was 0.5 mW. Each spectrum was collected with 10 s exposure time and 3 accumulations.

4.2.3 SERS tests of bacteria

Three Gram-negative bacterial strains, *Acinetobacter calcoaceticus (A. calcoaceticus), Escherichia coli K12 (E. coli K12), and Pseudomonas aeruginosa (P. aeruginosa)*, were purchased from American Type Culture Collection (ATCC, USA). *E. coli K12* (ATCC 10798) *and P. aeruginosa* (ATCC 10145) are wild types grown in Lysogeny broth for 10 h at 37°C and *A. calcoaceticus* (ATCC 23055) grown at 30°C. After sub-culturing from single colonies three times, the biomass was collected carefully and washed with DI water three times. The final biomass concentration was diluted to 2×10^5 cfu/mL with DI water.

To make the SERS test sample, 9 μL bacteria solution (2×10^5 cfu/mL) was mixed with 1 μL Au-MNPs (30 μg/mL) solution, then the mixture was dropped onto a clean silicon chip. The Au-MNPs along with the bacteria were condensed into a small dot by placing one corner of a permanent magnet underneath the chip. SERS spectra were collected using the same Renishaw Raman system and the 50×/N.A. 0.8 objective. The excitation laser was 785 nm and the laser power was 0.25 mW at the sample. Each spectrum was collected with 10 s exposure time and single accumulation. To increase the statistics, 15 spectra were collected for each sample at different places within the dot area.

4.3. Results and discussion

4.3.1 Synthesis and characterization of Fe_3O_4-Au NPs

The Fe_3O_4 NPs (MNPs), synthesized using the traditional co-precipitation method [30], are composed with a number of superparamagnetic Fe_3O_4 nano-crystals (~ 15 nm)

and possess a final hydrodynamic size of ~70 nm determined by dynamic light scattering (DLS). The Zeta potential measurement showed that these MNPs are positively charged. In order to grow a gold shell around a MNP core, the MNP surface has to be modified with molecules having functional groups that can attract gold ions or small gold nano-seeds, facilitating the growth of gold nanoshells by reducing chloroauric acid with reducing reagents [92-94]. Positively charged polyethyleneimine (PEI) was selected as the surface modification agent [90] and attached to the surfaces of MNPs pretreated with negatively charged citrate via electrostatic interaction. Due to the long chain of PEI, the MNPs tended to aggregate during the reaction. Therefore, the reaction took place under sonication to maintain the separation of particles. In addition, it was found that the short, repeated cycle of reactions can efficiently prevent the formation of large irregular particles [74]. Our results show that the Au-MNPs produced by conducting the reaction for 5 cycles were not only fully covered by gold but also highly monodispersed. The transmission electron microscopy (TEM) (Figure 4-2a) and scanning electron microscopy (SEM) (Figure 4-2b) images show that the Au-MNPs possess a uniform size of ~ 200 nm. Each individual Au-MNPs has a star-shape gold nanoshell as shown in the high resolution TEM image in the inset of Figure 4-2a. The star-shape gold nanoshell could be due to the nucleation and growth of gold from the randomly distributed amine groups at the PEI polymer chains. The DLS measurement showed that the Au-MNPs have a hydrodynamic size of 248.6 (± 35.8) nm (Figure 4-2c). The plasmonic property of these Au-MNPs was confirmed by the UV-vis-NIR spectroscopy. Figure 4-2d shows a broad

absorption peak at ~ 730 nm caused by the gold shell. The broad NIR absorbance was also observed in the multifunctional plasmonic-magnetic nanoroses [67].

To evaluate the magnetic mobility of the Au-MNPs, a drop of 10 μL Au-MNP solution (3 μg/mL) was made onto a clean silicon chip surface and then condensed using a permanent magnet. As shown in Figure 4-3a, the drop spread quickly forming a thin liquid film. Placing a corner of a permanent magnet at the center of the liquid spot underneath the silicon chip, the Au-MNPs were attracted to form a small dot in about 5 min due to the strong point magnet field. After another 5 min, the liquid was completely evaporated, leaving a condensed Au-MNP dot on the silicon chip (Figure 4-3b). The morphology of the dot was further examined using SEM. Figure 4-3c shows Au-MNPs were condensed to a small dot about 500 μm and closely packed within the dot area shown in the higher magnification SEM image (Figure 4-3d).

This result shows that the Au-MNPs can take the advantage of the magnetic property of Fe_3O_4 MNP cores to be quickly condensed into a small dot by applying an external point magnetic field. Unlike nonuniformly distributed Au NPs on a surface formed by dropping a conventional Au NPs solution, the condensed dot provides a large area of closely packed Au-MNPs with very high density of "hot" spots that are expected to be able to greatly enhance Raman scattering [95]. Therefore, forming a closely packed Au-MNP dot by applying a corner of a permanent magnet can be used as a simple and convenient way to prepare large area SERS-active substrates.

4.3.2 SERS tests of low concentration 4-Mercaptopyridine

To evaluate the SERS sensitivity of the condensed dot formed by the Au-MNPs, we used 4-Mercaptopyridine (4-MP) molecule as a SERS-reporter, which has been used in our previous quasi-3D plasmonic nanostructure studies due to its large scattering cross section and capability to form a self-assembled monolayer (SAM) on gold surfaces, comparable to alkane thiols [61, 96, 97]. The silicon chips with the condensed Au-MNP dot prepared as described above were immersed into 4-MP solutions with different concentrations for 3 h. The chips were rinsed with DI water to remove any physically adsorbed molecules, and then dried under a nitrogen stream.

Figure 4-4 shows the SERS spectra taken from the condensed dots that have been immersed in different concentrations of 4-MP solutions. The peaks at 1000, 1061, and 1096 cm^{-1} correspond to $1a_1$ ring breathing, $18b_2$ β(CH) and $12a_1$ ring breathing/C-S vibration, respectively, which belong to the characteristic peaks of 4-MP molecule [98]. As the concentration of 4-MP solution was decreased from 100 nM (~10 ppb) to 1 nM (~0.1 ppb), the intensities of the characteristic peaks decreased. Even though the solution concentration was dropped to 1 nM (~0.1 ppb), the intensities of the peaks at 1000 and 1096 cm^{-1} are still about 10 times higher than the baseline noise, which indicates that the limit of detection should be even lower than 1 nM (~ 0.1 ppb). This extreme high SERS sensitivity of the condensed Au-MNP dot is attributed to the high density of SERS-active "hot" spots formed by both closely packed Au-MNPs and the star-shape Au-MNPs [95]. We also took SERS spectra at different areas of the dot. The results showed very good reproducibility from spot to spot. The extreme sensitivity and high reproducibility make

the condensed Au-MNP dots well suited as SERS-active substrates.

4.3.3 Concentration of bacteria

The concept of concentrating bacterial cells using Au-MNPs in the existence of an external point magnetic field is depicted in Figure 4-1. A thin liquid film with Au-MNPs and bacterial cells are spread on the surface after dropping the solution on the silicon surface. The Au-MNPs are pulled toward the center and gradually condensed to form a dot by the point magnetic field induced by the corner of the permanent magnet. In the meantime, bacterial cells are pushed by the moving Au-MNPs and concentrated in the dot area.

Three Gram-negative bacterial strains, *Escherichia coli K12* (*E. coli K12*, ATCC 10798), *Pseudomonas aeruginosa* (*P. aeruginosa* , ATCC 10145), and *Acinetobacter calcoaceticus* (*A. calcoaceticus*, ATCC 23055), were used in this study. In order to demonstrate the capability of Au-MNPs to be able to efficiently concentrate bacteria to the dot area by the point magnetic field, a drop of the mixture of 1 μL Au-MNP solution (30 μg/mL) and 9 μL *E. coli K12* solution (2 x 10^5 cfu/mL) was placed on a clean silicon chip surface. A condensed Au-MNP dot was formed by applying a point magnetic field as shown in Figure 4-5a. Bacterial cells concentrated in the dot area can be clearly seen in the higher magnification SEM images in dark contrast (Figure 4-5b and c), while only few bacterial cells were found in the area outside the dot (Figure 4-5d).

The concentration efficiency was evaluated by comparing the number density of bacterial cells on the surface with and without concentration. The number of bacterial

cells was counted in the SEM image taken with the magnification of 1000x, equivalent to 0.0144 mm^2 per frame. The average number of bacterial cells in the same area without concentration was estimated to be 1.3 per frame, calculated from the total number of bacterial cells in 9 μL 2 x 10^5 cfu/mL divided by the average spread spot size of about 20 mm^2. The average number of bacterial cells within and outside the dot area as well as without concentration for three bacterial strains tested is plotted in Figure 4-6. It shows that the average number of bacterial cells within the dot area is about 60 times higher than that without using magnetic concentration, and about 120 times higher than that outside the dot area. Clearly, the Au-MNPs act as nano-workers, pushing the bacterial cells from a large spread liquid film to a small condensed dot on the chip surface, which provides a convenient yet efficient means to concentrate bacterial cells. Interestingly, we observed from the SEM images that for most bacterial cells in the dot area, Au-MNPs are closely packed alongside the bacterial cells but not on the top of the cells. Since the diameter of bacteria is ~0.5 μm and the average diameter of Au-MNPs is ~200 nm, we estimated that the Au-MNPs were packed in about 3 layers. The Au-MNPs were oxygen plasma cleaned prior to mixing with bacteria. Therefore, they have no specific affinity to the bacteria. In the course of condensation, the Au-MNPs are subjected both lateral and vertical forces due to the point magnetic field. While the lateral force pushes the Au-MNPs towards the point where the corner of the magnet is, the vertical downward force also drags the Au-MNPS towards the chip surface. This might be the reason that there are almost no Au-MNPS on top of bacterial cells.

4.3.4 Detection and differentiation of bacterial strains by SERS

SERS spectra of bacteria were taken in the dot area immediately after the concentration. In order to further differentiate three bacterial strains, at least 15 SERS spectra were taken for each strain of bacteria at different places in the dot area. The 785 nm laser was focused onto the surface, forming a 25 μm x 2 μm rectangular spot which covers about 4-6 bacterial cells per laser spot. Due to the strong enhancement from the closely packed Au-MNPs directly attached to the cell wall of the bacteria, the SERS spectra are very strong, giving only 4-6 bacterial cells being detected. Even though gold can quench the fluorescence signal from bacterial cells, the original SERS spectra still show quite strong fluorescence background (Figure 4-7). After baseline correction using the cubic spline interpolation method, the peaks were well resolved. The position and intensity difference of the vibrational peaks can be obviously seen among the SERS spectra of three bacterial strains (Figure 4-7). Because the local electric field of gold nanoparticles decays exponentially with distance, the SERS spectra of microorganisms contain mainly the molecular information of cell walls. Therefore, these differences could be attributed to the different biochemical components on the cell walls of different bacteria. All the three bacterial strains tested in this study are Gram-negative bacteria. The cell walls of these bacteria have an outer membrane rich of lipopolysaccharides (LPSs). LPSs are large molecules consisting of a lipid and a polysaccharide joined by a covalent bond, which act as endotoxins and elicit strong immune responses in animals. Peaks at 787, 866 and 1440 cm^{-1} are the characteristic peaks seen in lipids and

polysaccharides, respectively [99]. Table 4-1 lists the position and putative assignments of 15 major peaks in the spectrum of each bacterial strain. Clearly, these peaks indicate the existence of proteins, carbohydrates, fatty acid, and lipids. All are the biochemical components in the Gram-negative cell wall.

The principle component analysis (PCA) method was applied to further differentiate the bacterial strains based on the SERS spectra. The PCA method projects a data set into a transformed space that maximizes the variability within the data and thus allows spectral similarities and differences to be more easily observed. Both the wave number and intensity of each peak were used in PCA. The first two principle components (PCs) among the total 15 PCs, which account for greater than 90% of the variance in the analysis, were used to characterize these spectra. If the spectra of the same bacterial strain have definite, repeatable similarities, data points from each species should cluster together within the transformed space, indicating successful differentiation of a species-specific SERS signature. Assuming that, for a given species, the first two PCs follow a Gaussian distribution, an elliptical boundary in PC space is developed based upon Prieb's Adaptive Mixture Model [97]. Figure 4-8 shows a two-dimensional (2D) PCA plot of the first two PCs for the three bacterial strains. It can be seen that in the new PC transformed space, the elliptical boundaries of each bacterial strain are disjointed, and the three bacteria can be clearly distinguished.

The successful detection and differentiation of bacterial strains indicate that besides acting as nano-workers to concentrate bacterial cells by moving them under the external

magnetic field, the closely packed Au-MNPs can also function as SERS substrates for sensitive detecting and accurately distinguishing bacterial strains based on SERS spectra that carry the biomolecular characteristics of the bacterial cell walls.

4.4. Conclusions

In this work, we demonstrated a magnetic-plasmonic Fe_3O_4-Au core-shell nanoparticle platform for fast and convenient concentration, sensitive detection, and accurate differentiation of bacteria. The multifunctional Au-MNPs possess a strong magnetic property due to the superparamagnetic Fe_3O_4 core, and can be condensed to a small dot by applying an external point magnetic field. The small dot exhibits a strong SERS effect because of the unique plasmonic property offered by the star-shape gold nanoshells and the high density of "hot" spots formed by the closely packed Au-MNPs. These closely packed Au-MNP dots can be used as a highly sensitive SERS substrate for detection of molecules with a limit of detection better than 0.1 ppb. Taking advantage of both magnetic and plasmonic properties, the Au-MNPs can effectively concentrate bacterial cells in the existence of an external point magnetic field to a level of ~ 60 times higher than the sample without concentration. In addition, the concentrated bacterial cells surrounded by closely packed Au-MNPs can be directly detected using SERS. The strong and reproducible SERS spectra of bacteria allow accurate differentiation of bacterial strains using the PCA method. Compared to the current existing SERS bacterial sample preparation methods, the multifunctional Au-MNP platform offers many advantages, such as quick, robust one-step concentration and detection, easy operation, and cost

effectiveness. Therefore, this platform holds a great potential for field applications in food safety, environmental monitoring, and chemical and biological threat detections.

TABLE 4-1. Putative assignment of major peaks in the SERS spectra of bacteria [99].

wavenumber [cm^{-1}]	chemical characterization
530	S-S disulfide stretching in proteins
666	C-S stretching mode of cystine (collagen type I)
740	C-S stretch
787	O-P-O stretching
866	Phosphate group
940	C-C stretch backbone
983	C-C stretching β-sheet (proteins)
1029	O-CH_3 stretching of methoxy groups
1162	Tyrosine
1239	Amide III
1333	CH_3CH_2 wagging, collagen (protein assignment)
1417	C=C stretching in quinoid ring
1440	CH_2 bending (lipids)
1564	COO^-
1618	ν(C=C), tryptophan (protein assignment)

Figures

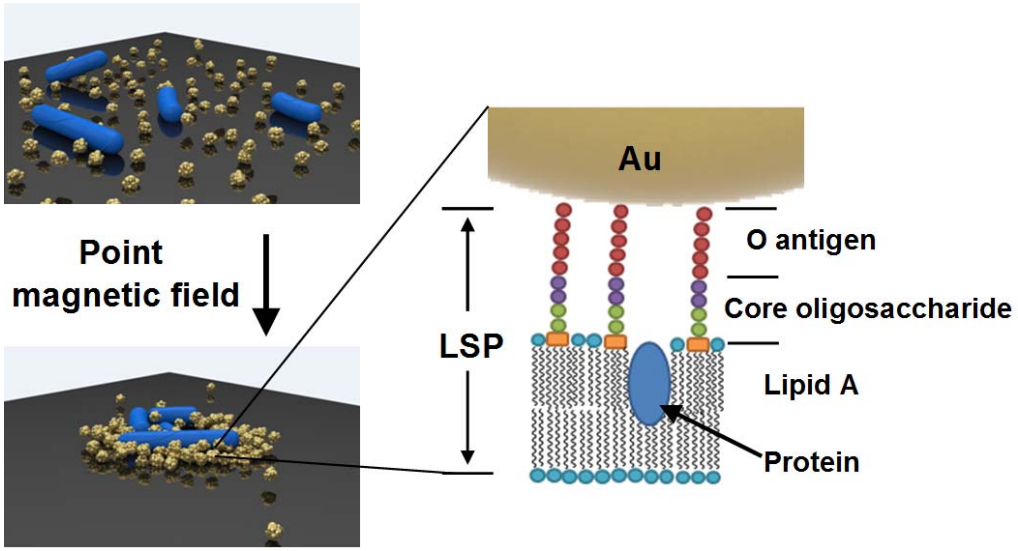

Figure 4-1. Schematics of the condensation process of Au-MNPs and bacteria (left) and the biomolecular characteristics of the bacterial cell wall that can possibly be detected by SERS (right).

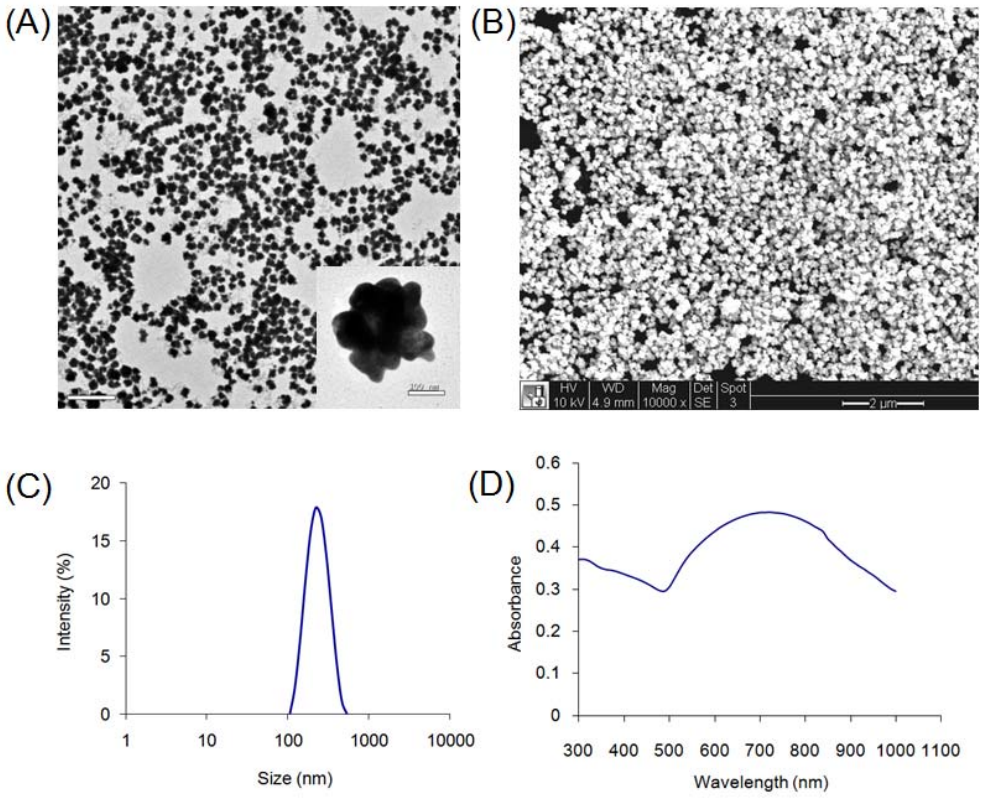

Figure 4-2. Characterization of the Au-MNPs. (A) A TEM image (scale bar = 1 μm). The inset is a high resolution TEM image showing the star-shape Au-MNPs (scale bar = 100 nm). (B) A SEM image (scale bar = 2 μm). (C) The hydrodynamic size measured by DLS. (D) A UV-vis-NIR absorption spectrum.

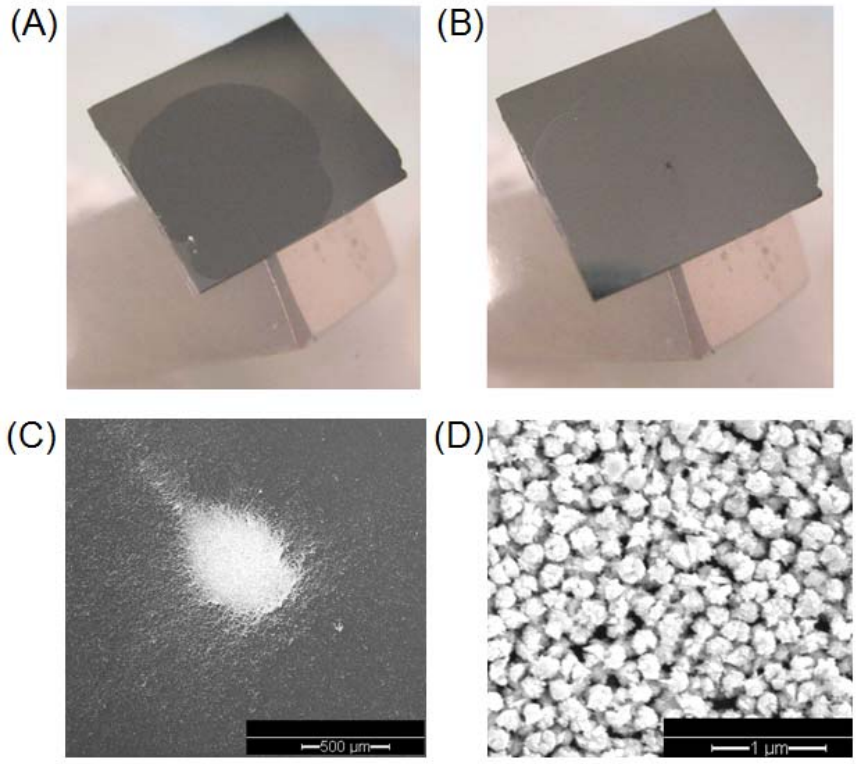

Figure 4-3. Magnetic concentration of Fe_3O_4-Au NPs. Photographs of a drop of the Fe_3O_4-Au NP solution on a silicon chip before (A) and after (B) the condensation. SEM images of the overview (C) and the center area (D) of the magnetically condensed dot.

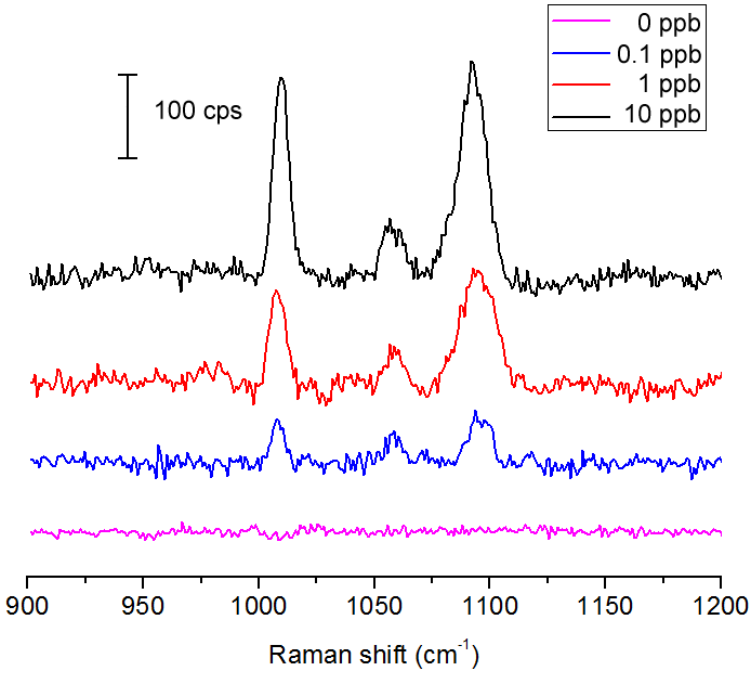

Figure 4-4. SERS spectra taken from the area of condensed Au-MNP dots on silicon chips, which have been immersed in different concentration of 4-MP solutions, washed with DI water and dried with a stream of N_2.

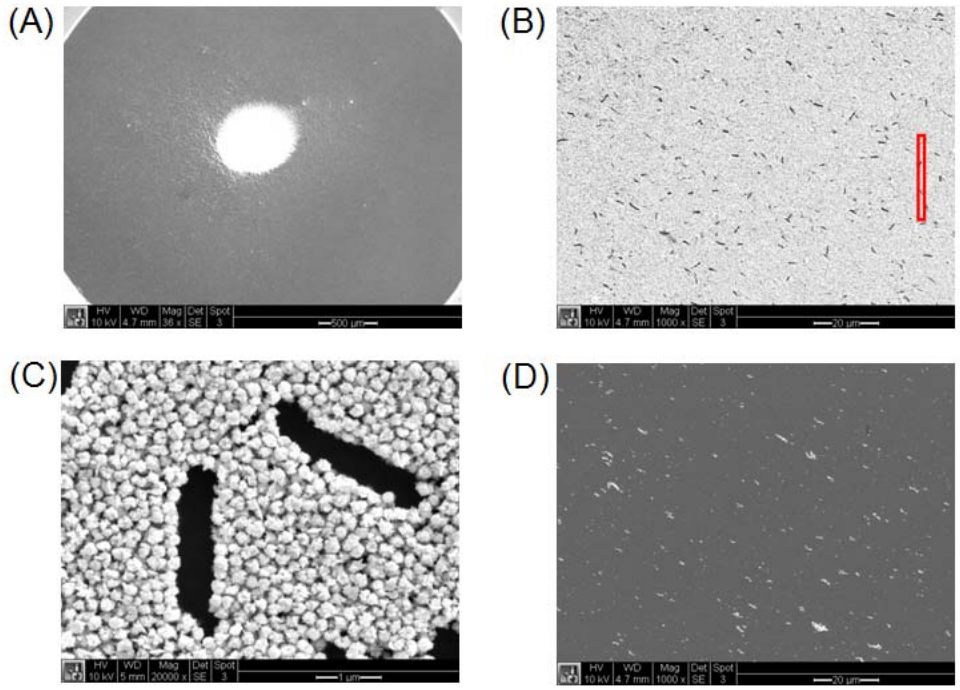

Figure 4-5. (A) A SEM image of the overview of the dot area (scale bar = 500 μm). (B) and (C) SEM images of condensed Au-MNPs and concentrated bacterial cells within the dot area. Bacteria are shown in dark contrast. The scale bars are 20 and 1 μm, respectively. (D) A SEM image of Au-MNPs and bacteria of the area outside the dot on the chip. The scale bar is 20 μm. The red rectangle in (B) shows the approximate size of the laser spot (25 μm x 2 μm).

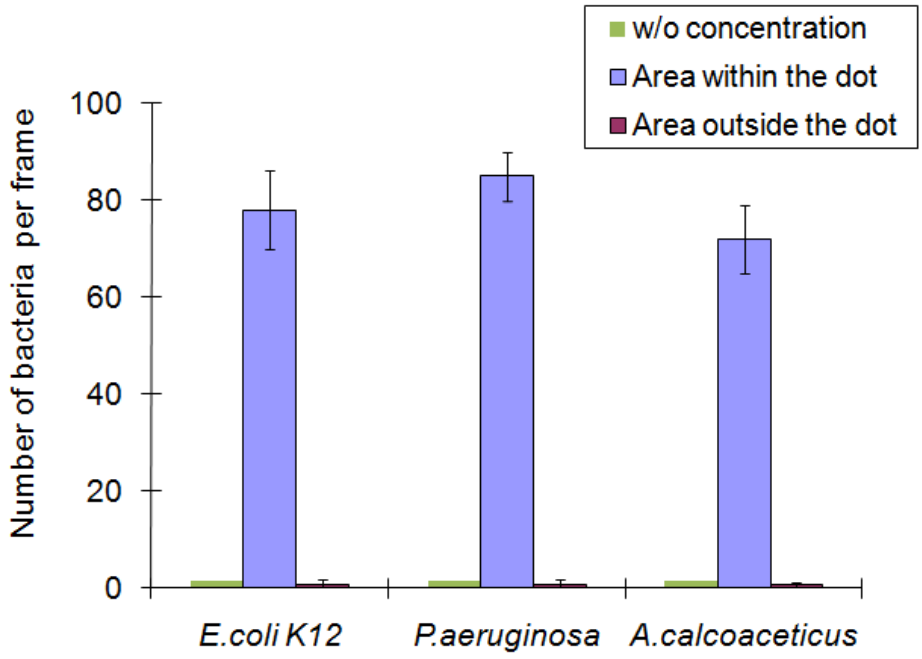

Figure 4-6. Comparison of the number density of bacteria within and outside the dot area as well as without concentration. The SEM image was taken at 1000x magnification, equivalent to the size of 0.0144 mm^2. Number of bacteria in the SEM images within and outside the dot area was counted for each strain. The average number of bacteria in the area of 0.0144 mm^2 without magnetic concentration was calculated and used as control.

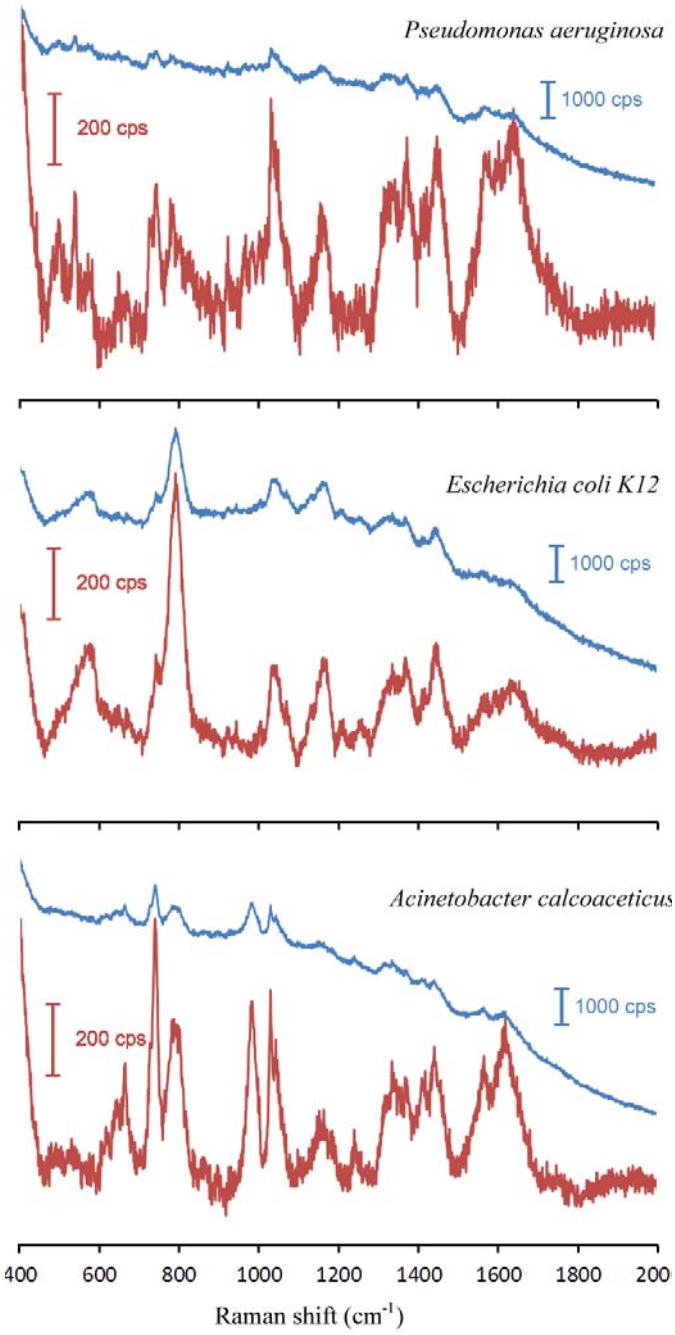

Figure 4-7. Representative Raman spectra of three different bacterial strains, *A. calcoaceticus, E. coli K12 and P. aeruginosa*. Blue lines are the original spectra and red lines are the baseline-corrected spectra.

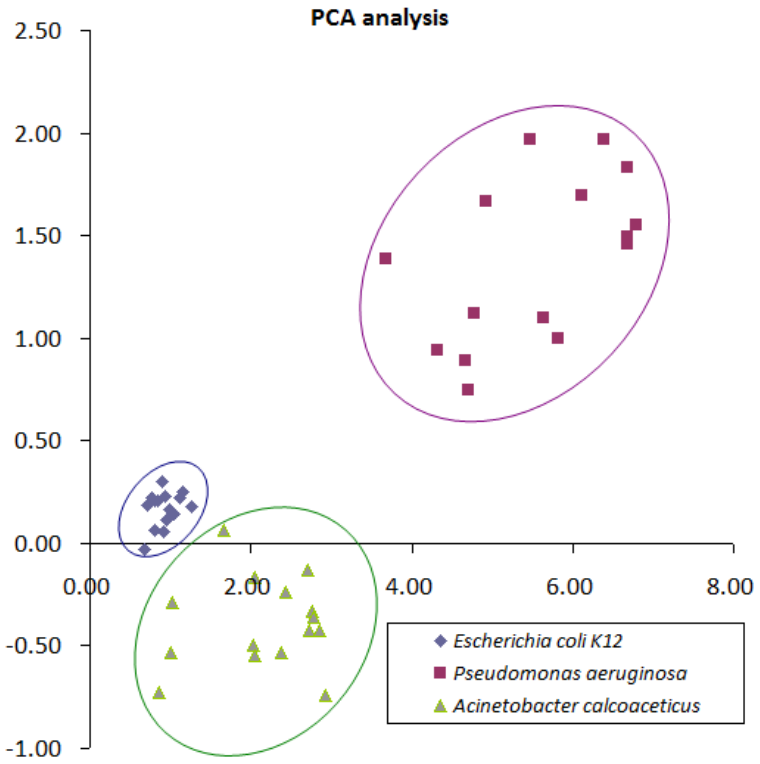

Figure 4-8. The 2D-PCA plot showing the differentiation of three different bacteria, *A. calcoaceticus, E. coli K12, and P. aeruginosa*.

Chapter 5 Hydrolytic Cationic Ester Microparticles for Highly Efficient DNA Vaccine Delivery

While DNA vaccination holds great potential to be a safer and more efficient alternative to traditional vaccination strategies, the current lack of nontoxic and effective delivery systems is one of the greatest impediments to its clinical implementation. In this work, we used a convenient one-step method to prepare a degradable "microgel" delivery platform that features hydrolytic esters. Prior to hydrolysis, these micron-sized gel particles can effectively condense DNA due to their positive surface charge. Upon entering antigen-presenting cells (APCs), the microgels are hydrolyzed to non-toxic zwitterionic polymers, consequently releasing the DNA and inducing phagosomal escape. Surface charge, DNA loading, cytotoxicity, and gene transfection efficiency of the hydrolysable microparticles with different tertiary to quaternary amine ratios were systematically studied. Nonhydrolysable counterparts and commercially developed PLGA-CTAB particles were used as the control. The passive targeting effect was further evaluated by blocking the phagocytosis pathway of the cells. The hydrolytic microgels prepared in this study possess great potential to become a platform for DNA vaccine delivery.

5.1. Introduction

Vaccines are among the greatest inventions in human history, as they have led to dramatically improved healthcare and greatly reduced mortality [100-104]. Traditional

vaccines are predominately based on killed or attenuated pathogens, protein antigens or modified toxins, and are limited to a small number of infectious diseases [105, 106] because they only generate a humoral (antibody-mediated) immune response. Activation of a cell-mediated response is necessary to generate cytotoxic T-lymphocyte cells and requires antigen presentation on infected cells via major histocompatibility class I (MHC I) complexes. This is currently only achievable with attenuated live organism vaccines, which are hindered by safety concerns and manufacturing difficulties [100, 107].

DNA-based vaccines are an attractive alternative to the formats currently in use, as they can initiate both humoral and cell-mediated immune responses [100, 106-109]. This would allow prophylactic vaccination against pathogens such as malaria and HIV as well as therapeutic vaccination to selectively kill cancerous cells. Instead of the non-replicating antigens used in traditional vaccines, a gene coding for an antigen-specific protein would be delivered. This more closely mimics live infection, and would lead to deployment of a complete immune response and immediate destruction of future pathogens that express this protein. In contrast with manufactured proteins, DNA can be produced simply, quickly and affordably, making this strategy promising for global health epidemics. [100, 101].

For gene-based vaccines to become clinically viable, a high level of gene transfer (transfection) must reliably occur. “Naked” DNA cannot effectively navigate many extracellular and intracellular barriers prerequisite to its expression; it is for this reason that many classes of delivery vectors are in development. While viral platforms are the

most effective, they are fraught with safety and immunogenicity concerns, so several nonviral delivery systems based on polymers or lipids are in development, Cationic lipids and liposomes have shown good transfection efficiency, but are limited by stability. Therefore, significant effort has been dedicated to cationic polymers as an alternative; they are enormously customizable, so one multifunctional polymer can be tuned to optimize a vector's many duties. However, many nonviral vectors suffer from poor efficiency or high cytotoxicity [104].

Microparticles loaded with DNA have been proven to be a very effective nonviral method for passively targeting DNA vaccines to professional antigen presenting cells (pro-APCs) [110]. For the most effective complete immune response, pro-APCs must be directly transfected and present antigens via MHC. These cells are the only types that have both MHC classes (I and II), express co-stimulatory molecules such as CD80 and CD40 and can migrate to the lymphatic system [111]. Thus, they play a vital role in T-lymphocyte activation and an effective DNA vaccine delivery system should target them. Microparticles with diameters ranging from 1-10 μm are too large for endocytosis by normal cells, but small enough for phagocytosis by macrophage or dendritic cells [101]. These are the cell types that can initiate a coordinated immune response. DNA-encapsulating poly(lactic-co-glycolic acid) (PLGA) microparticles are commonly used for this purpose; however, this strategy presents several major problems. The encapsulation process can damage DNA, and it is inefficient. Additionally, the hydrolysis of PLGA can lower pH inside the particle to 1.5-3.5, catalyzing the hydrolysis

of encapsulated DNA [100, 112]. Gene "unpacking" from the microparticle is slow; generally, the time required for complete DNA release is much longer than the average life of a phagocytic cell after its activation and migration to draining lymph nodes [108]. All these above drawbacks result in lowered transfection efficiency [100, 112].

The use of cationic microparticles for adsorption of DNA onto their surfaces offers an alternative strategy that avoids plasmid damage during complex formation. Literature reports also show that this method can increase gene loading and make plasmids immediately available upon entering cells, significantly improving the transfection efficiency [100]. Positively charged cetyltrimethylammonium bromide (CTAB) and poly(ethyleneimine) (PEI) have been grafted to the surface of PLGA microparticles for this purpose; these methods have achieved notable utility in genetic vaccination both *in vitro* and *in vivo* [15, 113-115]. However, CTAB contains only quaternary amines and is unable to buffer DNA from an acidic phagosomal environment. PEI has strong gene transfection ability but is well known for its cytotoxicity [113]. Therefore, new cationic microparticles that can mediate efficient gene transfection with low toxicity are highly desired.

Our group has demonstrated the use of cationic carboxybetaine methacrylate ethyl ester polymers (PCBMA-EE) to condense DNA [11]. By hiding the anionic carboxylate group in the carboxybetaine moiety with an ester, the polymer can be made temporarily cationic (Figure 5-1A) [4, 12]. Meanwhile, by co-polymerizing with a tertiary amine analogue of CBMA-EE, endosomal buffering functionality can be incorporated into the

copolymer. Intracellular hydrolysis of the ester results in zwitterionic PCBMA (Figure 5-1A), which facilitates DNA unpackaging, and is non-toxic. It has been shown that by tuning the tertiary and quaternary monomer ratio in the copolymer, gene transfection efficiency can be optimized. None of the ester polymers showed obvious toxicity to the cells [11].

In this work, we develop microgels fashioned from the aforementioned PCBMA copolymer (incorporating tertiary and quaternary amine ester monomers) as a novel platform for DNA vaccination with high efficiency and low toxicity, as illustrated in Figure 5-1B.

5.2. Materials and methods

5.2.1 Synthesis of tertiary (3°) CBMA–ethyl ester analogue

The synthesis procedure was modified from our previous reports [11]. Briefly, aluminum oxide was added to Di-tert-butyl dicarbonate (BOC) and stirred at a low rate of speed. N-methyl aminoethanol was then added dropwise. The stir rate was increased as the mixture homogenized. The solution stirred at room temperature for 5 h. The aluminum oxide was separated from the intermediate product by sedimentation. The intermediate was then dissolved in anhydrous dichloromethane with TEA at 0 ^{o}C. The solution was stirred while methacryloyl chloride was added dropwise. The solution was allowed to warm to room temperature and react overnight. The reaction was again cooled to 0 ^{o}C, extracted twice with acid, base, and water. The organic phase was dried and concentrated *in vacuo* to yield a second intermediate product, which was then deprotected

with trifluoroacetic acid and purified on a silica-gel column. It was then dissolved in anhydrous acetonitrile at 0 ^{o}C. Potassium Carbonate and ethyl bromoacetate were then added. The reaction was kept at 0 ^{o}C and monitored by TLC until completion. The product was purified by pouring it into freezing water and extracted into ethyl acetate. Evaporation of the solvent yielded the tertiary amine CBMA ethyl ester analogue.

5.2.2. Synthesis of quaternary (4°) CBMA–ethyl ester

Ethyl bromoacetate was added to a solution of 2-(Dimethylamino) ethyl metharylate (DMAEMA) in acetonitrile, and stirred at 25 C for 18 h. The resulting residues were precipitated in ethyl ether, filtered, and subsequently washed twice by ethyl ether. The precipitate was dried under vacuum, yielding N,N-Dimethyl-N-(ethylcarbonylmethyl)-N-[2-(methacryloyloxy)ethyl] ammonium bromide (CBMA ethyl ester).

5.2.3 Preparation of microgels

The degradable microgels were prepared using a modified microemulsion method reported previously [45, 116]. Briefly, 0.1 g Span 80 and 2 mg V-70 were dissolved in 10 mL of hexane and kept in an ice bath. Tertiary ester, quaternary ester, and the disulfide crosslinker, L-cystine bisacrylamide, were dissolved in DI water and the final pH of the aqueous solutions was tuned to 5. Then, five different aqueous solutions were prepared by changing the molar ratios of the two esters; 100% tertiary ester and 100% quaternary ester were prepared, and copolymers with 25% steps (25%, 50% and 75% tertiary ester) were generated in addition. 0.35 mL of the aqueous solution was mixed with the organic

solution in a 100 mL flask with vigorous stirring, after which strong sonication was applied to form the microemulsion. The solution was kept in ice bath during this procedure. The flask was purged with nitrogen at 4 ^{o}C for 30 min to remove dissolved oxygen. During polymerization, the reaction was kept at 40 ^{o}C with stirring and was protected under nitrogen for 12 h. After the reaction, the product was washed with tetrahydrofuran three times to remove the surfactants, and then the product was washed three times with DI water.

Nonhydrolysable microgels were used as the control, synthesized using the same method as described above. Nonhydrolysable monomers 2-(Dimethylamino) ethyl methacrylate, which contains a tertiary amine, and (trimethylamino) ethyl methacrylate (TMAEMA) which contains a quaternary amine, were used. The tertiary ratios were also tuned from 100% to 0%, to make a parallel comparison with the hydrolysable microgels.

5.2.4 Preparation of PLGA-CTAB microparticles

Cationic microparticles were prepared by using a modified solvent evaporation process as reported previously [15]. Briefly, the microparticles were prepared by emulsifying 10 mL of a 5% (wt/vol) polymer solution in methylene chloride with 1 mL of PBS and vigorous stirring. The primary emulsion then was added to 50 mL of distilled water containing CTAB (0.5% wt/vol). The mixture was vigorously stirred for 12 h at room temperature, allowing the methylene chloride to evaporate. The resulting microparticles were washed twice in distilled water by centrifugation at 10,000g and freeze-dried.

5.2.5 Characterization and pDNA loading of microparticles

The hydrodynamic size and zeta potential of all microparticles were tested using a dynamic light scattering (DLS) particle sizer (Nano ZS, Zetasizer Nano, Malvern).

Plasmid DNA coding for firefly luciferase (gWiz-Luc) was used as the model DNA vaccine, and loaded on the microparticles as described by Singh et al.[15]. Briefly, pDNA loading was attempted at 1% w/w by incubating pDNA with the microparticle pH 5 solution at 4 ^{o}C for 6h [113]. This pH was chosen to ensure most of the tertiary amine groups were temporarily protonated, to increase microparticle charge and lead to complete DNA association. The resulting particles were centrifuged for 15min and washed 2 times with PBS. The supernatant was collected and analyzed by a spectrophotometer at absorbance of 260nm for pDNA content. pDNA loading on the cationic microparticles was calculated by subtracting the pDNA content in the supernatant from the initial concentration of pDNA added.

5.2.6 Gene transfection

RAW264.7 cells from American Type Culture Collection were cultured in DMEM (Gibco, Invitroven, Carlsbad, CA) with 10% FBS and 1x penicillin-streptomycin at 37 ^{o}C and 5% CO_2. One day prior to transfection, the cells were transferred to 24-well tissue culture plates, at 50,000 cells per well. All cells used in these studies were from passages 5-10.

On the day of transfection, fresh culture medium with different microparticle formulations were added to the wells at a pDNA dose of 1μg DNA per well. Cells were

incubated with these formulations for 4 h at 37^{o}C, after which the medium was replaced with fresh medium. The cells were cultured for another 48 hours and then washed with sterile PBS and lysed using the GloLysis Buffer (Promega). Total protein content in the cell lysate was determined using a Micro BCA protein assay kit (Pierce Biotechnology, Rockford, IL). The luciferase content obtained from the luminescence readings was normalized to the total protein content [11, 112, 113]. All samples were tested in triplicate.

5.2.7 Passive targeting

To confirm the macrophage cells internalized the microparticles via the phagocytosis pathway instead of the endocytosis pathway, tests were performed blocking the phagocytosis pathway before gene transfection. This was accomplished by adding 10 μM cytochalasin-D to each well to completely inhibit transfection via the phagocytosis pathway, after which transfection was conducted using same procedure as described above [112].

5.3. Results and discussion

In this work, all the particles were prepared with a one-step microemulsion polymerization method. The micron-sized hydrogel particles were prepared for pDNA loading and passive targeting by crosslinking tertiary and/or quaternary amine monomers with a degradable crosslinker. Microparticle samples prepared in this work possess a hydrodynamic size around one micron, as characterized by DLS and shown in Figure 5-2. Particles of this size have crucial advantages for genetic vaccine delivery. APCs such as

macrophage cells take in particles via phagocytosis, unlike most non-APCs. The choice of micron-sized instead of nano-sized vectors mediates passive targeting to these desired cells.

Due to their different formulations, the microparticles in this study carry very different surface charges. As expected, for both hydrolysable and non-hydrolysable microgels, the surface charge increases as the ratio of quaternary amines increases at neutral pH, as shown in Figure 5-3. When the microgels enter an acidic environment representing the phagosome (pH=5), their tertiary amine groups partially protonate and carry a positive charge, causing an increase of the particles' zeta potential. As shown in Figure 5-4, higher pDNA loading was achieved at higher quaternary ratios, due to more favorable charge interaction between the negatively charged pDNA and the positively charged microgels. However, particles with 0%, 25% and 50% tertiary ratios did not show significant loading differences, indicating that almost all DNA was likely adsorbed to these microgels. The PLGA-CTAB microparticles also possess positive surface charge, which did not change with the pH, because CTAB only contains quaternary amines [15, 117]. When pDNA was loaded onto the microgels' surface, the size of the complex increased and zeta potential decreased, as would be expected (Figures 5-2 and 5-3).

The macrophage cell line 264.7 has been widely used *in vitro* to evaluate the ability of microparticle formations to transfect APCs. In this work, plasmid DNA containing the luciferase gene was used as a model DNA vaccine to transfect the macrophage cells. Results are shown in Figure 5-5. For the hydrolytic microparticle formulations, changing

the quaternary to tertiary ratio produced significant shifts in transfection efficiency. Optimal transfection efficiency was achieved at a 1:1 quaternary to tertiary ratio. The luciferase expression for this formulation was twelve times higher than the PLGA-CTAB controls. The other hydrolytic formulations showed much lower rates of expression; this is likely due to the transfection efficiency being determined by two key parameters: the microparticle surface charge (determined by quaternary percentage) and protonation capacity (determined by tertiary percentage). Both of these functions are essential to efficient delivery. The results suggest that while a completely quaternary microparticle may load more pDNA, this benefit is negated by its inability to release its payload from the acidic phagosomal environment. The tertiary amines in the microgel structure may also assist in phagosomal escape through the "proton sponge" hypothesis [112, 113]. However, a completely tertiary microparticle does not possess enough positive charge to adsorb DNA, the additional positive charge groups of quaternary amines are required to achieve sufficient DNA loading.

Very low transfection was achieved by all the nonhydrolysable microparticle formulations. One potential reason is they are unable to release the adsorbed pDNA after entering the cells. This verifies the important role of esters in this nucleic acid delivery platform; when the ester hydrolyzes, the switch in polymer charge from cationic to zwitterionic reduces pDNA binding favorability and thus promotes pDNA release.

Cytotoxicity is another major challenge in gene delivery. While cationic polymers are required to condense pDNA, they can also be very toxic to cells. Thus, increased

transfection efficiency is only beneficial if minimal cytotoxicity is maintained. Clinical use of gene-based vaccines will require the platform to be nontoxic. The very low toxicity of hydrolytic microgels in this study can be attributed to the "switchable" nature of PCBMA charge. While the PCBMA-ester is initially cationic to condense pDNA like other platforms, its shift in charge to zwitterionic upon hydrolysis renders it non-toxic. Very similar counterparts that do not show this "switchable" behavior exhibit high toxicity, as seen in Figure 5-6.

The efficiency of passive targeting to these cells was evaluated by testing the effect of blocking the phagocytosis pathway during gene transfection. At a concentration of 10 μM of cytochalasin-D, phagocytosis can be blocked, while the endocytosis pathway common to many cell types remains effective [112]. As shown in Figure 5-7, for all the formulations, transfection efficiency was significantly inhibited when phagocytosis was blocked. This result confirms the transfection was achieved predominately by the phagocytosis pathway. The size of the microparticles is likely too large for clathrin or caveolae-mediated endocytosis [111, 118]. Therefore, the passive targeting effect can be achieved by preferentially transfecting the APCs using these microgels.

Finally, degradability is also highly desirable in synthetic vector platforms to avoid any potential adverse effects. Unlike other nondegradable microparticle platforms, such as polystyrene microparticles that will stay in the body for an undesirable prolonged period after they finish their job, the microgels presented in this work contain degradable crosslinkers, and can be degraded to small products and can be excreted from the body

via renal clearance [49, 116, 119].

5.4 Conclusions

In this work, a microparticle platform utilizing “microgels”, based on hydrolytic esters, was developed as a novel DNA vaccine delivery vector. These microgels were formed in a one-step polymerization method. By optimizing the tertiary to quaternary amine ratio in the microgels, this vector combines several important features for the successful gene transfection of APCs. First, passive targeting to APCs can be achieved due to the size of the microgels. Inhibition of phagocytosis using Cytochalasin D suppresses gene transfection, confirming this pathway. Second, prior to hydrolysis, the microgels carry a positive charge, requisite for high pDNA loading. Third, the tertiary moieties in the microgels can be protonated in the phagosomal environment, buffering pH changes to protect the nucleic acid payload and facilitating phagosomal escape. Results show that microgels with a 1:1 tertiary to quaternary amine ratio present the best gene transfection efficiency, about twelve times higher than the commercially developed PLGA-CTAB control. Fourth, after hydrolysis, the entire microgel becomes zwitterionic, promoting pDNA release and conferring low cytotoxicity. While the hydrolytic microgels were shown to be non-toxic, their non-hydrolysable counterparts presented high toxicity and poor transfection efficiency. Finally, the microgels are degradable in the intracellular reducing environment, and the degraded components are nontoxic and can be excreted from the body. In conclusion, the microgels developed in this work can be used as a promising platform for DNA vaccine delivery.

Figures

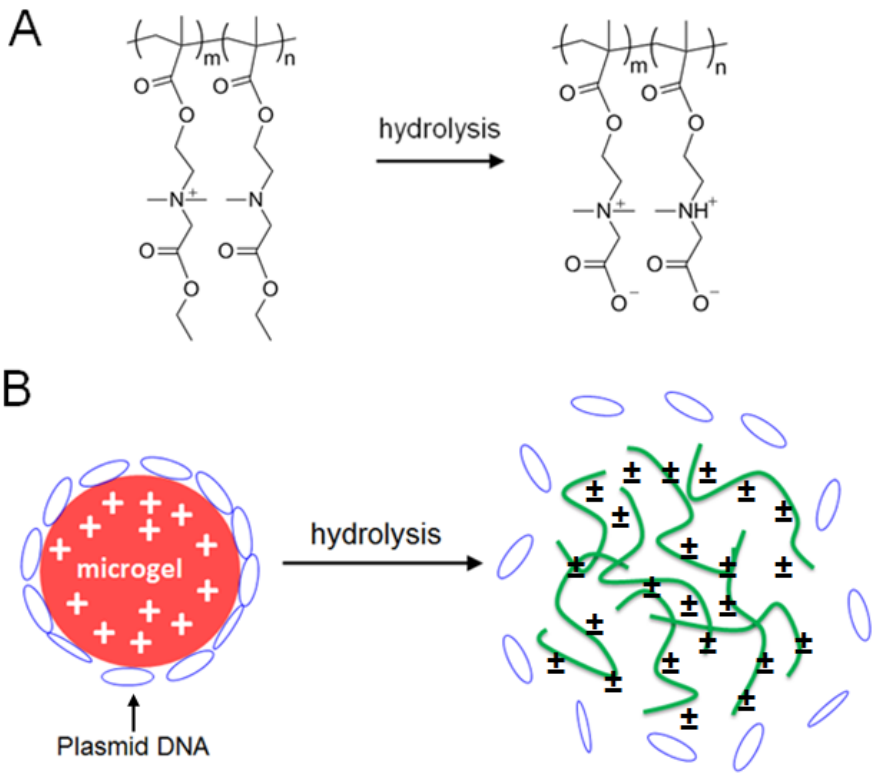

Figure 5-1. (A) Structure of the copolymer made from quaternary and tertiary ethyl esters before (left) and after (right) hydrolysis. Note that this polymer is cationic and zwitterionic before and after hydrolysis, respectively. (B) Scheme shows the pDNA adsorption and release before and after hydrolysis and degradation of the degradable microgel. The degraded products are presented in green.

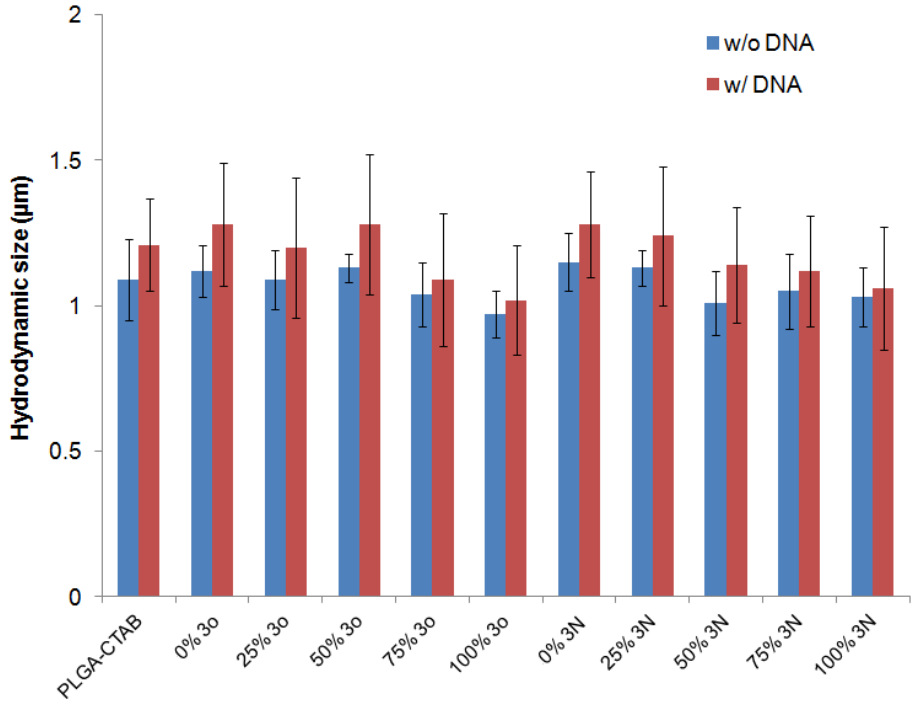

Figure 5-2. Hydrodynamic sizes of different microparticle formulations with or without pDNA loading. The microgels were prepared by crosslinking tertiary and quaternary monomers with different ratios using a degradable crosslinker. Microgels with 0% tertiary ester and 100% quaternary ester is denoted as "0% 3o"; similarly, its nonhydrolysable counterpart is denoted as "0% 3N". PLGA-CTAB particles were prepared by coating CTAB onto the PLGA microparticles.

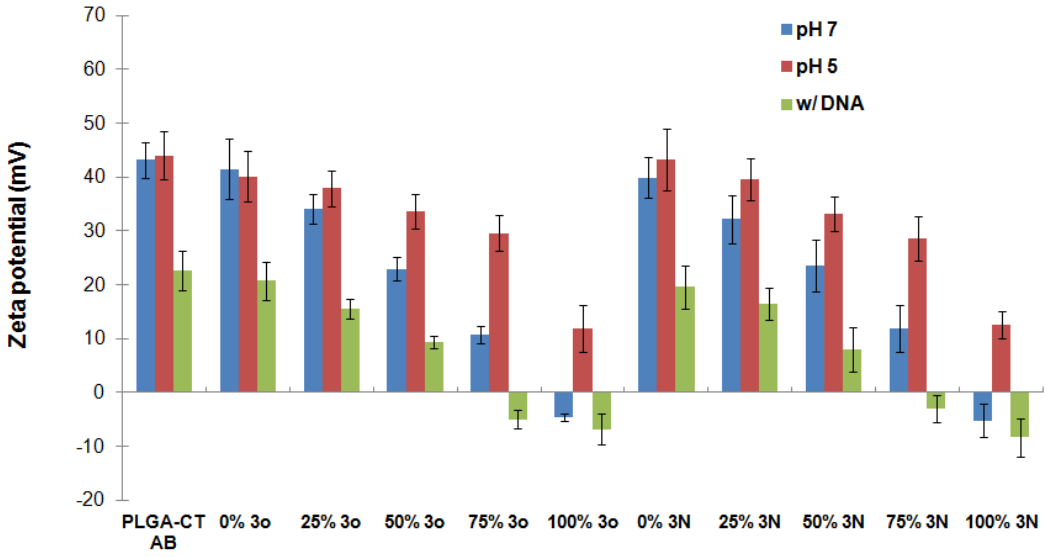

Figure 5-3. Zeta potential tests of different microparticle formulations at pH=5, pH=7 and once loaded with pDNA. When the microgels containing tertiary anime groups entered the pH=5 solution, protonation of the tertiary anime groups caused an increase of microgels' zeta potential.

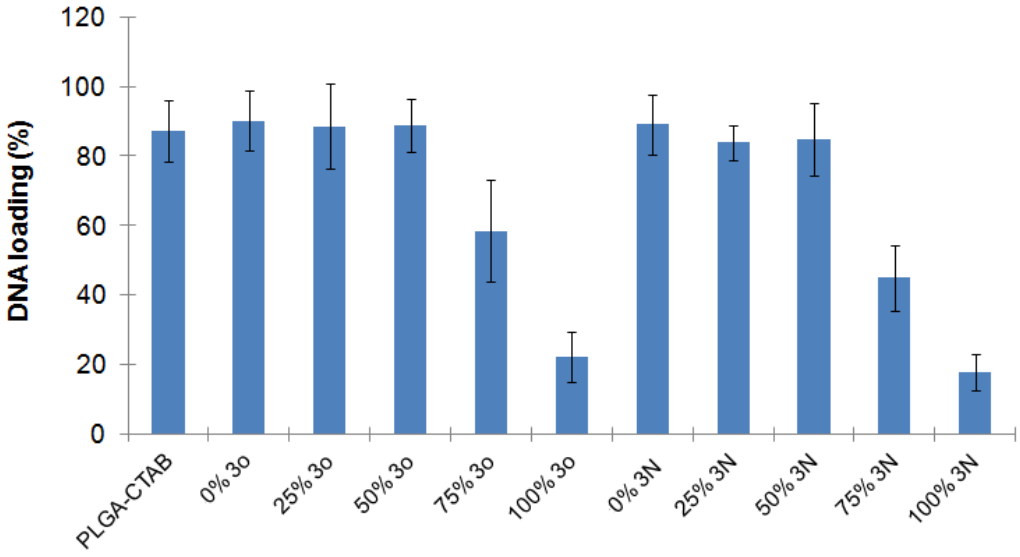

Figure 5-4. pDNA loading of different microparticle formulations. Increase of the quaternary ratio from 0% to 50% can increase the loading, but no further increase can be achieved probably due to the particle surface reaching saturation.

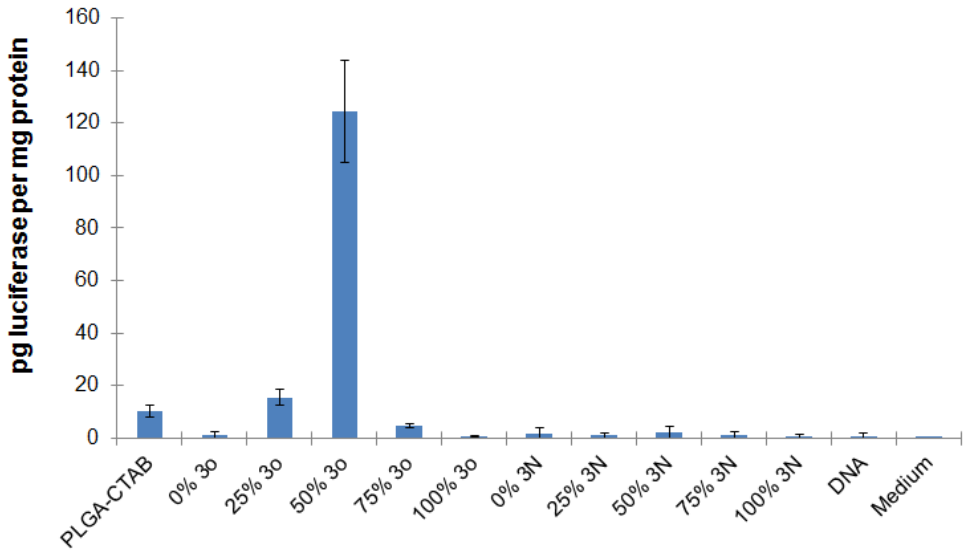

Figure 5-5. Gene transfection of different microparticle formulations on macrophage cells. For the hydrolysable particles, optimized transfection efficiency was achieved at a 1:1 tertiary to quaternary ratio, which is about twelve times higher than the PLGA-CTAB control. All of the nonhydrolysable particles showed very low transfection efficiency.

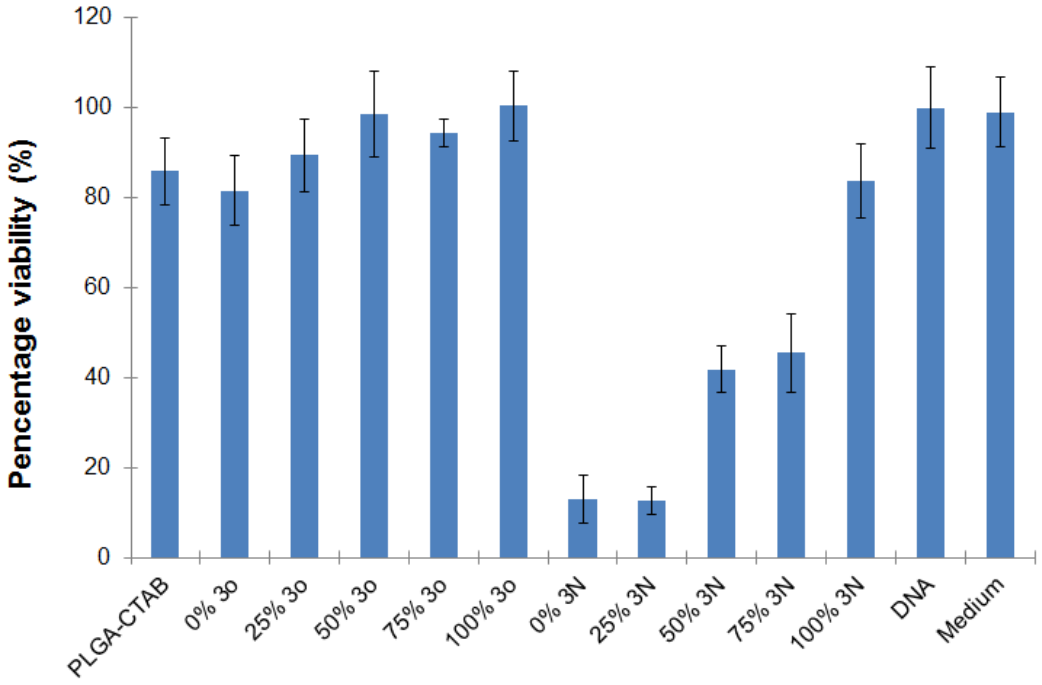

Figure 5-6. Cytotoxicity tests of all microparticle formulations. All the hydrolysable particles presented low cytotoxicity to the macrophage cells, while for the nonhydrolysable particles, the increase of quaternary ratio lead to significant increase of cytotoxicity.

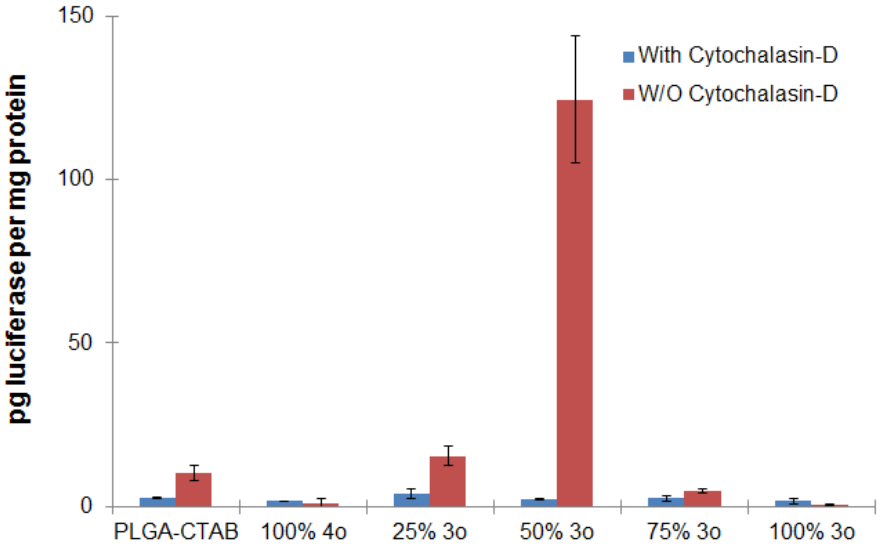

Figure 5-7. Passive targeting tests for microparticle formulations. At a concentration of 10 μM cytochalasin-D, phagocytosis of macrophage cells was blocked, consequently inhibiting the gene transfection.

Chapter 6 Softer Zwitterionic Nanogels for Longer Circulation and Lower Splenic Accumulation

Zwitterionic nanogels of varying stiffness were prepared by tuning their crosslinking densities and reactant contents. *In vivo* studies of these nanogels show that softer nanogels pass through physiological barriers, especially the splenic filtration, more easily than their stiffer counterparts, consequently leading to longer circulation half-life and lower splenic accumulation. Results from this work emphasize the role of stiffness in designing long-circulating nanoparticles.

6.1 Introduction

Long circulating nanoparticles are highly desirable in drug delivery and diagnosis [7, 120]. Nanoparticles can encapsulate therapeutic drugs and/or imaging reagents, such as magnetic nanoparticles for magnetic resonance imaging (MRI) or quantum dots for fluorescence imaging [30, 121]. They are commonly administrated into the body via intravenous injection, can stay in the circulation for a desirable long period and travel with the blood stream to their targeted site to accumulate in a favorable amount. Long circulating nanoparticles have two major advantages. They can efficiently stabilize and protect their loadings which are either unstable in physiological environment or will be quickly degraded in the blood or cleared from the blood circulation. A the same time, they can preferentially deliver their loadings to the targeted site to improve their therapeutic efficiency and/or imaging sensitivity, as well as to reduce accumulation in

normal tissues, and thus avoid any potential side effects [120, 122]. Therefore, long circulating nanoparticles are attracting significant attention and are expected to revolutionize current medical treatments.

To achieve long circulation time *in vivo*, nanoparticles need to be elaborately designed to overcome the intrinsic defense system of the body and the *in vivo* physiological barriers. Several physiological factors are regarded as the important reasons for the clearance of the nanoparticles. First, the blood is a heterogeneous complex medium containing ions, proteins and blood cells, etc. It has been well recognized that immediately after nanoparticles enter the blood stream, they are susceptible to nonspecific plasma protein adsorption, known as opsonization [123]. This phenomenon will result in the recognition of the "protein contaminated" nanoparticles by the reticuloendothelial system (RES), which mainly locates in liver, spleen and bone marrow [13], subsequentially leading to the clearance of the nanoparticles by the RES. Second, nanoparticles in blood circulation are susceptible to splenic filtration. The spleen is the biggest filter of the body. Its unique structure enables the removal of older erythrocytes from the blood circulation as well as blood-borne microorganisms and cellular debris [124]. Spleen can also filter nanoparticles. It has been reported that the slit size in spleen rarely exceeds 200 to 500 nm in width, even with an erythrocyte in transit [7]. But biodistribution studies in the literature show that the spleen has strong capability for the filtration of nanoparticles even smaller than 100 nm, and spleen has even higher uptake

of nanoparticles per unit mass than liver [125, 126]. Third, although smaller nanoparticles can better avoid splenic fitration, nanoparticles smaller than 20 nm can be excreted by renal clearance in kidney. The smaller the nanoparticles, the faster the excretion rate [49].

By considering all these factors, a nanoparticle should have the following characteristics in order to exhibit long blood circulation. First of all, nanoparticles need to have a stealthy surface coating in order to efficiently stabilize them in complex media and minimize opsonization after they are injected into the blood stream. Thus, the nanoparticles can evade non-specific uptake by the RES. Furthermore, the nanoparticles need to be designed to bypass several *in vivo* clearance mechanisms, such as the splenic filtration and the renal clearance, to remain in the blood circulation [7].

Current studies of long circulating nanoparticles are mainly focused on optimizing nanoparticle sizes or coating thicknesses. For example, Perrault *et al* coated gold nanoparticle cores of five different sizes with polyethylene glycol (PEG) of three different molecular weights and tested circulation time of the PEGylated gold nanoparticles in a mouse model [125]. Results showed that the nanoparticles with the smallest core, but the largest PEG possessed the longest circulation time. In addition, several studies showed that the nanoparticles shapes could also influence the circulation time and biodistribution. Non-spherical nanoparticles were found to have longer circulation time than their spherical counterparts [127, 128].

While the effects of nanoparticle surface coatings, nanoparticle sizes, and shapes

have been studied, the mechanical properties of nanoparticles have not been well investigated yet. Mechanical properties play an important role in many biological processes. For example, red blood cells can pass through splenic filtration due to their extraordinary deformability and flexibility. Therefore, they have an *in vivo* longevity of about 120 days. Aged red blood cells finally get cleared from the blood circulation by splenic filtration because they become rigid and have lost these properties [124]. To prepare artificial red blood cells for biomedical applications, mechanical properties are one important design parameter. Interestingly, Desimone *et al*. showed the circulation time and biodistribution of micrometer-sized hydrogel disks (about 6 μm in diameter and 2 μm thick) mimicking red blood cells [129]. Several micro-disks of varying stiffness were tested. Results showed that softer particles could pass through lung tissue better and possess longer circulation time while their stiffer counterparts were mostly entrapped in lung tissue. In this work, we demonstrate nano-sized particles (i.e., nanogels of about 100nm in diameter) with tunable flexibility, study the relationship between the mechanical and *in vivo* biological properties of engineered nanoparticle, and push the limit of their blood circulation time. Prolonged circulation time can render the nanoparticles less uptake by the RES and better chance to arrive the target sites, leading to better efficiency. Long circulation time is fundamentally important for many biomedical applications such as drug delivery and molecular imaging [7].

One efficient method of tuning mechanical properties (e.g., stiffness) of biomaterials

is to change their crosslinking density in hydrogels. However, because of the different nature of the monomers and the crosslinkers, this method inevitably induces change in the surface properties of hydrogel as the hydrogel composition varies. Tuning the stiffness of the nanogels without compromising their surface properties still remains a challenge [130].

Here, we present a solution to make stealthy nanogels with tunable "softness" by using zwitterionic monomers and crosslinkers. Zwitterionic materials, such as poly(carboxybetaine) (PCB) and poly(sulfobetaine) (PSB), have been emerging as a new class of materials for constructing long circulating nanoparticles. They have proved their excellent ultralow fouling properties (< 0.3 ng/cm^2 adsorbed proteins) on flat surfaces [4] or nanoparticle surfaces [43]. It was demonstrated that PCB coated magnetic nanoparticles (PCB-MNPs) had the long term stability in both saline solutions and 100% human blood serum. These *in vitro* studies revealed PCB-MNPs could efficiently evade the uptake of nonspecific macrophage cells, indicating their weak interactions with the RES [6]. However, the *in vivo* environment is far more complicated than any existing *in vitro* models. *In vivo* experiments need to be conducted to evaluate the blood circulation time of PCB nanoparticles. In this work, we prepared stealthy PCB nanogels with different stiffnesses by tuning their crosslinking densities and solid contents. A zwitterionic crosslinker containing a carboxylbetaine group was used to make the nanogels completely zwitterionic without compromising the stealthy properties of the

nanogels [131].

6.2 Experimental

6.2.1 Preparation of PCB nanogels encapsulated with gold nanoparticles

Poly CB nanogels loaded with gold nanoparticles were prepared by inverse microemulsion polymerization method [116].

To prepare nanogels for *in vivo* tests, 1.4 g Tween 80, 2 g Span 80 and 4 mg V-70 were dissolved in 20 mL of hexane and kept in ice bath. 25 mg gold nanoparticles (~ 10 nm), CBMA and CB crosslinker were dissolved in 0.35 mL of DI water. The reactant content is 46% for four nanogel samples with crosslinking densities of 2%, 5%, 10% and 15%. One sample has reactant content of 40% with 2% crosslinking density. The two stock solutions were mixed in a 100 mL flask with vigorous stirring, then strong sonication was applied to form the microemulsion. The flask was purged with nitrogen at 4 ^{o}C for 30 min to remove dissolved oxygen. During polymerization, the reaction was kept at 40 ^{o}C with stirring and was protected under nitrogen for 12 h. After the reaction, the product was washed by tetrahydrofuran for 3 times to remove the surfactants, then the product was dispersed in DI water and other impurities were removed by using a 100 kD molecular-weight-cutoff Amicon Ultra centrifugal filter.

To prepare nanogels for the syringe filtration test, 0.2 g Tween 80, 0.3 g Span 80 and 4 mg V-70 were dissolved in 20 mL of hexane and kept in ice bath. 25 mg gold nanoparticles (~ 10 nm), CBMA and CB crosslinker were dissolved in 0.5 mL of DI

water. The reactant content is 46% and the crosslinking densities are 2% and 15%.

6.2.2 Macrophage uptake test

RAW264.7 cells were cultured in DMEM medium with 10% FBS and 1% antibiotics in a 6-well plate. Prior to the test, cells were washed with PBS three times, and gold nanoparticles loaded nanogels at gold concentration of 5 ppm in culture media were added. After 4 h incubation at 37 ^{o}C, 5% CO_2, cells were washed three times with PBS and lysed with 1 mL of 50 mM NaOH solution. Intracellular iron content was determined by the ICP-AES method.

6.2.3 *In vivo* studies.

The *in vivo* circulation time and biodistribution of PCB nanogels are studied using Spraque Dawley rats (body weight 150 g) as the animal model. Each nanogel sample has three duplicates to generate statistical significance. All animal experiments adhered to federal guidelines and were approved by the University of Washington Animal Care and Use Committee. To study the *in vivo* circulation time, 100 μL of each nanogel sample was administrated into the rat *via* tail vein injection at the dose of 1mg gold per kg body weight. At 5 min, 4 h, 8 h, 24 h, and 48 h after the injection, a 50 μL blood sample was collected, digested and analyzed by the elementary analysis method, inductively coupled plasma (ICP). The *in vivo* biodistribution was tested 48 h after the nanogel samples injection. The animals were euthanized by CO_2 inhalation, and the organs (heart, liver, spleen, lung, kidneys and brain) were collected, lysed in aqua regia, and analyzed by ICP.

6.3 Results and discussion

To validate our hypothesis *in vitro*, two types of PCB nanogels (one stiff and one soft) were prepared, using 46% reactant content with 15% and 2% crosslinking densities, respectively. The mean hydrodynamic sizes of both the nanogels were tuned to be around 0.25 μm. Syringe filters with cellulose acetate membranes with a pore size of 0.22 μm were used to test the ability of the nanogels to pass through slits narrower than their sizes. The cellulose acetate membrane is hydrophilic and does not adsorb the nanogels on its surface. Both of the nanogel samples show purplish red color due to their encapsulation of gold nanoparticles. The filtration tests are shown in Figure 6-1. For the "hard" nanogel sample (Figure 6-1a), the filtrate collected in the cuvette was almost transparent, indicating most of the hard nanogels were stopped by the filter. Elementary analysis of gold showed that only 6% of the stiff nanogels were found in the filtrate. In contrast, as shown in Figure 6-1b, the soft nanogels could efficiently pass through the filter, the filtrate collected in the cuvette showed similar color as the original sample. Nearly 100% of the soft nanogels could be found in the filtrate. The hydrodynamic size of the soft nanogels after filtration was also tested; no change could be observed, indicating the nanogels remained intact during filtration. Scanning electron microscopy (SEM) images (Figure 6-2) of soft nanogels before and after filtration further proved the integrity of the nanogels after filtration. No leakage of gold NPs happened during the filtration. This result suggests that the soft nanogels are able to pass through narrow slits due to their deformability, as illustrated in Figure 6-1c and 6-1d.

For the *in vivo* tests, five different PCB nanogels with different stiffnesses were

prepared using different reactant formations: 46 % solid content with 15%, 10%, 5% and 2% crosslinking densities (denoted as “15%”, “10%”, “5%” and “2%”) and 40 % solid content with 2% crosslinking density (denoted as “2%-“). Gold nanoparticles are used as a detectable marker and encapsulated in the nanogels, noting that the gold concentration in the blood can be negligible. Thus, the blood concentration of the nanogels samples can be analyzed by an elementary method.

All the PCB nanogels prepared for *in vivo* tests possess the similar hydrodynamic size of about 120 nm with a polydispersity index (PDI) < 0.1 in phosphate buffered saline (PBS) solution as determined by dynamic light scattering, indicating their uniform size distribution, and their size remains unchanged in PBS solution for at least 60 days, as shown in Figure 6-3. They presented a uniform morphology under SEM, as shown in Figure 6-4. Macrophage cell uptake tests were conducted to confirm the stealthy properties of all nanogels. When incubated in the medium with macrophage cells, protein adsorption from the cell culture medium onto the surface of nanoparticles can lead to cellular recognition and uptake. As shown in Figure 6-5, all nanogel samples, regardless of their crosslinking densities, showed a negligible uptake amount as compared to blank cells and uncoated gold nanoparticles, indicating their strong ability to evade recognition by macrophage cells. While the nanogel samples have similar hydrodynamic sizes, zeta potentials, gold concentrations, and stealthy properties, the only difference is their stiffness. As presented in Table 6-1, the “2%-” sample has the lowest stiffness while the

"15%" sample has the highest stiffness.

The *in vivo* circulation results are shown in Figure 6-6. The circulation half-lives of all samples in rats, ranging from 9.1 h to 19.6 h, were calculated using a one-compartment model and listed in Table 6-1. Perrault et al. reported the circulation studies of several PEG coated gold nanoparticles with a hydrodynamic size of around 100 nm in a mouse model. These particles possessed *in vivo* circulation half-lives from 3.3 h to 11.3 h (also calculated from a one-compartment model), depending on the molecular weights of PEG and the core sizes of gold nanoparticles [125]. Several other long circulating nanoparticles have circulation half-lives around 10 h [49, 132, 133]. Thus, all the samples in this work can be considered to possess long-circulating properties. It has been reported that uncoated gold nanoparticles are quickly cleared from blood circulation after intravenous injection [125, 134]. Therefore, our results show the strong ability of PCB polymer to protect gold nanoparticles from being cleared. Moreover, it can be clearly observed from the circulation profiles that nanogel samples of varying stiffness have different blood retention half-lives at the same time point. In general, softer nanogels can remain in the bloodstream longer than their stiffer counterparts. As discussed previously, this phenomenon is likely because softer nanogels have better deformability to pass through *in vivo* barriers, especially in the spleen, which is well known for filtering out rigid particles from the blood circulation.

To further investigate how the nanogels were cleared from the blood circulation,

biodistribution studies were performed and the accumulation of nanogel samples in different organs 48 hours after administration was tested. As shown in Figure 6-7, liver and spleen are the major organs responsible for removing nanogels from blood circulation as reported in the literature [125, 133, 135], since they are the major RES organs clearing foreign blood-borne particulate entities. As expected, other organs show much lower accumulation of the nanogels. Unlike spleen, accumulation of the nanogels in liver as well as other organs shows no significant difference. This is likely due to the fact that all the nanogel samples have similar surface properties, as shown in the *in vitro* update tests of macrophages. Thus, they have similar interactions with the RES tissue in liver and other organs. In contrast, accumulation in spleen shows obvious difference among different nanogel samples. The splenic accumulation significantly increases as the nanogels become stiffer, from sample "2%-" to sample "10%", while no significant difference can be observed for the 10% and 15% samples. These results show a strong capability for the filtration of nanoparticles by the slits in the walls of venous sinuses in spleen [7]. Consistent with the *in vitro* test, softer nanogels can pass through those slits better and remain in the circulation, while harder nanogels can be retained or trapped and consequently are cleared by the red-pulp macrophages [124].

To correlate the circulation and biodistribution studies, the circulation half-life was calculated using a one-compartment model, and plotted together with the splenic accumulation data. As shown in Figure 6-8, softer nanogels have longer circulation time,

but less splenic accumulation. Consistent with our hypothesis, softer nanogels are able to overcome those *in vivo* barriers better, and spleen is the major organ that clears stiffer nanogels.

6.4 Conclusions

In this work, we demonstrate the long circulating properties of PCB-based nanoparticles using PCB nanogels. Results show that the stiffness of nanoparticles plays an important role in their *in vivo* behaviors. Softer particles are preferred due to their deformability. The findings from this work open new opportunities for the design of long circulating nanoparticles. It can be a possible solution for some dilemmas in certain applications. For example, when long circulating drug loaded nanoparticles are prepared, there is a tradeoff between drug loading and circulation half-life. Smaller particles have longer circulation half-life, but less drug loading and easier drug leakage while larger particles can improve the drug loading and retain drug better, but with shorter circulation half-life [136, 137]. Base on this work, a potential solution is to design larger, but softer particles with higher drug loading and longer circulation half-life. Our previous work has shown the ability of PCB nanogels to load and release macromolecular drugs, indicating their potential to achieve this goal.

TABLE 1. *In vitro* and *in vivo* characterization of PCB nanogels.

Crosslinking density	Hydrodynamic size (nm)	PDI	Zeta potential (mv)	Gold concentration (%)	Modulus of bulk hydrogel (MPa)	*In vivo* circulation half-life (hour)
15%	117.5±4.8	0.07±0.02	-4.5±1.3	11.9±0.3	1.35±0.02	9.1±2.5
10%	120.4±3.4	0.06±0.01	-5.7±2.6	12.2±0.2	0.87±0.03	10.2±1.8
5%	121.8±5.9	0.08±0.02	-3.1±1.5	11.9±0.4	0.58±0.08	11.8±1.7
2%	119.6±3.7	0.06±0.01	-4.8±1.7	12.1±0.3	0.26±0.04	15.0±1.8
2% -	123.3±5.1	0.08±0.01	-3.9±1.3	12.8±0.2	0.18±0.03	19.6±1.5

Figures

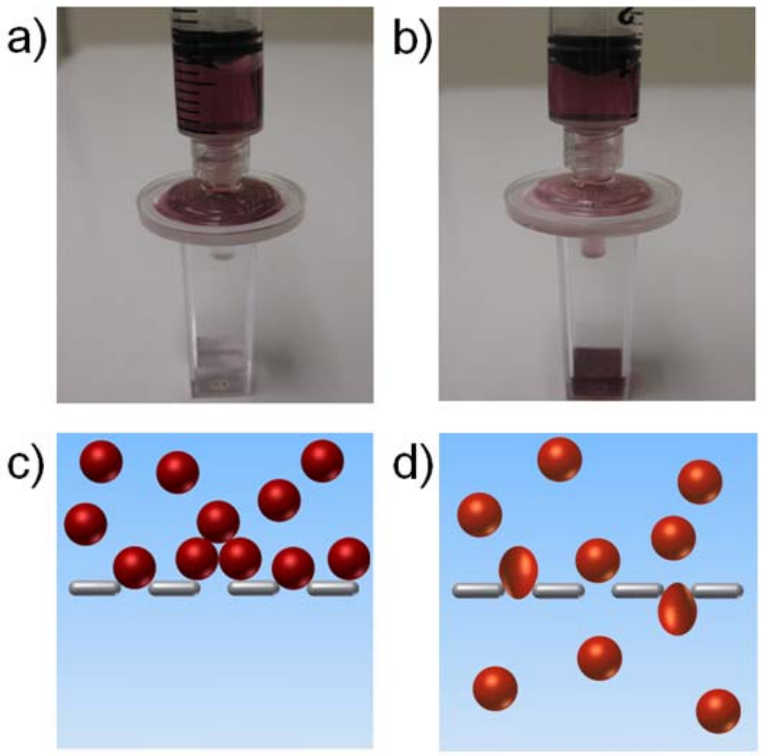

Figure 6-1. Photo images showing the ability of hard (a) and soft (b) nanogels with a mean hydrodynamic size of 0.25 µm to pass filters with a pore size of 0.22 µm. Schemes showing the interactions of hard particles and soft particles with slits smaller than their size; the hard particles (c) are trapped by the slit, while the soft particles (d) can deform and pass through the slit.

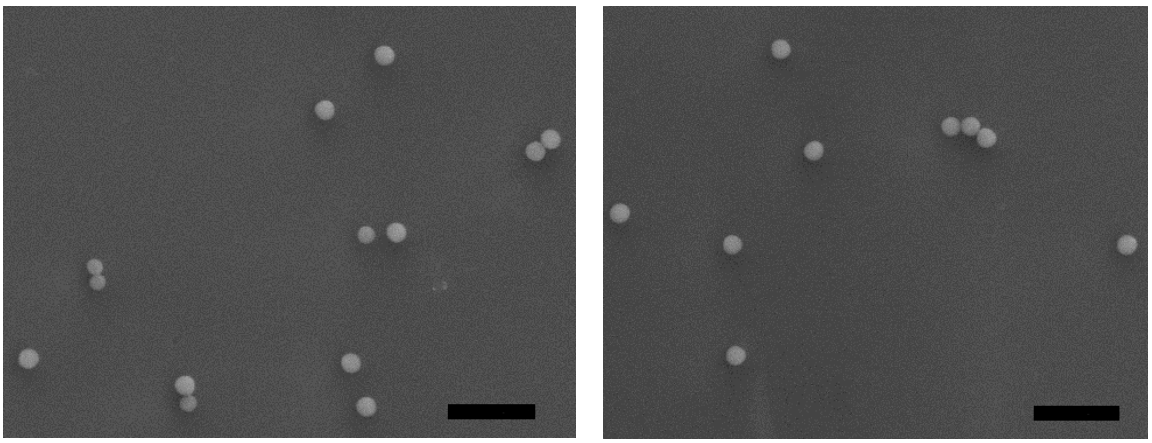

Figure 6-2 SEM images of soft nanogels before (left) and after (right) filtration by the filter. No leakage of gold nanoparticles can be observed in the nanogels after filtration. Scale bar is 1 μm.

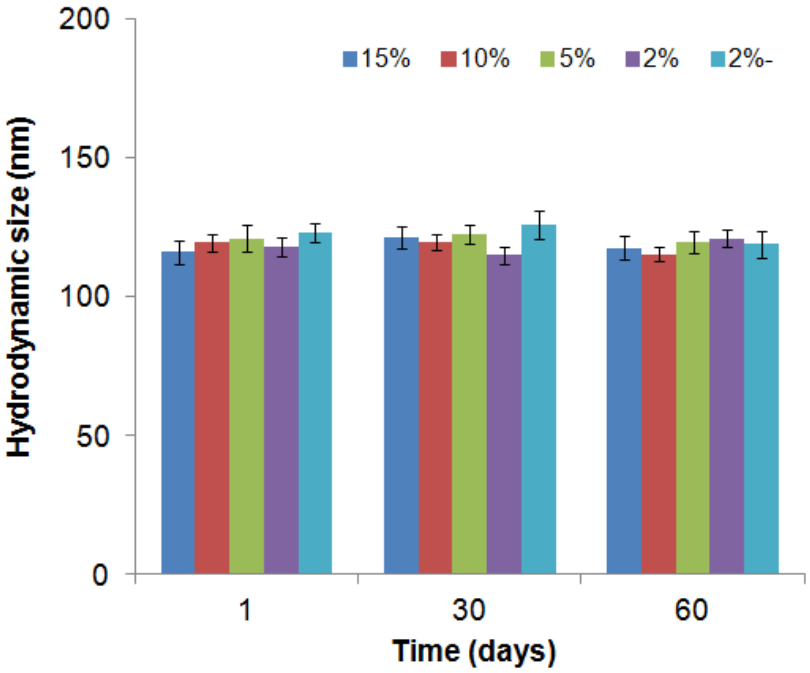

Figure 6-3. Stability of the different PCB nanogels in PBS solution tested by DLS (n=3)

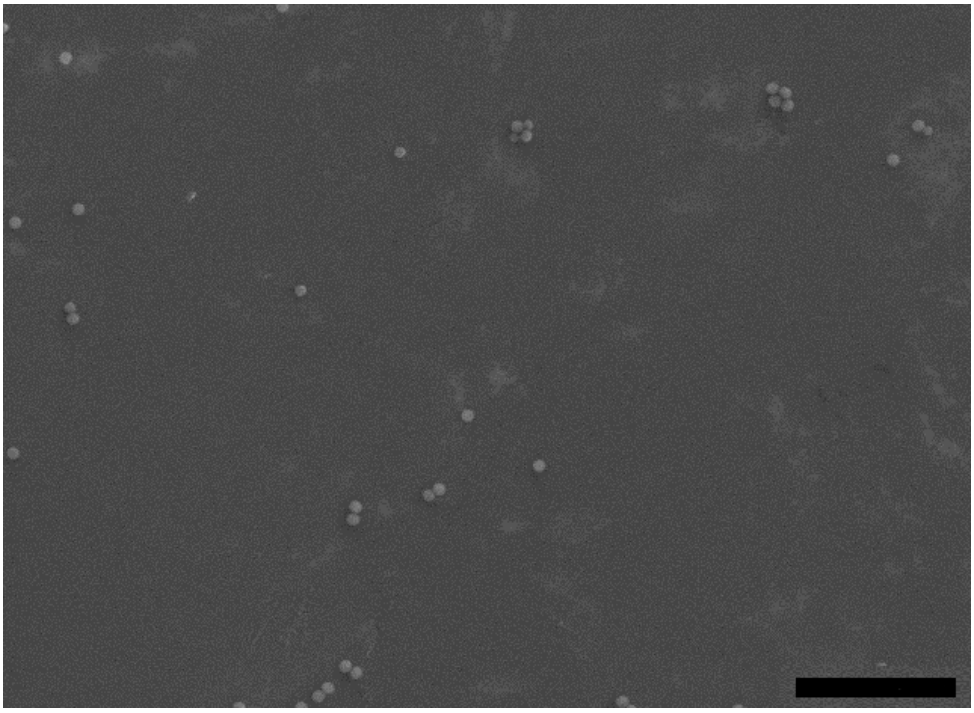

Figure 6-4 SEM image of nanogels with 5% crosslinking density for *in vivo* studies. Scale bar is 2 μm

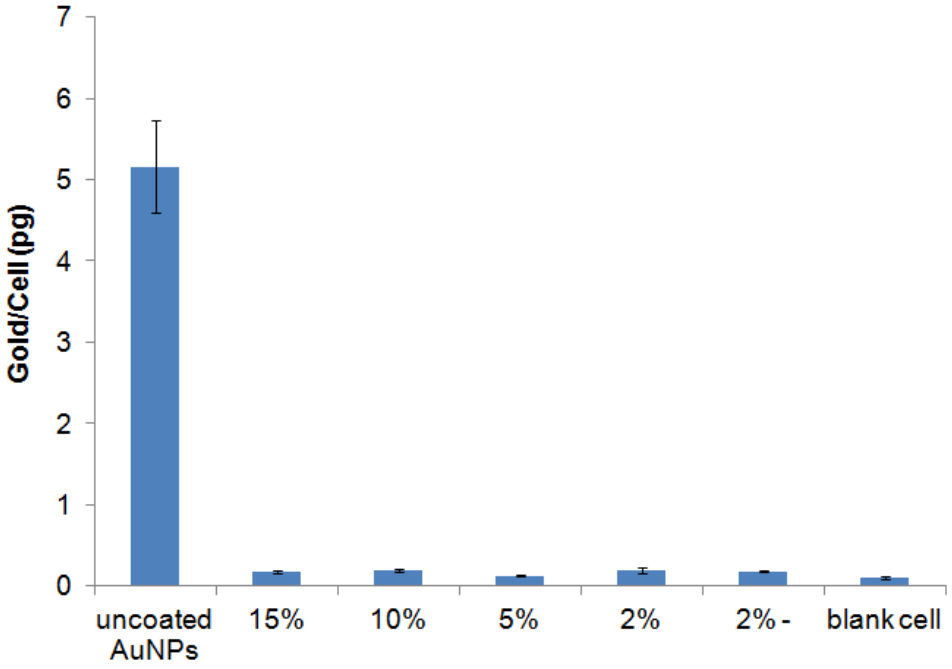

Figure 6-5. Macrophage cells uptake of uncoated gold nanoparticles (AuNPs) and different PCB nanogels at gold concentration of 5 ppm (n=3)

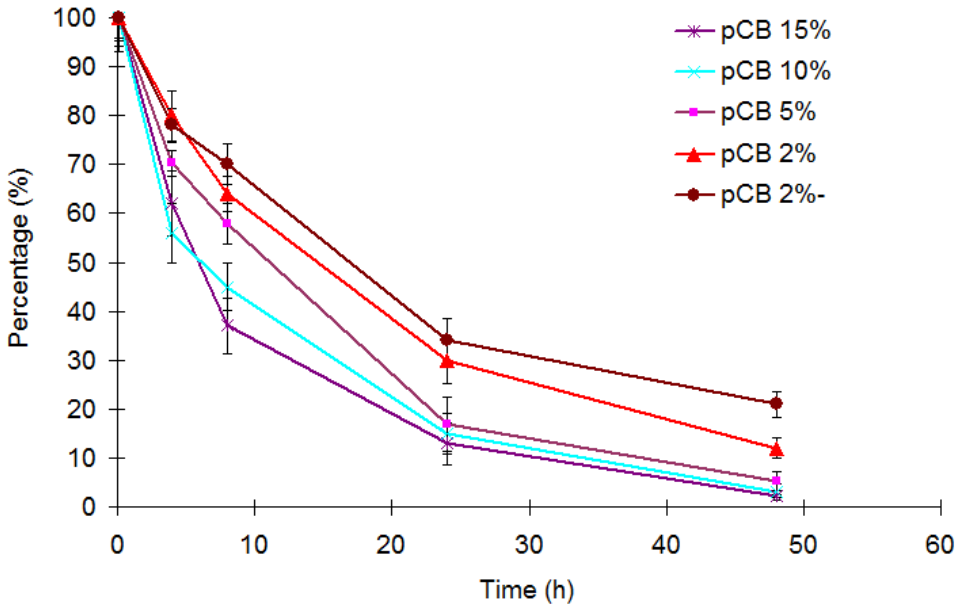

Figure 6-6. *In vivo* blood circulation profiles of nanogels of varying stiffness encapsulated with gold nanoparticless.

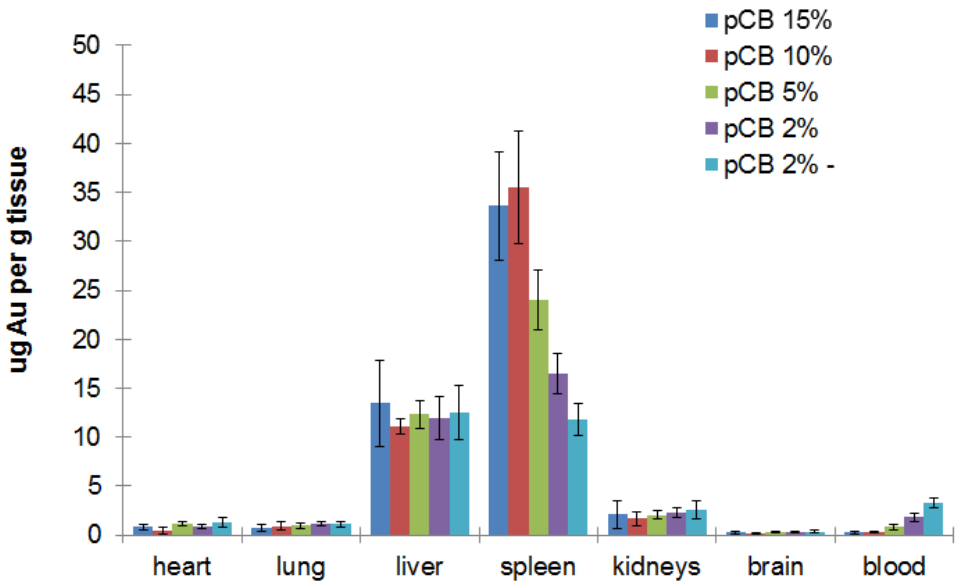

Figure 6-7. Biodistribution of PCB nanogels with of verying stiffness 48 hours after injection. Except for between the "10%" and "15%" samples, all samples show a significant decrease ($p<0.05$) in splenic accumulation as their stiffness decreases.

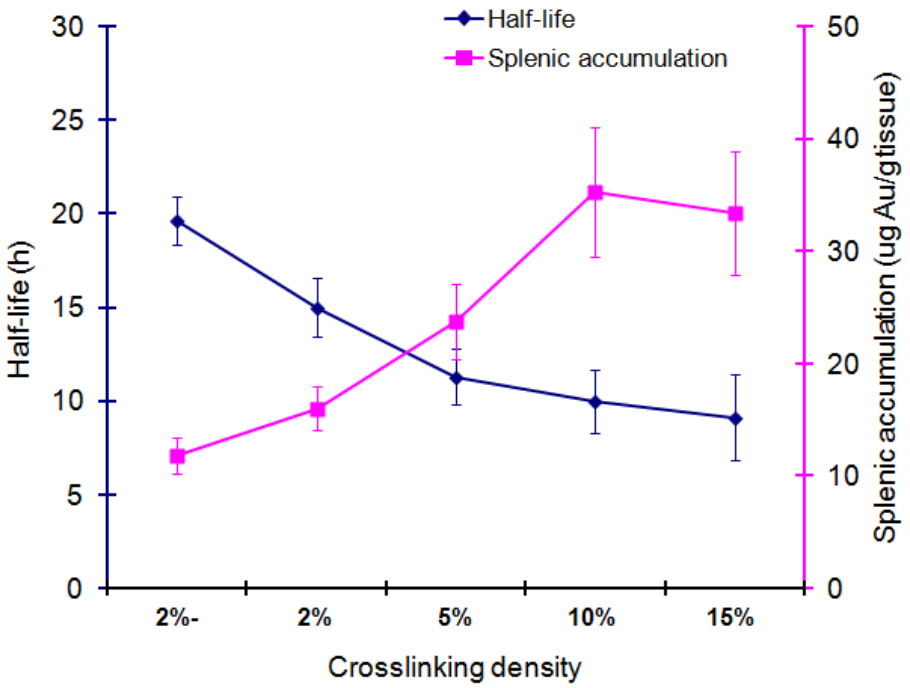

Figure 6-8. Circulation half-life and splenic accumulation of different nanogel samples.

Chapter 7 Inhibition of Foreign Body Capsule Formation by Implanted Zwitterionic Hydrogels

The foreign body reaction has been a long-standing obstacle impeding the performance of implantable medical devices due to the formation of a dense collagenous capsule that can isolate these devices from the body and block mass transport and/or electric communication with the body. Numerous materials have been tested, but none have been able to eliminate capsule formation. In this work, we demonstrate that ultra-low fouling zwitterionic hydrogels can resist the formation of a capsule for at least three months after subcutaneous implantation in mice. Moreover, zwitterionic hydrogels can also promote angiogenesis in their surrounding tissue, which is beneficial to the transport of molecules between the body and implants. Findings in this work open new opportunities for the development of biocompatible and high-performance implantable medical devices.

7.1 Introduction

Materials or devices implanted in the body play an important role in drug delivery, *in vivo* sensing, artificial prostheses, and tissue engineering [1, 138-141]. However, these implants are encapsulated by a dense collagen capsule, produced by the body's defense system, about three weeks after implantation [16, 141]. The capsule forms on all implants and is a permeation barrier to most molecules important for detection and delivery. For

example, implanted biosensors or cell-based constructs require efficient mass transport with the environment, but fail due to the low vascularity and impermeable capsule [141, 142]. In addition, the capsule causes undesirable complications to artificial prostheses and cosmetic implants, such as distortion and pain [143, 144]. The collagenous capsule formation is one consequence of the foreign body reaction (FBR), which is used by mammals as a natural protective mechanism [142]. Here we report how we can overcome the FBR with the development of an implantable material that does not stimulate capsule formation.

The FBR is believed to be triggered by non-specific protein adsorption to materials upon implantation. Macrophage cells recognize these non-specifically "protein-labeled" implants as foreign objects, and attempt to phagocytose and digest them. Due to the large size of the implant, individual macrophages are incapable of isolating it and they fuse into foreign body giant cells, which then secrete cytokines triggering fibroblasts to deposit a dense, avascular layer of collagen. This forms the capsule, which permanently isolates the implant from the organism [16, 138, 143]. The FBR and resulting capsule has been shown to apply to many materials including Teflon, polyurethane, silicone rubber, polyethylene, poly(methyl methacrylate) (PMMA), poly(2-hydroxyethyl methacrylate) (PHEMA), poly(ethylene glycol) (PEG), Dacron, gold, titanium, and alumina. Materials in this list are hydrophilic, hydrophobic, hard, soft, polymeric, metallic or ceramic [16, 142]. Since initial protein adsorption on the implant surface has been associated with the first step that triggers the foreign body reaction, we hypothesize that a non-fouling

material can eliminate consequential capsule formation [4, 145].). PEG and PHEMA have been the most widely used low-fouling or non-fouling materials and they have been successfully applied to microparticles or nanoparticles for drug or nucleic acid delivery [129, 146, 147]. However, when these polymers are crosslinked to form hydrogels and used as implants, even these are encapsulated. The latter also suffers from instability *in vivo* due to oxidization [16, 145, 148]. Recently, zwitterionic materials, such as poly(carboxybetaine) (PCB), have emerged as a new class of materials that are robust and ultra-low fouling. They have been shown to adsorb < 0.3 ng/cm^2 protein from 100% blood serum or plasma, and can be used to prepare stealthy nanoparticles [4, 6]. As suggested schematically in Figure 7-1 and shown in Figure 7-3, hydrogels made from crosslinked carboxybetaine chains can strongly resist capsule formation in a mouse implantation model for at least three months, while neither PHEMA nor PEG are capable of this. Moreover, PCB promoted angiogenesis in the surrounding tissue, which is also beneficial to mass transport of molecules between the body and the implants. This may be associated with macrophages differentiating to the pro-healing (M2) state.

7.2 Experimental

7.2.1. Preparation of hydrogel samples

The CBMA monomer and CBMAX crosslinker were synthesized using a previously published procedure [131]. The PCBMA hydrogels were prepared by crosslinking CBMA monomer with CBMAX as reported previously [131]. To evaluate the influence of crosslinking density to the *in vivo* performance, four different formulations were made by

substituting monomer for crosslinker in increasing amounts, the percentage of crosslinker includes 0.5 mole%, 5 mole%, 20 mole%, and 100 mole%. 100% means the whole hydrogel was formed out of crosslinker. Compared with other crosslinkers, using CBMAX can make the whole hydrogel based out of one material—carboxybetaine methacrylate, and thus minimizing the introduction of undesirable fouling moieties. Furthermore, CBMAX can also greatly improve the hydrogels' mechanical properties and subsequent integrity during the *in vivo* studies. PHEMA hydrogels, a widely used biomaterial, were used as the controls. Tetraethylene glycol dimethacrylate (PEGX) was used as the crosslinker. The PHEMA hydrogels were prepared using standard literature methods [149, 150]. The PHEMA hydrogels were consistent with the PCBMA hydrogels, i.e., the crosslinking densities were 0.5%, 5%, 20%, and 100%. The molecular structures of the above two monomers and two crosslinkers are shown in Figure 7-1A and 7-1B.

After synthesis, the hydrogels were equilibrated in sterilized phosphate buffered saline (PBS) changed three times a day for at least a week. The final thickness of all hydrogels after equilibration in PBS was about 1 mm. For implantation, the hydrogels were punched into disks with a diameter of 5 mm using a biopsy punch, and stored in sterilized PBS at 4^{o}C before use [150].

7.2.2. *In vitro* cytotoxicity and endotoxin tests

All hydrogel disks were tested for cytotoxic leachables and endotoxin levels before implantation [150]. To assess cytotoxicity, the materials were incubated at 37°C for 24 h in culture medium (Dulbecco's Modified Eagle Medium supplemented with 8% FBS

and 2% Penicillin Streptomycin) to extract soluble substances. NIH-3T3 fibroblasts at 5×10^4 cells per well were seeded in tissue-culture polystyrene multi-well culture plates. After 24 h, the culture medium was removed from the cells and the same amount of the extracting medium from incubated materials was applied to the cells and cultured for 48 h. Cell attachment and morphology were then examined under a phase contrast microscope. Endotoxins are toxic compounds from small lipopolysaccharide (LPS) molecules of lysed bacteria. The endotoxin content of the samples was determined according to the instructions provided with a Limulus Amebocyte Lysate (LAL) endotoxin assay kit (Cambrex Bioscience). In this work, the LAL endotoxin assay kit was sensitive to 0.06 endotoxin units (EU)/ml.

7.2.3. *In vivo* hydrogel disks implantation

All animal experiments followed federal guidelines and were approved by the University of Washington Animal Care and Use Committee. The hydrogel disks were implanted subcutaneously in mice for 1 week, 4 weeks, and 3 months. The implantations were performed as previously described [150, 151]. Six-weeks-old C57B16 male mice obtained from Charles River Labs were used for *in vivo* tests. Each mouse received two implants subcutaneously, one PCBMA hydrogel disk, one PHEMA hydrogel disk. Each sample had 6 replicates to provide statistical significance in the histological studies. Mice were anesthetized using isoflurane and then shaved. Surgical scissors were used to create a longitudinal incision on the central dorsal surface. A blunt forceps was used to create a subcutaneous pocket on either side of the incision for the implantation of the disks. The

dorsal skin incision on the mouse is no longer than 1.5 cm. The incision is the full thickness through the skin to enable access to the subcutaneous space. After implantation, wound clips were used to close the incisions. Mice were observed until recovery and housed for 1 week, 4 weeks or 3 months. The mice grew normally after the implantation and no weight loss was found before the explantation.

7.2.4. Explantation and histological analysis

After 1 week, 4 weeks or 3 months, mice were euthanized by CO_2 asphyxiation. The implant and surrounding tissue were excised by carefully cutting around the area with scalpel and scissor. The explanted samples were then fixed in zinc fixative overnight and embedded in paraffin wax. For each implant, 6-μm sections were cut and mounted onto slides for histological stain. The inflammatory response after 1 week was stained using hematoxylin & eosin (H&E). The collagen formation and organization after 4 weeks and 3 months was stained using Masson's trichrome stain. The blood vessels formation after 4 weeks was stained using an antibody to MECA32 [150, 152].

Macrophage (MΦ) differentiation was studied using a triple-label immunofluorescence stain as reported previously [152]. F4/80 was used as the pan-MΦ marker. Nitric oxide synthase (NOS) and MΦ mannose receptor (MMR) were used as representative markers for the M1 and M2 activation states, respectively. The sections were incubated with rat anti-mouse F4/80 antibody, goat anti-mouse MMR antibody, and rabbit anti-mouse iNOS antibody at $4^{o}C$ for overnight. Then, three types of donkey antibodies (anti-mouse, goat and rabbit) with three different fluorescence tags were used

to visualize the macrophage cells. Rat IgG, goat IgG, and rabbit IgG were used as the negative controls.

All histological images were acquired on a Nikon E800 upright microscope in bright field or epifluorescence using Metamorph software.

7.2.5. Statistical Analysis

Data are presented as means ± 95% confidence intervals. Quantification of histological sections was performed with images taken on three or four sections per animal (n = 6). A paired t-test was used to establish significance.

7.3 Results and discussion

Crosslinked poly(carboxybetaine methacrylate) PCBMA hydrogels were found to exhibit no cytotoxicity and to have undetectable endotoxin levels. We have shown PCBMA hydrogels are ultra-low fouling, inducing much lower cell adhesion than PHEMA, which has been used for some applications requiring low fouling [131, 149, 153]. Inflammatory response to the implants was evaluated at one week after implantation. Representative H&E stained images show numerous inflammatory cells (labeled in dark brown) present at the interface of the PHEMA hydrogel (Figure 7-2A). In contrast, few inflammatory cells can be found at the interface in PCBMA samples (Figure 7-2B), suggesting that a lower level of inflammation was generated in response to the PCBMA hydrogels. We believe this is due to the ability of PCBMA to resist non-specific protein adsorption, thus avoiding recognition by inflammatory cells.

Acute and chronic inflammatory responses to biocompatible synthetic polymer implants decline by 3 weeks and then a collagen capsule starts to form [152]. Thus, four weeks after implantation is selected as the first time point to study the development of the capsule and three months is selected to study the long-term performance of the implants. Masson's trichrome stain was used to characterize capsule formation for all samples. Results are shown for four-week samples and for three-month samples in Figure 7-4. With trichrome stain, collagen stains blue, cytoplasm stains red, and nuclei stains black. As shown in Figure 7-3A, four weeks after implantation, all PHEMA samples have been encapsulated by dense, avascular collagen, consistent with other reports in the literature [152]. At three months after implantation, they were still encapsulated (Figure 7-4A). In comparison, at both time points, all PCBMA samples presented much less of a foreign body reaction. As shown in Figure 7-3B and Figure 7-4B, collagen is loosely distributed in the tissue surrounding the PCBMA samples, looking more like normal extracellular matrix than a foreign body capsule. The foreign body reaction to PCBMA hydrogels did not show obvious change from 4 weeks to 3 months, suggesting PCBMA hydrogels were essentially invisible to the body.

The collagen densities at both time points were also analyzed in terms of blue pixel coverage percent in the images within 100 μm from the polymer-tissue interface at 10 μm steps, as shown in Figure 7-3C and Figure 7-4C. Due to the dense capsule layer, collagen density close to the interface is more than 90%, and decreases to around 40% in the

subcutaneous tissue adjacent to the capsule. It should be noted, hydrogel samples prepared from 100% PEG crosslinker, formed a capsule at both time points. PEG (or PEO) is known to be susceptible to oxidization damage *in vivo* and to lose its non-fouling properties [16, 145, 148]. Shen et al. showed a PEO-like surface that could reduce inflammatory cell attachments at one day after subcutaneous implantation; but after 4-weeks, the coating had been degraded and contained moieties that probably adsorbed protein and stimulated capsule formation [145]. In contrast, due to the absence of a dense capsule layer, collagen density for the PCBMA hydrogel samples was relatively uniform and diffuse, around 30-40% on average. Tissue with a normal, open collagen structure can be beneficial to oxygen, nutrient and metabolite exchange between the implant and the body.

The four PCBMA hydrogel samples had different mechanical properties, ranging from soft to stiff (compressive modulus of hydrogel with 0.5% CBMAX is 0.16MPa, and that of hydrogel made from 100% CBMAX is 160MPa), yet all showed similar *in vivo* performance. It is believed that the ultra-low fouling nature of these PCBMA hydrogels contributed to resisting the foreign body reaction, and thus there was no observable capsule.

Moreover, at both time points, abundant blood vessels can be found in the tissue adjacent to all PCBMA hydrogel samples, but few can be found in PHEMA hydrogel samples. Red blood cells in the blood vessels are clearly visible in the trichrome stained

histology sections suggesting that these are functional blood vessels. To further confirm blood vessel formation, the sections were stained using MECA32 antibody highlighting blood vessel endothelial cells with a dark brown color, as shown in Figure 7-5 and Figure 7-6 for both time points. Neovascularization was also evaluated by counting the blood vessel number in the slides. As shown in Figure 7-5C and Figure 7-6C, blood vessel density in all PCBMA hydrogel samples was significantly higher than that in PHEMA hydrogel samples ($p < 0.01$). The promotion of angiogenesis (or possibly the reduced inhibition of angiogenesis) shows PCBMA hydrogels have the potential to maintain the mass transport between the body and implanted devices [142]. Poly(sulfobetaine methacrylate) (PSBMA) hydrogels were previously studied *in vivo*. Though they were not shown to resist capsule formation under the conditions studied, enhanced angiogenesis was observed after subcutaneous implantation. The blood vessel density in PSBMA sample was about twice of that in PHEMA sample [150]. This work has shown that hydrogels based on pure carboxybetaine permitted neovescularizaton to a greater extent than PSBMA.

The unique *in vivo* performance of PCBMA hydrogels led us to explore the underlying biological mechanism. It has been reported that macrophages are the key driver of the foreign body reaction. They can be activated into two phenotypes (polarizations): the proinflammatory M1 state or the prohealing M2 state. M1 macrophages can secrete inflammatory cytokines and recruit additional macrophage cells

while M2 macrophages can release growth factor, promote angiogenesis and tissue remodeling. To investigate this with our materials, macrophage cell differentiation was examined with all samples [138]. Macrophage cells expressing M1 and M2 markers in the surrounding tissue were quantified by a triple-label immunofluorescence method. In this method, cells reacting with a pan-macrophage marker were labeled red, M1 macrophage cells were labeled green, and M2 macrophage cells were labeled blue. Representative fluorescence images of PHEMA and PCBMA samples are shown in Figure 7-7A and 7-7B, respectively. Macrophage cells expressing M1 and/or M2 markers (NOS and/or MMR) were counted in each fluorescence channel, and summarized in Figure 7-7C. All F4/80 positive macrophage cells fall into three groups: NOS+/MMR+, NOS+/MMR−, and NOS−/MMR+. All samples in this work had a large number of macrophage cells that expressed both M1 and M2 marker, belonging to the NOS+/MMR+ group. This is consistent with literature reports using similar methods [152]. However, PHEMA hydrogels and PCBMA hydrogels showed significant differences in macrophage cells expressing only M1 or M2 marker. With the PHEMA hydrogel samples, more macrophage cells expressed the M1 marker suggesting activation of the proinflommation pathway. In comparison, PCBMA hydrogels had an increased propensity to activate the prohealing pathway, with more macrophage cells expressing the M2 marker than with PHEMA samples ($p<0.01$). This observation is consistent with the neovascularization results, revealing that PCBMA hydrogels promote the macrophage cells in surrounding tissue to differentiate to the prohealing M2 phenotype stimulating

microvessel formation.

7.4 Conclusions

In summary, this work demonstrates that zwitterionic hydrogels prepared from carboxybetaine monomer and crosslinker are advantageous in the mitigation of the foreign body reaction. They strongly resisted the formation of the collagenous capsule in a mouse model for at least three months, and they showed enhanced microvessel formation in the surrounding tissue. These merits are highly desired for a broad spectrum of *in vivo* applications, and offer the potential to improve the performance of current medical devices such as glucose sensors, artificial organs and drug releasing devices. Additionally, they may be important in tissue engineering where fibrotic reactions are undesirable.

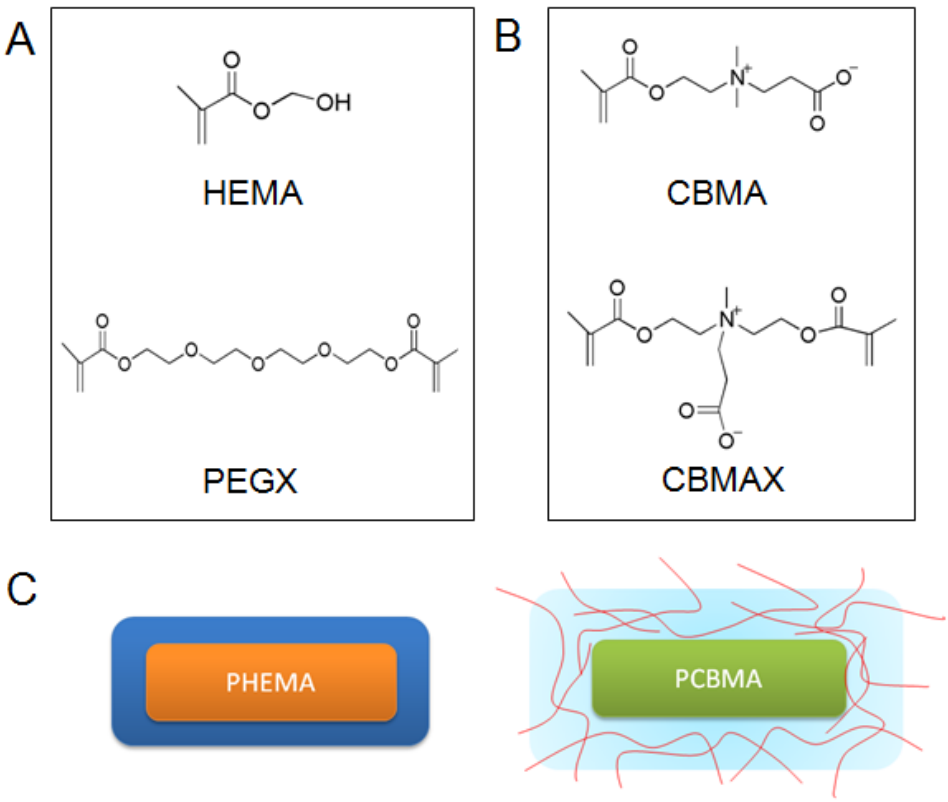

Figure 7-1. Molecular structures of (**A**) HEMA monomer and PEG crosslinker (PEGX), and (**B**) CBMA monomer and CBMA crosslinker (CBMAX). (**C**) A schematic illustration of the different *in vivo* reactions to PHEMA and PCBMA hydrogels. The PHEMA hydrogel is encapsulated by an avascular, dense collagen capsule (presented in dark blue), while the PCBMA hydrogel is surrounded by diffuse collagen (light blue) interpenetrated by abundant blood vessels (red).

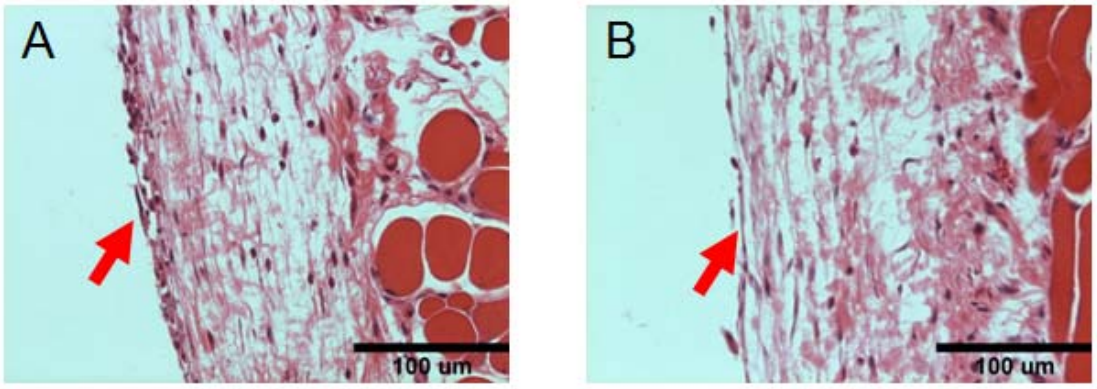

Figure 7-2 H&E stain images of samples implanted subcutaneously in mice for one week: (A) PHEMA hydrogel with 5% crosslinking density, (B) PCBMA hydrogel with 5% crosslinking density. The implant-tissue interfaces are indicated by red arrows. Scale bars are 100μm.

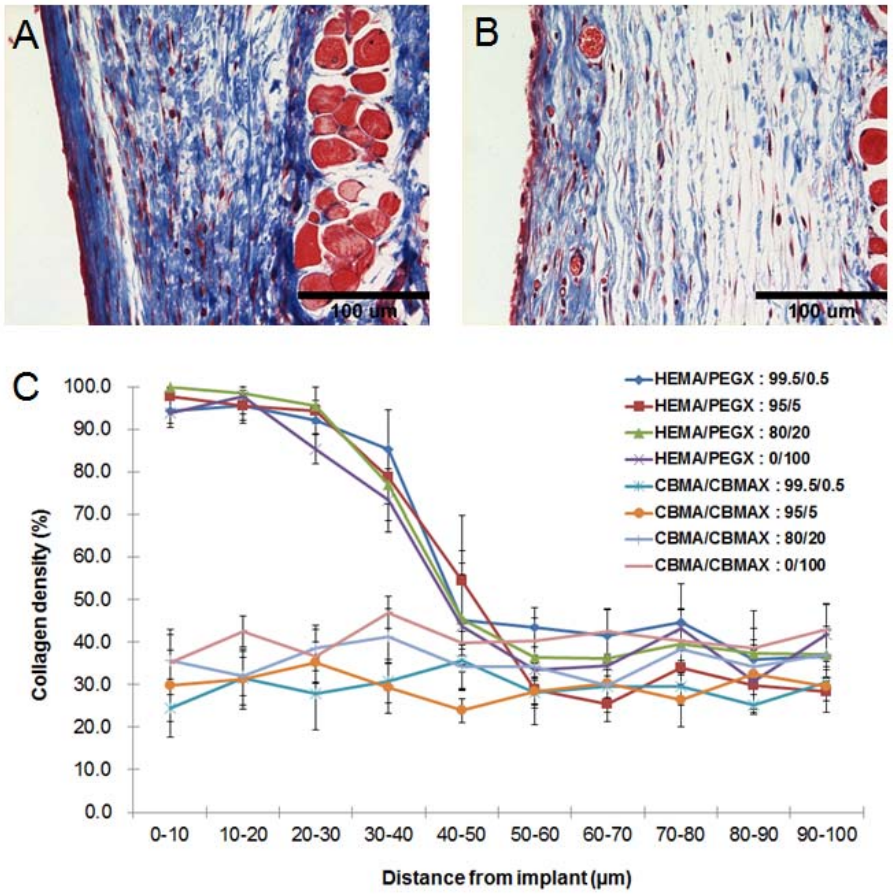

Figure 7-3 Masson's trichrome stain images of samples implanted subcutaneously in mice for four weeks: (A) PHEMA hydrogel with 5% crosslinking density, and (B) PCBMA hydrogel with 5% crosslinking density. Scale bars are 100µm. (C) Collagen density of all four-week samples -- data were collected in the tissue within 100 µm from the interface. A dense collagen capsule formed in all PHEMA samples including the hydrogel made from 100% PEG crosslinker. The collagen density near the surface is more than 90%. In comparison, due to the absence of the capsule, all PCBMA samples show a diffuse and uniform collagen distribution.

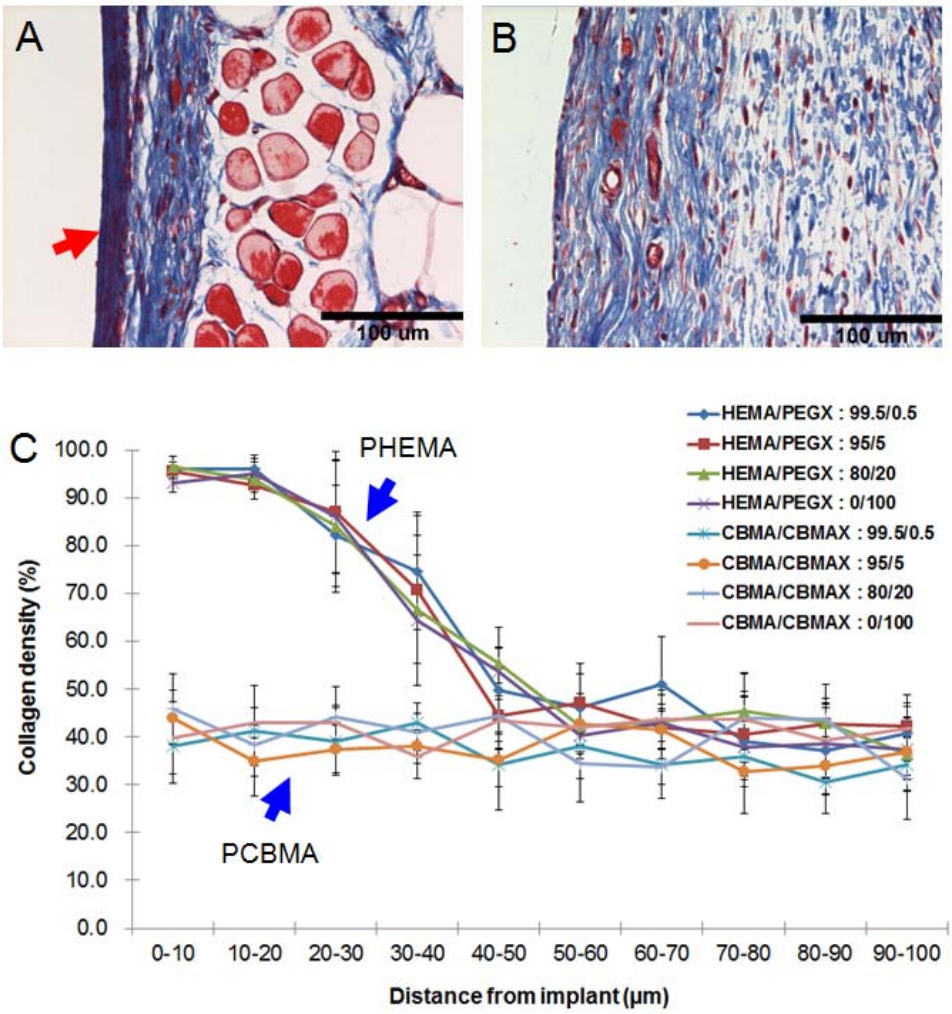

Figure 7-4. Masson's trichrome stain images of samples implanted subcutaneously in mice for three month: (**A**) PHEMA hydrogel with 5% crosslinking density; (**B**) PCBMA hydrogel with 5% crosslinking density. The implants were located on the left side of the images. The collagen capsule is indicated by red arrows. Scale bars in the images are 100 μm. (**C**) Collagen densities of all four weeks samples. Data were collected in the tissue within 100 μm from the interface. A dense layer of collagen formed around all PHEMA samples including the hydrogel made from 100% PEG crosslinker, as result, the collagen density near the surface is close to 100%. In comparison, due to the absence of the capsule, all PCBMA samples show diffuse and uniform collagen density distribution.

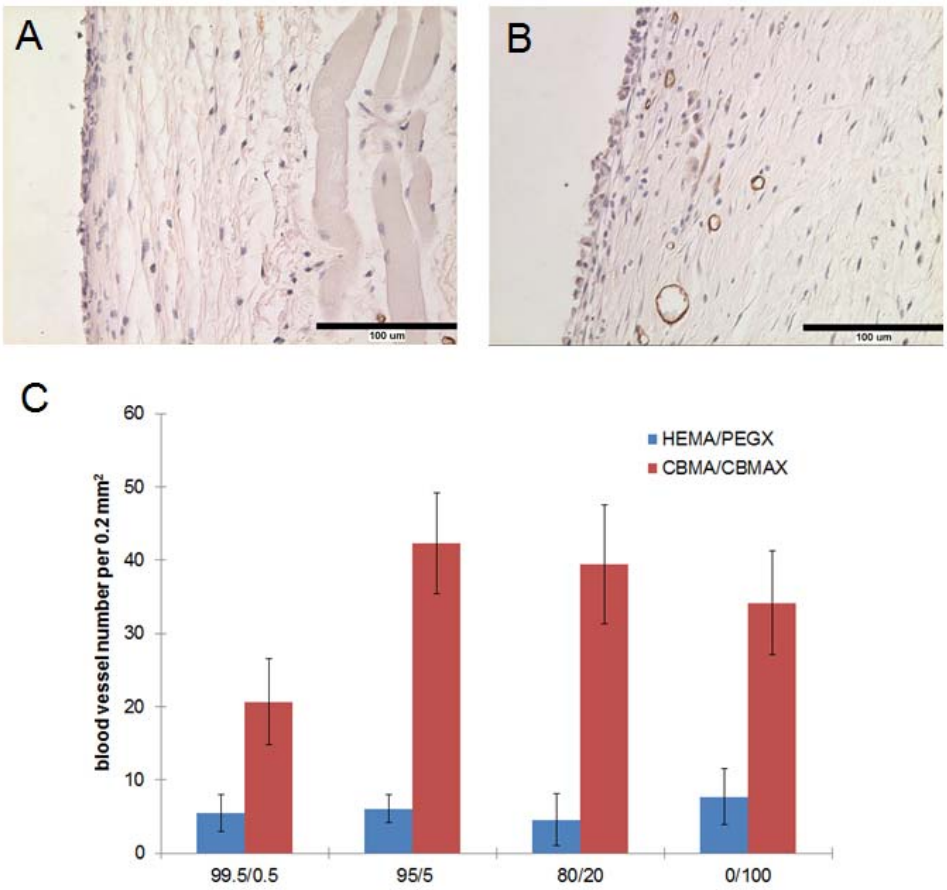

Figure 7-5. MECA32 immunostaining for blood vessel endothelial cells in four-week samples: (A) PHEMA hydrogel with 5% crosslinking density, and (B) PCBMA hydrogel with 5% crosslinking density. Blood vessels are stained dark brown. Scale bars are 100 μm. (C) Blood vessel density in the tissue surrounding the implants. Many more blood vessels can be found in PCBMA samples.

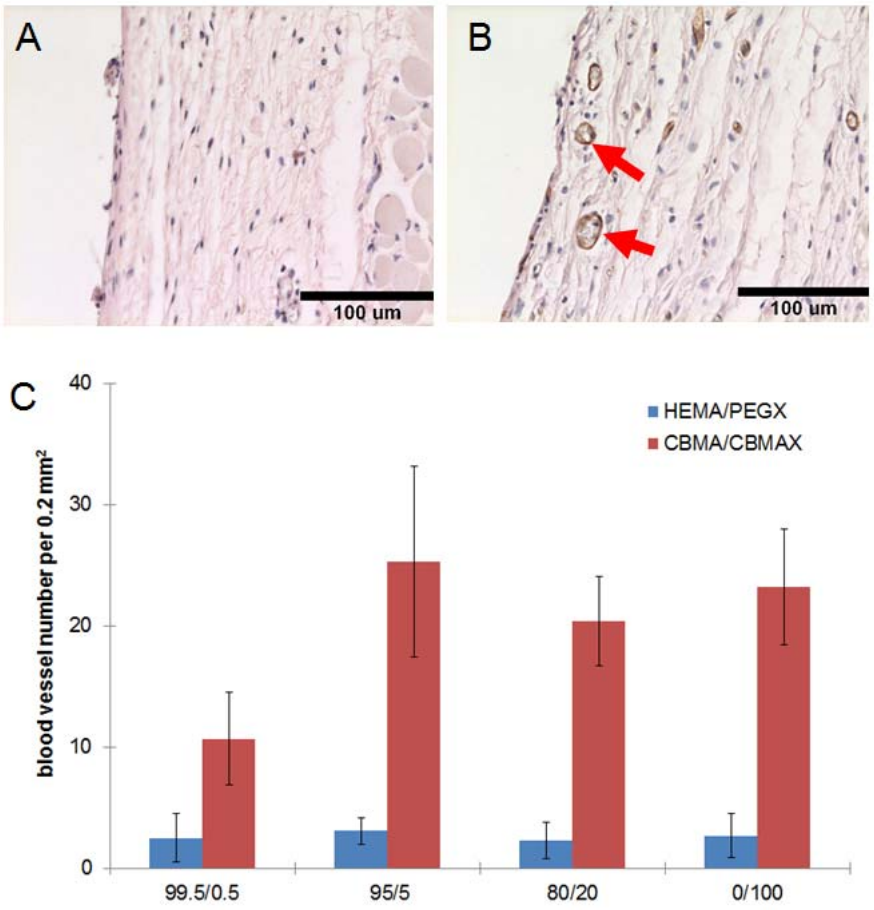

Figure 7-6. MECA32 immunostaining for blood vessel endothelial cells in three-month samples: (**A**) PHEMA hydrogel with 5% crosslinking density; and (**B**) PCBMA hydrogel with 5% crosslinking density. Blood vessels are stained dark brown and highlighted by red arrows. Scale bars are 100 μm. (**C**) Blood vessel density in the tissue surrounding the implants.

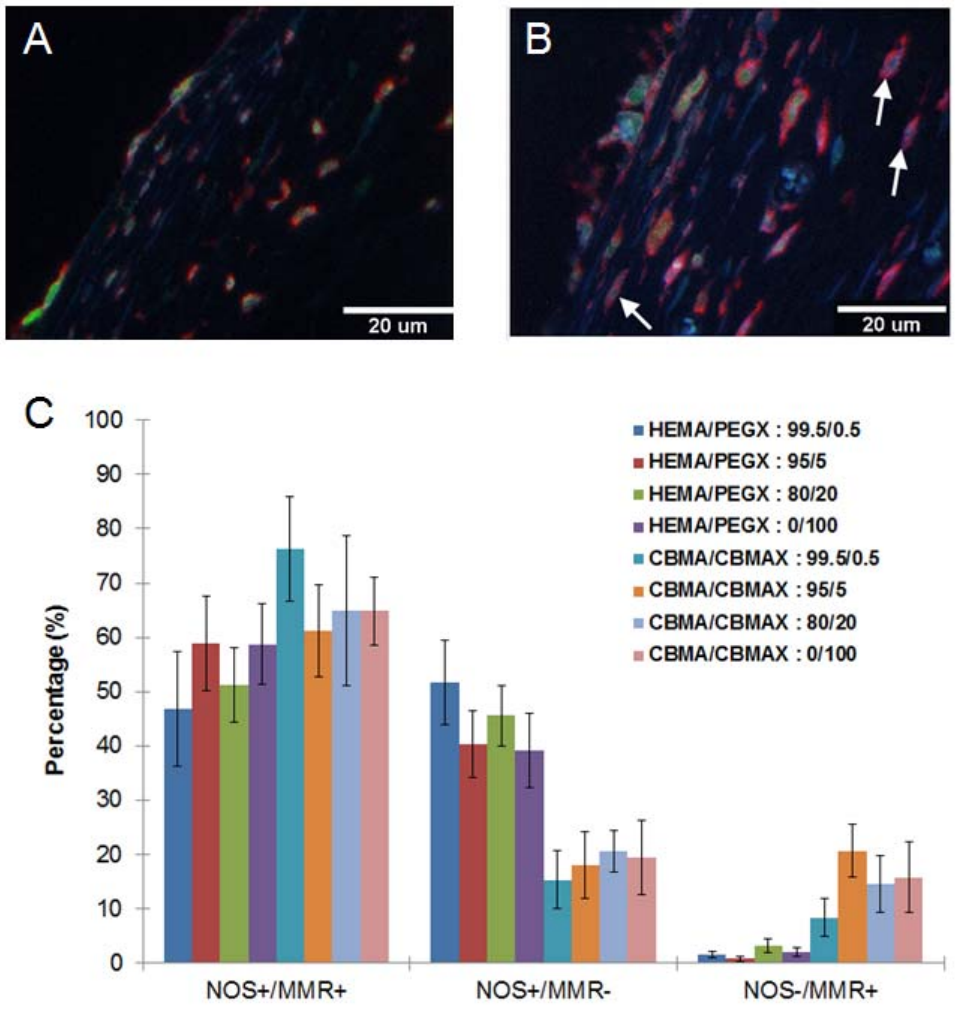

Figure 7-7. Macrophage differentiation in the tissue surrounding the implants of the four-week samples. Both M1 and M2 macrophage cell membranes were labeled red, M1 macrophage cells were labeled green, and M2 macrophage cells were labeled blue. (**A**) PHEMA hydrogel with 5% crosslinking density, and (**B**) PCBMA hydrogel with 5% crosslinking density. Macrophage cells expressing only MMR (blue color surrounded by red) were highlighted by the white arrows. Scale bars are 20 μm. (**C**) Percentage of macrophage cells express NOS and/or MMR biomarkers.

Chapter 8 Conclusions

The work presented in this thesis mainly demonstrates the biomedical applications of multifunctional zwitterionic carboxybetaine polymers and their derivatives in three aspects: multifunctional PCB nanoparticles, DNA vaccine delivery, and *in vivo* studies of PCB nanoparticles and hydrogel implants.

The excellent anti-fouling and functionalizable properties of PCB are critical for many biomedical applications. PCB is an excellent material for preparing stealthy nanoparticles and implants, which can efficiently evade recognition by the innate immune system and avoid an adverse response from the body. Notably, one major breakthrough in this thesis demonstrates that when the surface of subcutaneous implants becomes extremely nonfouling by using PCB, the foreign body reaction, which is inevitable to all types of other materials, can be greatly mitigated. Moreover, the functionalizable property further broadens the applications of PCB. PCB-based nanoparticles can easily been functionalized for simultaneous targeting, imaging, and therapy. Furthermore, PCB can be prepared as a hydrolysable form, PCB ester and its tertiary analogue, which can be switched from positive charge to neutral after hydrolysis for application such as high efficient but nontoxic DNA vaccine delivery.

The research described in this thesis lays the groundwork for several future projects. First, this thesis presents the splendid *in vitro* performance of the multifunctional nanoparticles for targeting, imaging, and therapy, as well as the hydrolytic microparticles

for DNA vaccine delivery. They hold great potential to move on to *in vivo* applications. Second, this thesis shows that softer and more flexible PCB nanoparticles can achieve lower splenic accumulation and longer circulation time *in vivo*. Basing on this work, large and flexible drug carriers mimicking red blood cell can be developed with higher drug loading than small and stiff carriers, without compromising their *in vivo* circulation time. Thus, better therapeutic efficiency can be expected with this platform. Third, this thesis presents PCB hydrogels that can efficiently mitigate capsule formation in a mouse model for at least three months. For the future work, longer time points such as one year after implantation should be tested because some implantable devices need to stay in the body for more than three months. Moreover, capsule formation in large animals, such as swine, should be evaluated. These results will be important before their applications in humans.

REFERENCES

[1] Ratner BD, Hoffman, A.S., Schoen, F.J., and Lemons, J.E. Biomaterials Science. 2nd ed: Amsterdam: Elsevier.; 2004.

[2] Binghe Wang TJS, Richard A. Soltero. Drug Delivery: Principles and Applications: Wiley-IEEE; 2005.

[3] Sun C, Lee JSH, Zhang MQ. Magnetic nanoparticles in MR imaging and drug delivery. Advanced Drug Delivery Reviews. 2008;60:1252-65.

[4] Jiang SY, Cao ZQ. Ultralow-Fouling, Functionalizable, and Hydrolyzable Zwitterionic Materials and Their Derivatives for Biological Applications. Advanced Materials. 2010;22:920-32.

[5] Magin CM, Cooper SP, Brennan AB. Non-toxic antifouling strategies. Materials Today. 2010;13:36-44.

[6] Zhang L, Xue H, Gao CL, Carr L, Wang JN, Chu BC, et al. Imaging and cell targeting characteristics of magnetic nanoparticles modified by a functionalizable zwitterionic polymer with adhesive 3,4-dihydroxyphenyl-L-alanine linkages. Biomaterials. 2010;31:6582-8.

[7] Moghimi SM, Hunter AC, Murray JC. Long-circulating and target-specific nanoparticles: Theory to practice. Pharmacological Reviews. 2001;53:283-318.

[8] Cheng G, Zhang Z, Chen SF, Bryers JD, Jiang SY. Inhibition of bacterial adhesion and biofilm formation on zwitterionic surfaces. Biomaterials. 2007;28:4192-9.

[9] Yang W, Xue H, Li W, Zhang JL, Jiang SY. Pursuing "Zero" Protein Adsorption of Poly(carboxybetaine) from Undiluted Blood Serum and Plasma. Langmuir. 2009;25:11911-6.

[10] Vaisocherova H, Yang W, Zhang Z, Cao ZQ, Cheng G, Piliarik M, et al. Ultralow fouling and functionalizable surface chemistry based on a zwitterionic polymer enabling sensitive and specific protein detection in undiluted blood plasma. Analytical Chemistry. 2008;80:7894-901.

[11] Carr LR, Jiang SY. Mediating high levels of gene transfer without cytotoxicity via hydrolytic cationic ester polymers. Biomaterials. 2010;31:4186-93.

[12] Cheng G, Xue H, Zhang Z, Chen SF, Jiang SY. A Switchable Biocompatible Polymer Surface with Self-Sterilizing and Nonfouling Capabilities. Angewandte Chemie-International Edition. 2008;47:8831-4.

[13] Corot C, Robert P, Idee JM, Port M. Recent advances in iron oxide nanocrystal technology for medical imaging. Advanced Drug Delivery Reviews. 2006;58:1471-504.

[14] Wang YXJ, Hussain SM, Krestin GP. Superparamagnetic iron oxide contrast agents: physicochemical characteristics and applications in MR imaging. European Radiology. 2001;11:2319-31.

[15] Singh M, Briones M, Ott G, O'Hagan D. Cationic microparticles: A potent delivery system for DNA vaccines. Proceedings of the National Academy of Sciences of the United States of America. 2000;97:811-6.

[16] Ratner BD. Reducing capsular thickness and enhancing angiogenesis around implant drug release systems. Journal of Controlled Release. 2002;78:211-8.

[17] Fang C, Zhang MQ. Multifunctional magnetic nanoparticles for medical imaging

applications. Journal of Materials Chemistry. 2009;19:6258-66.
[18] Dobson J. Magnetic nanoparticles for drug delivery. Drug Development Research. 2006;67:55-60.
[19] Duguet E, Vasseur S, Mornet S, Devoisselle JM. Magnetic nanoparticles and their applications in medicine. Nanomedicine. 2006;1:157-68.
[20] McCarthy JR, Kelly KA, Sun EY, Weissleder R. Targeted delivery of multifunctional magnetic nanoparticles. Nanomedicine. 2007;2:153-67.
[21] McCarthy JR, Weissleder R. Multifunctional magnetic nanoparticles for targeted imaging and therapy. Advanced Drug Delivery Reviews. 2008;60:1241-51.
[22] Cheng G, Li GZ, Xue H, Chen SF, Bryers JD, Jiang SY. Zwitterionic carboxybetaine polymer surfaces and their resistance to long-term biofilm formation. Biomaterials. 2009;30:5234-40.
[23] Zhang Z, Chao T, Chen SF, Jiang SY. Superlow fouling sulfobetaine and carboxybetaine polymers on glass slides. Langmuir. 2006;22:10072-7.
[24] Zhang Z, Chen SF, Jiang SY. Dual-functional biomimetic materials: Nonfouling poly(carboxybetaine) with active functional groups for protein immobilization. Biomacromolecules. 2006;7:3311-5.
[25] Li GZ, Cheng G, Xue H, Chen SF, Zhang FB, Jiang SY. Ultra low fouling zwitterionic polymers with a biomimetic adhesive group. Biomaterials. 2008;29:4592-7.
[26] Xie J, Xu C, Kohler N, Hou Y, Sun S. Controlled PEGylation of monodisperse Fe3O4 nanoparticles for reduced non-specific uptake by macrophage cells. Advanced Materials. 2007;19:3163-6.
[27] Dalsin JL, Lin LJ, Tosatti S, Voros J, Textor M, Messersmith PB. Protein resistance of titanium oxide surfaces modified by biologically inspired mPEG-DOPA. Langmuir. 2005;21:640-6.
[28] Sever MJ, Wilker JJ. Synthesis of peptides containing DOPA (3,4-dihydroxyphenylalanine). Tetrahedron. 2001;57:6139-46.
[29] Lu CW, Hung Y, Hsiao JK, Yao M, Chung TH, Lin YS, et al. Bifunctional magnetic silica nanoparticles for highly efficient human stem cell labeling. Nano Letters. 2007;7:149-54.
[30] Vaisocherova H, Zhang Z, Yang W, Cao ZQ, Cheng G, Taylor AD, et al. Functionalizable surface platform with reduced nonspecific protein adsorption from full blood plasma-Material selection and protein immobilization optimization. Biosensors & Bioelectronics. 2009;24:1924-30.
[31] Fang C, Bhattarai N, Sun C, Zhang MQ. Functionalized Nanoparticles with Long-Term Stability in Biological Media. SMALL. 2009;5:1637-41.
[32] Park IK, Ng CP, Wang J, Chu B, Yuan C, Zhang S, et al. Determination of nanoparticle vehicle unpackaging by MR imaging of a T-2 magnetic relaxation switch. Biomaterials. 2008;29:724-32.
[33] Polyak B, Fishbein I, Chorny M, Alferiev I, Williams D, Yellen B, et al. High field gradient targeting of magnetic nanoparticle-loaded endothelial cells to the surfaces of steed stents. Proceedings of the National Academy of Sciences of the United States of America.

2008;105:698-703.
[34] Yavuz CT, Mayo JT, Yu WW, Prakash A, Falkner JC, Yean S, et al. Low-field magnetic separation of monodisperse Fe3O4 nanocrystals. Science. 2006;314:964-7.
[35] Lee HY, Lee SH, Xu CJ, Xie J, Lee JH, Wu B, et al. Synthesis and characterization of PVP-coated large core iron oxide nanoparticles as an MRI contrast agent. Nanotechnology. 2008;19.
[36] Sato T, Iijima T, Seki M, Inagaki N. Magnetic properties of ultrafine ferrite particles. Journal of Magnetism and Magnetic Materials. 1987;65:252-6.
[37] Seo SB, Yang J, Hyung W, Cho EJ, Lee TI, Song YJ, et al. Novel multifunctional PHDCA/PEI nano-drug carriers for simultaneous magnetically targeted cancer therapy and diagnosis via magnetic resonance imaging. Nanotechnology. 2007;18.
[38] Jun YW, Huh YM, Choi JS, Lee JH, Song HT, Kim S, et al. Nanoscale size effect of magnetic nanocrystals and their utilization for cancer diagnosis via magnetic resonance imaging. Journal of the American Chemical Society. 2005;127:5732-3.
[39] Horcajada P, Chalati T, Serre C, Gillet B, Sebrie C, Baati T, et al. Porous metal-organic-framework nanoscale carriers as a potential platform for drug delivery and imaging. Nature Materials. 2010;9:172-8.
[40] Meng FH, Hennink WE, Zhong Z. Reduction-sensitive polymers and bioconjugates for biomedical applications. Biomaterials. 2009;30:2180-98.
[41] Oh JK, Tang CB, Gao HF, Tsarevsky NV, Matyjaszewski K. Inverse miniemulsion ATRP: A new method for synthesis and functionalization of well-defined water-soluble/cross-linked polymeric particles. Journal of the American Chemical Society. 2006;128:5578-84.
[42] Jia GW, Cao ZQ, Xue H, Xu YS, Jiang SY. Novel Zwitterionic-Polymer-Coated Silica Nanoparticles. Langmuir. 2009;25:3196-9.
[43] Yang W, Zhang L, Wang SL, White AD, Jiang SY. Functionalizable and ultra stable nanoparticles coated with zwitterionic poly(carboxybetaine) in undiluted blood serum. Biomaterials. 2009;30:5617-21.
[44] Cao ZQ, Yu QM, Xue H, Cheng G, Jiang SY. Nanoparticles for Drug Delivery Prepared from Amphiphilic PLGA Zwitterionic Block Copolymers with Sharp Contrast in Polarity between Two Blocks. Angewandte Chemie-International Edition. 2010;49:3771-6.
[45] Cheng G, Mi L, Cao ZQ, Xue H, Yu QM, Carr L, et al. Functionalizable and Ultrastable Zwitterionic Nanogels. Langmuir. 2010;26:6883-6.
[46] Tanaka J, Stansbury JW, Antonucci JM, Suzuki K. Surface treatment with N,N'-Dimethacryloylcystine for enhanced bonding of resin to dental alloys. Dental Materials Journal. 2007;26:514-8.
[47] Park J, An KJ, Hwang YS, Park JG, Noh HJ, Kim JY, et al. Ultra-large-scale syntheses of monodisperse nanocrystals. Nature Materials. 2004;3:891-5.
[48] Liong M, Lu J, Kovochich M, Xia T, Ruehm SG, Nel AE, et al. Multifunctional inorganic nanoparticles for imaging, targeting, and drug delivery. Acs Nano. 2008;2:889-96.
[49] Choi HS, Liu W, Misra P, Tanaka E, Zimmer JP, Ipe BI, et al. Renal clearance of quantum dots. Nature Biotechnology. 2007;25:1165-70.

[50] Veiseh O, Gunn JW, Zhang MQ. Design and fabrication of magnetic nanoparticles for targeted drug delivery and imaging. Adv Drug Deliv Rev. 2010;62:284-304.
[51] Jun YW, Lee JH, Cheon J. Chemical design of nanoparticle probes for high-performance magnetic resonance imaging. Angewandte Chemie-International Edition. 2008;47:5122-35.
[52] Lee JH, Jun YW, Yeon SI, Shin JS, Cheon J. Dual-mode nanoparticle probes for high-performance magnetic resonance and fluorescence imaging of neuroblastoma. Angewandte Chemie-International Edition. 2006;45:8160-2.
[53] Reddy GR, Bhojani MS, McConville P, Moody J, Moffat BA, Hall DE, et al. Vascular targeted nanoparticles for imaging and treatment of brain tumors. Clinical Cancer Research. 2006;12:6677-86.
[54] Moffat BA, Reddy GR, McConville P, Hall DE, Chenevert TL, Kopelman RR, et al. A novel polyacrylamide magnetic nanoparticle contrast agent for molecular imaging using MRI. molecular imaging. 2003;2:324?32.
[55] Melancon MP, Lu W, Li C. Gold-Based Magneto/Optical Nanostructures: Challenges for *In vivo* Applications in Cancer Diagnostics and Therapy. MRS Bulletin. 2009;34:415-21.
[56] Willets KA, Van Duyne RP. Localized surface plasmon resonance spectroscopy and sensing. Annual Review of Physical Chemistry. 2007;58:267-97.
[57] Jain PK, Huang X, El-Sayed IH, El-Sayad MA. Review of some interesting surface plasmon resonance-enhanced properties of noble metal nanoparticles and their applications to biosystems. Plasmonics. 2007;2:107-18.
[58] El-Sayed IH, Huang XH, El-Sayed MA. Surface plasmon resonance scattering and absorption of anti-EGFR antibody conjugated gold nanoparticles in cancer diagnostics: Applications in oral cancer. Nano Letters. 2005;5:829-34.
[59] Tam JM, Tam JO, Murthy A, Ingram DR, Ma LL, Travis K, et al. Controlled Assembly of Biodegradable Plasmonic Nanoclusters for Near-Infrared Imaging and Therapeutic Applications. ACS Nano. 2010;4:2178-84.
[60] Anker JN, Hall WP, Lyandres O, Shah NC, Zhao J, Van Duyne RP. Biosensing with plasmonic nanosensors. Nature Materials. 2008;7:442-53.
[61] Yu QM, Guan P, Qin D, Golden G, Wallace PM. Inverted size-dependence of surface-enhanced Raman scattering on gold nanohole and nanodisk arrays. Nano Letters. 2008;8:1923-8.
[62] Bardhan R, Chen WX, Perez-Torres C, Bartels M, Huschka RM, Zhao LL, et al. Nanoshells with Targeted Simultaneous Enhancement of Magnetic and Optical Imaging and Photothermal Therapeutic Response. Advanced Functional Materials. 2009;19:3901-9.
[63] Ji XJ, Shao RP, Elliott AM, Stafford RJ, Esparza-Coss E, Bankson JA, et al. Bifunctional gold nanoshells with a superparamagnetic iron oxide-silica core suitable for both MR imaging and photothermal therapy. Journal of Physical Chemistry C. 2007;111:6245-51.
[64] Atwater HA, Polman A. Plasmonics for improved photovoltaic devices. Nature Materials. 2010;9:205-13.
[65] Schuller JA, Barnard ES, Cai WS, Jun YC, White JS, Brongersma ML. Plasmonics for extreme light concentration and manipulation. Nature Materials. 2010;9:193-204.

[66] Levin CS, Hofmann C, Ali TA, Kelly AT, Morosan E, Nordlander P, et al. Magnetic-Plasmonic Core-Shell Nanoparticles. ACS Nano. 2009;3:1379-88.
[67] Ma LL, Feldman MD, Tam JM, Paranjape AS, Cheruku KK, Larson TA, et al. Small Multifunctional Nanoclusters (Nanoroses) for Targeted Cellular Imaging and Therapy. ACS Nano. 2009;3:2686-96.
[68] Yu H, Chen M, Rice PM, Wang SX, White RL, Sun SH. Dumbbell-like bifunctional Au-Fe3O4 nanoparticles. Nano Letters. 2005;5:379-82.
[69] Wang CG, Irudayaraj J. Multifunctional Magnetic-Optical Nanoparticle Probes for Simultaneous Detection, Separation, and Thermal Ablation of Multiple Pathogens. Small. 2010;6:283-9.
[70] Wang CG, Chen J, Talavage T, Irudayaraj J. Gold Nanorod/Fe3O4 Nanoparticle "Nano-Pearl-Necklaces" for Simultaneous Targeting, Dual-Mode Imaging, and Photothermal Ablation of Cancer Cells. Angewandte Chemie-International Edition. 2009;48:2759-63.
[71] Zhang Q, Ge JP, Goebl J, Hu YX, Sun YG, Yin YD. Tailored Synthesis of Superparamagnetic Gold Nanoshells with Tunable Optical Properties. Advanced Materials. 2010;22:1905-+.
[72] Kneipp K, Wang Y, Kneipp H, Perelman LT, Itzkan I, Dasari R, et al. Single molecule detection using surface-enhanced Raman scattering (SERS). Physical Review Letters. 1997;78:1667-70.
[73] Nie SM, Emery SR. Probing single molecules and single nanoparticles by surface-enhanced Raman scattering. Science. 1997;275:1102-6.
[74] Zhou X, Xu WL, Wang Y, Kuang Q, Shi YF, Zhong LB, et al. Fabrication of Cluster/Shell Fe3O4/Au Nanoparticles and Application in Protein Detection via a SERS Method. Journal of Physical Chemistry C. 2011;114:19607-13.
[75] Xu CJ, Yuan ZL, Kohler N, Kim JM, Chung MA, Sun SH. FePt Nanoparticles as an Fe Reservoir for Controlled Fe Release and Tumor Inhibition. Journal of the American Chemical Society. 2009;131:15346-51.
[76] Tang DP, Yuan R, Chai YQ. Magnetic core-shell Fe3O4@Ag nanoparticles coated carbon paste interface for studies of carcinoembryonic antigen in clinical immunoassay. Journal of Physical Chemistry B. 2006;110:11640-6.
[77] Zhuo Y, Yuan PX, Yuan R, Chai YQ, Hong CL. Bienzyme functionalized three-layer composite magnetic nanoparticles for electrochemical immunosensors. Biomaterials. 2009;30:2284-90.
[78] Jarvis RM, Goodacre R. Characterisation and identification of bacteria using SERS. Chemical Society Reviews. 2008;37:931-6.
[79] Guicheteau J, Argue L, Emge D, Hyre A, Jacobson M, Christesen S. Bacillus spore classification via surface-enhanced Raman spectroscopy and principal component analysis. Applied Spectroscopy. 2008;62:267-72.
[80] Ivleva NP, Wagner M, Horn H, Niessner R, Haisch C. In Situ Surface-Enhanced Raman Scattering Analysis of Biofilm. Analytical Chemistry. 2008;80:8538-44.
[81] Holt RE, Cotton TM. SURFACE-ENHANCED RESONANCE RAMAN AND

ELECTROCHEMICAL INVESTIGATION OF GLUCOSE-OXIDASE CATALYSIS AT A SILVER ELECTRODE. Journal of the American Chemical Society. 1989;111:2815-21.
[82] Sengupta A, Mujacic M, Davis EJ. Detection of bacteria by surface-enhanced Raman spectroscopy. Analytical and Bioanalytical Chemistry. 2006;386:1379-86.
[83] Kahraman M, Yazici MM, Sahin F, Culha M. Convective assembly of bacteria for surface-enhanced Raman scattering. Langmuir. 2008;24:894-901.
[84] Yang LL, Yan B, Premasiri WR, Ziegler LD, Dal Negro L, Reinhard BM. Engineering Nanoparticle Cluster Arrays for Bacterial Biosensing: The Role of the Building Block in Multiscale SERS Substrates. Advanced Functional Materials. 2010;20:2619-28.
[85] Wang YL, Ravindranath S, Irudayaraj J. Separation and detection of multiple pathogens in a food matrix by magnetic SERS nanoprobes. Analytical and Bioanalytical Chemistry. 2011;399:1271-8.
[86] Zhou RH, Wang P, Chang HC. Bacteria capture, concentration and detection by alternating current dielectrophoresis and self-assembly of dispersed single-wall carbon nanotubes. Electrophoresis. 2006;27:1376-85.
[87] Mabey D, Peeling RW, Ustianowski A, Perkins MD. Diagnostics for the developing world. Nature Reviews Microbiology. 2004;2:231-40.
[88] Zhang JY, Do J, Premasiri WR, Ziegler LD, Klapperich CM. Rapid point-of-care concentration of bacteria in a disposable microfluidic device using meniscus dragging effect. Lab on a Chip. 2010;10:3265-70.
[89] Nigam S, Barick KC, Bahadur D. Development of citrate-stabilized Fe3O4 nanoparticles: Conjugation and release of doxorubicin for therapeutic applications. Journal of Magnetism and Magnetic Materials. 2011;323:237-43.
[90] Goon IY, Lai LMH, Lim M, Munroe P, Gooding JJ, Amal R. Fabrication and Dispersion of Gold-Shell-Protected Magnetite Nanoparticles: Systematic Control Using Polyethyleneimine. Chemistry of Materials. 2009;21:673-81.
[91] McLellan JM, Xiong YJ, Hu M, Xia YN. Surface-enhanced Raman scattering of 4-mercaptopyridine on thin films of nanoscale Pd cubes, boxes, and cages. Chemical Physics Letters. 2006;417:230-4.
[92] Jin YD, Gao XH. Plasmonic fluorescent quantum dots. Nature Nanotechnology. 2009;4:571-6.
[93] Oldenburg SJ, Averitt RD, Westcott SL, Halas NJ. Nanoengineering of optical resonances. Chemical Physics Letters. 1998;288:243-7.
[94] Hirsch LR, Gobin AM, Lowery AR, Tam F, Drezek RA, Halas NJ, et al. Metal nanoshells. Annals of Biomedical Engineering. 2006;34:15-22.
[95] Kneipp J, Kneipp H, Kneipp K. SERS - a single-molecule and nanoscale tool for bioanalytics. Chemical Society Reviews. 2008;37:1052-60.
[96] Xu JJ, Guan P, Kvasnicka P, Gong H, Homola J, Yu QM. Light Transmission and Surface-Enhanced Raman Scattering of Quasi-3D Plasmonic Nanostructure Arrays with Deep and Shallow Fabry-Prot Nanocavities. The Journal of Physical Chemistry C. 2011;115:7.
[97] Xu JJ, Zhang L, Gong H, Homola J, Yu QM. Tailoring Plasmonic Nanostructures for

Optimal SERS Sensing of Small Molecules and Large Microorganisms. Small. 2010;7:371-6.
[98] Hu JW, Zhao B, Xu WQ, Li BF, Fan YG. Surface-enhanced Raman spectroscopy study on the structure changes of 4-mercaptopyridine adsorbed on silver substrates and silver colloids. Spectrochimica Acta Part a-Molecular and Biomolecular Spectroscopy. 2002;58:2827-34.
[99] Wei E. Huang ML, Roger M. Jarvis, Royston Goodacre, and Steven A. Banwart. Shining Light on the Microbial World: The Application of Raman Microspectroscopy. Advances in Applied Microbiology2010. p. 153-86.
[100] Nguyen DN, Green JJ, Chan JM, Longer R, Anderson DG. Polymeric Materials for Gene Delivery and DNA Vaccination. Advanced Materials. 2009;21:847-67.
[101] O'Hagan DT, Singh M, Ulmer JB. Microparticles for the delivery of DNA vaccines. Immunological Reviews. 2004;199:191-200.
[102] Ulmer JB, Valley U, Rappuoli R. Vaccine manufacturing: challenges and solutions. Nature Biotechnology. 2006;24:1377-83.
[103] Plotkin SA, Plotkin SL. The development of vaccines: how the past led to the future. Nature Reviews Microbiology. 2011;9:889-93.
[104] Pack DW, Hoffman AS, Pun S, Stayton PS. Design and development of polymers for gene delivery. Nature Reviews Drug Discovery. 2005;4:581-93.
[105] Berzofsky JA, Ahlers JD, Belyakov IM. Strategies for designing and optimizing new generation vaccines. Nature Reviews Immunology. 2001;1:209-19.
[106] Sharma AK, Khuller GK. DNA vaccines: Future strategies and relevance to intracellular pathogens. Immunology and Cell Biology. 2001;79:537-46.
[107] Liu MA. DNA vaccines: an historical perspective and view to the future. Immunological Reviews. 2011;239:62-84.
[108] Little SR, Lynn DM, Ge Q, Anderson DG, Puram SV, Chen JZ, et al. Poly-beta amino ester-containing microparticles enhance the activity of nonviral genetic vaccines. Proceedings of the National Academy of Sciences of the United States of America. 2004;101:9534-9.
[109] Tang DC, Devit M, Johnston SA. Genetic immunization is a simple method for eliciting an immune-response. Nature. 1992;356:152-4.
[110] Coban C, Kobiyama K, Aoshi T, Takeshita F, Horii T, Akira S, et al. Novel Strategies to Improve DNA Vaccine Immunogenicity. Current Gene Therapy. 2011;11:479-84.
[111] van den Berg JH, Nuijen B, Schumacher TN, Haanen J, Storm G, Beijnen JH, et al. Synthetic vehicles for DNA vaccination. Journal of Drug Targeting. 2010;18:1-14.
[112] Little SR, Lynn DM, Puram SV, Langer R. Formulation and characterization of poly (beta amino ester) microparticles for genetic vaccine delivery. Journal of Controlled Release. 2005;107:449-62.
[113] Kasturi SP, Sachaphibulkij K, Roy K. Covalent conjugation of polyethyleneimine on biodegradable microparticles for delivery of plasmid DNA vaccines. Biomaterials. 2005;26:6375-85.
[114] Singh M, Ugozzoli M, Briones M, Kazzaz J, Soenawan E, O'Hagan DT. The effect of CTAB concentration in cationic PLG microparticles on DNA adsorption and *in vivo* performance. Pharmaceutical Research. 2003;20:247-51.

[115] Kasturi SP, Qin H, Thomson KS, El-Bereir S, Cha SC, Neelapu S, et al. Prophylactic anti-tumor effects in a B cell lymphoma model with DNA vaccines delivered on polyethylenimine (PEI) functionalized PLGA microparticles. Journal of Controlled Release. 2006;113:261-70.
[116] Zhang L, Xue H, Cao Z, Keefe A, Wang J, Jiang S. Multifunctional and degradable zwitterionic nanogels for targeted delivery, enhanced MR imaging, reduction-sensitive drug release, and renal clearance. Biomaterials. 2011;32:4604-8.
[117] Briones M, Singh M, Ugozzoli M, Kazzaz J, Klakamp S, Ott G, et al. The preparation, characterization, and evaluation of cationic microparticles for DNA vaccine delivery. Pharmaceutical Research. 2001;18:709-12.
[118] Wong SY, Pelet JM, Putnam D. Polymer systems for gene delivery-past, present, and future. Progress in Polymer Science. 2007;32:799-837.
[119] Minigo G, Scholzen A, Tang CK, Hanley JC, Kalkanidis M, Pietersz GA, et al. Poly-L-lysine-coated nanoparticles: A potent delivery system to enhance DNA vaccine efficacy. Vaccine. 2007;25:1316-27.
[120] Gu F, Zhang L, Teply BA, Mann N, Wang A, Radovic-Moreno AF, et al. Precise engineering of targeted nanoparticles by using self-assembled biointegrated block copolymers. Proceedings of the National Academy of Sciences of the United States of America. 2008;105:2586-91.
[121] van Schooneveld MM, Vucic E, Koole R, Zhou Y, Stocks J, Cormode DP, et al. Improved biocompatibility and pharmacokinetics of silica nanoparticles by means of a lipid coating: A multimodality investigation. Nano Letters. 2008;8:2517-25.
[122] Peer D, Karp JM, Hong S, FaroKhzad OC, Margalit R, Langer R. Nanocarriers as an emerging platform for cancer therapy. Nat Nanotechnol. 2007;2:751-60.
[123] Mornet S, Vasseur S, Grasset F, Duguet E. Magnetic nanoparticle design for medical diagnosis and therapy. Journal of Materials Chemistry. 2004;14:2161-75.
[124] Mebius RE, Kraal G. Structure and function of the spleen. Nature Reviews Immunology. 2005;5:606-16.
[125] Perrault SD, Walkey C, Jennings T, Fischer HC, Chan WCW. Mediating Tumor Targeting Efficiency of Nanoparticles Through Design. Nano Letters. 2009;9:1909-15.
[126] Moghimi SM, Porter CJH, Muir IS, Illum L, Davis SS. Non-phagocytic uptake of intravenously injected microspheres in rat spleen - influence of particle-size and hydrophilic coating. Biochemical and Biophysical Research Communications. 1991;177:861-6.
[127] Geng Y, Dalhaimer P, Cai SS, Tsai R, Tewari M, Minko T, et al. Shape effects of filaments versus spherical particles in flow and drug delivery. Nature Nanotechnology. 2007;2:249-55.
[128] Park JH, von Maltzahn G, Zhang LL, Derfus AM, Simberg D, Harris TJ, et al. Systematic Surface Engineering of Magnetic Nanoworms for *in vivo* Tumor Targeting. Small. 2009;5:694-700.
[129] Merkel TJ, Jones SW, Herlihy KP, Kersey FR, Shields AR, Napier M, et al. Using mechanobiological mimicry of red blood cells to extend circulation times of hydrogel microparticles. Proceedings of the National Academy of Sciences of the United States of

America. 2011;108:586-91.
[130] Mitragotri S, Lahann J. Physical approaches to biomaterial design. Nature Materials. 2009;8:15-23.
[131] Carr LR, Zhou YB, Krause JE, Xue H, Jiang SY. Uniform zwitterionic polymer hydrogels with a nonfouling and functionalizable crosslinker using photopolymerization. Biomaterials. 2011;32:6893-9.
[132] Cai QY, Kim SH, Choi KS, Kim SY, Byun SJ, Kim KW, et al. Colloidal gold nanoparticles as a blood-pool contrast agent for x-ray computed tomography in mice. Investigative Radiology. 2007;42:797-806.
[133] Zhang GD, Yang Z, Lu W, Zhang R, Huang Q, Tian M, et al. Influence of anchoring ligands and particle size on the colloidal stability and *in vivo* biodistribution of polyethylene glycol-coated gold nanoparticles in tumor-xenografted mice. Biomaterials. 2009;30:1928-36.
[134] Kim D, Park S, Lee JH, Jeong YY, Jon S. Antibiofouling polymer-coated gold nanoparticles as a contrast agent for *in vivo* x-ray computed tomography imaging. Journal of the American Chemical Society. 2007;129:7661-5.
[135] Cheng J, Teply BA, Sherifi I, Sung J, Luther G, Gu FX, et al. Formulation of functionalized PLGA-PEG nanoparticles for *in vivo* targeted drug delivery. Biomaterials. 2007;28:869-76.
[136] Chen VMaY. Nanoparticles - A Review. Tropical Journal of Pharmaceutical Research. 2006;5:561-73.
[137] Redhead HM, Davis SS, Illum L. Drug delivery in poly(lactide-co-glycolide) nanoparticles surface modified with poloxamer 407 and poloxamine 908: *in vitro* characterisation and *in vivo* evaluation. Journal of Controlled Release. 2001;70:353-63.
[138] Anderson JM, Rodriguez A, Chang DT. Foreign body reaction to biomaterials. Seminars in Immunology. 2008;20:86-100.
[139] Langer R, Tirrell DA. Designing materials for biology and medicine. Nature. 2004;428:487-92.
[140] Williams DF. On the nature of biomaterials. Biomaterials. 2009;30:5897-909.
[141] Langer R. Perspectives and Challenges in Tissue Engineering and Regenerative Medicine. Advanced Materials. 2009;21:3235-6.
[142] Ward WK. A Review of the Foreign-body Response to Subcutaneously-implanted Devices: The Role of Macrophages and Cytokines in Biofouling and Fibrosis. Journal of Diabetes Science and Technology. 2008;2:768-77.
[143] Hetrick EM, Prichard HL, Klitzman B, Schoenfisch MH. Reduced foreign body response at nitric oxide-releasing subcutaneous implants. Biomaterials. 2007;28:4571-80.
[144] Williams DF. On the mechanisms of biocompatibility. Biomaterials. 2008;29:2941-53.
[145] Ostuni E, Chapman RG, Holmlin RE, Takayama S, Whitesides GM. A survey of structure-property relationships of surfaces that resist the adsorption of protein. Langmuir. 2001;17:5605-20.
[146] Gref R, Minamitake Y, Peracchia MT, Trubetskoy V, Torchilin V, Langer R. Biodegradable long-circulating polymeric nanospheres. Science. 1994;263:1600-3.

[147] Davis ME, Zuckerman JE, Choi CHJ, Seligson D, Tolcher A, Alabi CA, et al. Evidence of RNAi in humans from systemically administered siRNA via targeted nanoparticles. Nature. 2010;464:1067-U140.
[148] Ward WK, Slobodzian EP, Tiekotter KL, Wood MD. The effect of microgeometry, implant thickness and polyurethane chemistry on the foreign body response to subcutaneous implants. Biomaterials. 2002;23:4185-92.
[149] Carr LR, Cheng G, Xue H, Jiang S. Engineering the Polymer Backbone To Strengthen Nonfouling Sulfobetaine Hydrogels. Langmuir. 2010;26:14793-8.
[150] Zhang Z, Chao T, Liu L, Cheng G, Ratner BD, Jiang S. Zwitterionic Hydrogels: an *in vivo* Implantation Study. Journal of Biomaterials Science-Polymer Edition. 2009;20:1845-59.
[151] Tsai AT, Rice J, Scatena M, Liaw L, Ratner BD, Giachelli CM. The role of osteopontin in foreign body giant cell formation. Biomaterials. 2005;26:5835-43.
[152] Madden LR, Mortisen DJ, Sussman EM, Dupras SK, Fugate JA, Cuy JL, et al. Proangiogenic scaffolds as functional templates for cardiac tissue engineering. Proceedings of the National Academy of Sciences of the United States of America. 2010;107:15211-6.
[153] Carr LR, Xue H, Jiang SY. Functionalizable and nonfouling zwitterionic carboxybetaine hydrogels with a carboxybetaine dimethacrylate crosslinker. Biomaterials. 2011;32:961-8.

Curriculum Vitae

EDUCATION

Ph.D. in Chemical Engineering, University of Washington - 2012
M.Sc. in Chemical Engineering, University of Washington - 2010
B.Engn. in Chemical Engineering & technology, Tianjin University - 2003

PUBLICATIONS

1. **Lei Zhang**, Zhiqiang Cao, Louisa Carr, Tao Bai, Jean-Rene Ella-Menye, Colleen Irvin, Buddy D. Ratner, and Shaoyi Jiang, Inhibition of foreign body capsule formation by implanted zwitterionic hydrogels, 2012, (**submitted**)
2. **Lei Zhang**, Louisa Carr, Zhiqiang Cao, Jean-Rene Ella-Menye, and Shaoyi Jiang, Hydrolytic cationic ester microparticles for high efficiency DNA vaccine delivery, 2012, (**in preparation**)
3. **Lei Zhang**, Zhiqiang Cao, Yuting Li, Jean-Rene Ella-Menye, Tao Bai, and Shaoyi Jiang, Softer zwitterionic nanogels for longer circulation and lower splenic accumulation, 2012, (**ACS NANO, in revision**)
4. **Lei Zhang**, Jiajie Xu, Luo Mi, Heng Gong, Shaoyi Jiang and Qiuming Yu, Magnetic-plasmonic Fe_3O_4-Au core-shell nanoparticles for fast concentration and sensitive detection of bacteria using SERS. **Biosensors and Bioelectronics** 2012; 31 (1): 130-136
5. **Lei Zhang**, Hong Xue, Zhiqiang Cao, Andrew Keefe, Jinnan Wang and Shaoyi Jiang, Multifunctional and degradable zwitterionic nanogels for targeted delivery, enhanced MR imaging, reduction-sensitive drug release, and renal clearance. **Biomaterials** 2011; 32(20): 4604-4608
6. **Lei Zhang**, Hong Xue, Changlu Gao, Louisa Carr, Jinnan Wang, Baocheng Chu, and Shaoyi Jiang, Imaging and cell targeting characteristics of magnetic nanoparticles modified by a functionalizable zwitterionic polymer with adhesive 3,4-dihydroxyphenyl-L-alanine linkages. **Biomaterials** 2010; 31(25): 6582–6588
7. **Lei Zhang**, Faquan Yu, Jingkang Wang, and Victor C. Yang, Gum arabic-coated magnetic nanoparticles for potential application in simultaneous magnetic targeting and tumor imaging. **AAPS Journal** 2009; 11(4): 693-699.
8. Zhiqiang Cao, **Lei Zhang (co-first author)**, and Shaoyi Jiang, Poly(zwitterionic) liposome for drug delivery, 2012, (**submitted**)
9. Zhiqiang Cao, Luo Mi, Jose Mendiola, Jean-Rene Ella-Menye, **Lei Zhang**, Hong Xue and Shaoyi Jiang, Reversibly switching the function of a surface between attacking and defending against bacteria. **Angewandte Chemie International Edition** 2012; 124(11), 2602-2605
10. Jiajie Xu, **Lei Zhang**, Heng Gong, Jiri Homola, and Qiuming Yu, Tailoring plasmonic nanostructures for optimal SERS sensing of small molecules and large microorganisms. **Small** 2011;7(3): 371-376

11. Faquan Yu, **Lei Zhang**, Yongzhuo Huang, Kai Sun, Allan E. David, and Victor C. Yang, The magnetophoretic mobility and superparamagnetism of core-shell iron oxide nanoparticles with dual targeting and imaging functionality. **Biomaterials** 2010; 31(22): 5842-5848.
12. Wei Yang, **Lei Zhang**, Shanlin. Wang, Andrew D. White, and Shaoyi Jiang, Functionalizable and ultra stable nanoparticles coated with zwitterionic poly(carboxybetaine) in undiluted blood serum, **Biomaterials** 2009; 30(29): 5617–5621

CONFERENCE TALKS

1. Multifunctional Zwitterionic Nanogels for Targeted Drug Delivery and Renal Clearance. 2011 AIChE Annual Meeting, Minneapolis, MN, Oct, 2011.
2. Magnetic Plasmonic Core-Shell Nanoparticles for Fast Condensation and Detection of Bacteria Using SERS. 2011 AIChE Annual Meeting, Minneapolis, MN, Oct, 2011.
3. Highly Efficient DNA Vaccine Based On Hydrolytic Cationic Ester Particles, 2011 AIChE Annual Meeting, Minneapolis, MN, Oct, 2011.
4. Stealth and functionalizable zwitterionic magnetic nanoparticles prepared by a one-step method for image-guided targeting drug delivery. 240th American Chemical Society National Meeting, Boston, MA, Aug, 2010.
5. Multifunctional Magnetic Nanoparticles Coated by Zwitterionic Polymer. 2009 AIChE Annual Meeting, Nashville, TN, Nov, 2009.